

# Simulations of Proton Transfer Processes using Reactive Force Fields

Inauguraldissertation

zur

Erlangung der Würde eines Doktors der Philosophie

vorgelegt der

Philosophisch–Naturwissenschaftlichen Fakultät

der Universität Basel

von

Sven Lammers

aus Husum, Deutschland

Basel, 2006

Genehmigt von der Philosophisch-Naturwissenschaftlichen Fakultät  
auf Antrag von:

Prof. Dr. Markus Meuwly  
Prof. Dr. Hanspeter Huber

Basel, 19. Dezember 2006

Prof. Dr. Hans-Jakob Wirz (Dekan)

# Acknowledgment

I would like to thank Prof. Dr. Markus Meuwly for giving me the opportunity to work as a doctoral student in his group, as well as for his guidance and support during the last four years.

Prof. Dr. Hanspeter Huber and his group for our jointly held group seminars and him personally for many interesting discussions and for being so kind to act as co-referee.

I would also like to thank the past and current members of the group Dr. David Nutt, Dr. Vincent Zoete, Dr. Polina Banushkina, Holmfridur Thorsteinsdottir, Franziska Schmid, Dr. Jonas Danielsson, Dr. Antony Fouqueau, Manuela Koch and Stefan Lutz, with whom I had the pleasure to work with.

I would like to thank my family and friends for their love and support. Much love to Mom, Dad, my brother Hanno and sister Inken, Zoe Cournia, Florian Weissbach, Lars Gummels, and Arne Greve.

# Abstract

Proton transfer reactions are of fundamental importance for a wide range of chemical and biological processes. Theoretical investigations of these dynamical processes are therefore of great interest. The energetic barrier for proton and hydrogen transfer is often so high that transfer events happen only rarely. The long time scales involved complicate application of accurate dynamical studies such as QM/MM molecular dynamics simulations. To supply useful information concerning biochemical reactions, computational methods have to provide the possibility of sufficient sampling (i.e. have to be computationally very efficient) and have to be accurate in the description of the chemical reaction of interest.

We present reactive molecular force fields that are computationally very efficient derived from accurate high level *ab initio* potential energy surfaces. Based on prototype systems such as the protonated water dimer, protonated ammonia dimer and protonated ammonia water hetero-dimer, multidimensional potential energy surfaces have been calculated. Using these, a force field representation has been developed to study the dynamics of the transfer events by molecular dynamics simulations. The flexible implementation of the force field makes it transferable to a variety of systems with hydrogen bonding patterns.

We present applications of the reactive force field to the dynamics of single and double proton/hydrogen bonds in systems of chemical and biological interest. Results are discussed for prototype systems, systems exhibiting double proton transfer, and systems of biological interest (proton transfer in ferredoxin I). For the former, infrared spectra are calculated that can be compared to experimental results, while for the latter proton transfer rates from protein side chains to a buried [3Fe-4S] cluster are of interest.

# Contents

<b>1. Introduction</b>	<b>5</b>
<b>2. Theoretical Background</b>	<b>7</b>
2.1. Molecular Dynamics Simulations . . . . .	7
2.1.1. Historical Notes . . . . .	7
2.1.2. Foundations . . . . .	8
2.2. Simulation of proton transfer reactions . . . . .	10
2.2.1. Hybrid quantal/classical methods . . . . .	10
2.2.2. Reactive force fields . . . . .	12
2.3. Morphing of ab-initio based potential energy surfaces . . . . .	13
<b>3. Applications</b>	<b>15</b>
3.1. Reactive force fields for proton transfer dynamics . . . . .	15
3.1.1. Introduction . . . . .	15
3.1.2. Method . . . . .	15
3.1.3. Implementation . . . . .	21
3.1.4. Morphing Transformations . . . . .	26
3.1.5. Proton bound homo dimer $\text{NH}_4^+ \cdots \text{NH}_3$ . . . . .	26
3.1.6. Double proton transfer in 2PY2HP . . . . .	38
3.1.7. Ferredoxin I . . . . .	44
3.1.8. Conclusion . . . . .	49
3.2. Investigating the Relationship between Infrared Spectra of Shared Protons in Different Chemical Environments: A Comparison of protonated diglyme and protonated water dimer . . . . .	52
3.2.1. Introduction . . . . .	52
3.2.2. Computational Methods . . . . .	55

<b>Contents</b>	<b>4</b>
3.2.3. Results . . . . .	58
3.2.4. Discussion and Conclusion . . . . .	64
<b>4. Published Work</b>	<b>79</b>
<b>5. Summary and Outlook</b>	<b>87</b>
<b>Bibliography</b>	<b>88</b>
<b>A. Instructions for Use of CHARMM and MMPT</b>	<b>101</b>
A.1. Compilation . . . . .	101
A.2. Usage . . . . .	102
<b>B. Fitting and Morphing of PES</b>	<b>105</b>
B.1. Fitting with I-NoLLS . . . . .	105
B.2. Morphing of PES . . . . .	105
<b>C. Parameter Tables</b>	<b>111</b>

# 1. Introduction

Why carrying out simulations for proton transfer reactions? Because there are several categories of processes associated with the proton transfer in living system, e.g. bio-energy and signal transfer, that are essential to life. No life without this simple reaction. But although simple, research in this area is a great challenge because there are only a few approaches that could be used for such studies. Among them, quantum chemical methods belong to the key ones. But on the other hand quantum chemical methods happen to be slow. Especially in the case of proton transfer reactions where we have to apply a high-level of theory to get accurate results. This is the dilemma of the computational scientist. Either choose a crude approximation or wait a long long time for your calculations to finish. And this is particularly true for dynamics simulations. Molecular dynamics simulations, although they are classical descriptions, have proven to be a valuable tool in dynamics studies, and we combined potential energy surfaces derived from accurate quantum chemical calculations with the speed of molecular dynamics simulation. At the heart of the molecular dynamics simulation lies the potential energy surface. The introductory chapter explains the typical form to the potential energy functions and discusses other approaches to proton transfer simulations and how potential energy surfaces have been improved using a morphing approach in the past. The chapter Applications contains two manuscripts. The first is a methodological manuscript in preparation for the Journal of Computational Chemistry. In this manuscript we extend the picture of potential energy functions by introducing potential energy functions that do not suffer from the limits of conventional molecular dynamics simulation and are capable to describe the bond forming and breaking of proton transfer processes and how the morphing approach can be utilized to extend this method to complex systems which are very difficult to explore using quantum chemical methods. But even one the simplest system, the protonated water dimer, is not fully understood. We had the pleasure to work on proton-bound systems at a time when Asmis and coworker published the first gas-phase infrared spectrum of the protonated water dimer in 2003 (1). One can argue about the quality

---

of this particular spectrum, since there are some unsolved issues concerning the experimental conditions, but without doubt it sparked a firework of papers solely on the infrared spectrum of the protonated water dimer. We present a manuscript of a paper in revision for the Journal of Physical Chemistry on the IR spectra of proton-bound systems in the second part of the Applications chapter. Another chapter contains a paper on double proton transfer reactions. A large part of my thesis consist of the program MMPT implemented in CHARMM, one of the standard molecular dynamics programs today. I hope that the program will prove to be useful to many others and therefore included some technical instructions for interested users at the back.



## 2. Theoretical Background

### 2.1. Molecular Dynamics Simulations

#### 2.1.1. Historical Notes

The pioneering application of the molecular dynamics (MD) method was the investigation of the phase transition of a hard sphere system in the late 1950s by Alder and Wainwright (2, 3). In their studies the particles interact via instantaneous collisions and travel as free particles between collisions. The article of Gibson, Goland, Milgram, and Vineyard appeared in 1960 (4) and is the first example of a molecular dynamics calculation, discussing the creation of defects in copper induced by radiation damage, with a continuous potential based on a finite difference time integration method. Rahman was another pioneer of molecular dynamics and published a paper about a number of properties of liquid argon using the Lennard-Jones potential (5) in 1964. His computer codes are still in operation in many modern molecular dynamics programs. Verlet calculated the phase diagram of argon in 1967 (6). He introduced a time integration algorithm and a bookkeeping algorithm which both bear his name today and are known as the Verlet integrator and the Verlet neighbor list, respectively. More complex systems were then studied by Rahman and Stillinger in their simulation of water with a realistic potential in 1974.

The complexity of systems under investigation changed tremendously over time. What started as simulations of simple liquids resulted in all-atom simulations of proteins. The first simulation appeared in 1977 with the simulation of the bovine pancreatic trypsin inhibitor (BPTI), a globular polypeptide containing 58 amino acid residues. McCammon, Gelin, and Karplus developed an empirical potential energy function to study the dynamics of a folded BPTI protein (7). Since then it has become one of the most thoroughly studied proteins in terms of structure and folding pathway. The increasing complexity peaked recently in simulations of the complete satellite tobacco mosaic virus (STMV), simulations of up to 1 million atoms for over

50 ns (8).

Today MD simulations of solvated proteins, complexes of proteins and ligands or DNA and lipid systems are routinely found in the literature and have become an established research tool in computational branches of physics and chemistry and their interface to biology to understand the functions of proteins.

### 2.1.2. Foundations

In general in a MD simulation we assume the Born-Oppenheimer approximation to be valid, namely that the rapid motion of electrons average out and all particles can be treated classically. The Hamiltonian  $H$  of a system of  $n$  atoms can be defined as the sum of kinetic and potential energies working on a set of coordinates  $x_i$  and momenta  $p_i$  of each atom  $i$ :

$$H(x_i, p_i) = T(p_i) + V(x_i) \quad (2.1)$$

where the kinetic term  $T$  represents the dynamic properties and the potential term  $V$  represents the static properties of the system. The potential energy functions are most conveniently expressed in terms of bond distances, non-bonded distances, valence angles, torsional (or dihedral) angles and out-of-plane (or improper dihedral) angles. The potential energy is therefore usually defined through internal coordinates instead of Cartesian coordinates:

$$V(x_i) = V(r_b, r_{nb}, \theta, \phi, \psi) = V_b(r_b, \theta, \phi, \omega) + V_{nb}(r_{nb}) \quad (2.2)$$

where  $r_b$  are bond distances,  $\theta$  are valence angles,  $\phi$  are torsional angles,  $\psi$  are out-of-plane angles, and  $r_{nb}$  are non-bonded distances describing the molecular system. The intramolecular terms combined in  $V_b$  describe the strain energy in the molecular structure compared to a relaxed equilibrium structure and they often have the form of harmonic strain potentials. In case of the bonded potential this can be expressed through harmonic functions in which the particle exhibits perfect oscillations around the equilibrium distance.

$$V_{bond} = \frac{1}{2} \sum_i^n k_{b,i} (r_i - r_{0,i})^2 \quad (2.3)$$

Using this functional form, the bonded potential describes the strain energy of separating two bonded atoms at distance  $r_n$ , where  $r_0$  represents the separation at the potential minimum energy for the specified bond type and  $k_b$  is the force constant. Although this is a simplification of the potential energy of bond stretch vibrations it reproduces accurately the potential around the equilibrium. Potential energy expressions describing the intramolecular interactions regarding the valence angles and out-of-plane angles have the same harmonic form:

$$V_{bend} = \frac{1}{2} \sum_i^n k_{\theta,i} (\theta_i - \theta_{0,i})^2 \quad (2.4)$$

$$V_{improper} = \frac{1}{2} \sum_i^n k_{\omega,i} (\omega_i - \omega_{0,i})^2 \quad (2.5)$$

where  $k_{\theta,i}$  and  $k_{\omega,i}$  are the corresponding force constants. The torsional degree of freedom  $\phi$  is described through a periodical cosine potential having a periodicity  $n$

$$V_{torsion} = \sum_i^n k_{\phi,i} (1 - \cos(n\phi_i - \delta)). \quad (2.6)$$

Further potential energy expressions include intermolecular terms, that describe the Coulomb and Lennard-Jones interaction between atoms separated by three or more bonds. These non-bonded interaction terms are evaluated between atom pairs to yield the intermolecular energy

$$V_{nb} = \sum_{i<j} (q_i q_j e^2 / r_{ij}) + 4\epsilon_{ij} ((\sigma_{ij}/r_{ij})^{12} - (\sigma_{ij}/r_{ij})^6) \quad (2.7)$$

Additional parameters to complete the force constants are the partial charge  $q$  and a van-der-Waals radius  $\sigma$ . The combination of potential functions and parameters, like force constants and equilibrium distances, constitute the so-called force field. Commonly used force fields for biomolecular and organic systems such as CHARMM (9), and its descendants AMBER (10), GROMOS (11) and OPLS (12), follow this format with only minor changes. The particular form of energy expressions presented in Eqs. 2.3 to 2.7 are used in the CHARMM force field (13). It is obvious that these functional forms represent a certain reduction of the complexity of molecular energetics. They are applied as a compromise between accuracy and speed. More complex force fields

have been developed that add, for example cubic and quartic terms to Eqs. 2.3 and 2.4 to take anharmonicity and stretch-bend cross-terms into account, or that replace the Lennard-Jones function with more flexible Buckingham or Morse potentials. Such force fields, including MM4 and MMFF, were developed to yield accurate structures or vibrational structures for isolated molecules in the gas phase but have not been used regularly in more computer-time demanding fluid simulations.

## 2.2. Simulation of proton transfer reactions

Chemistry textbooks often depict proton transfer as not only the simplest, but also an ubiquitous reaction. While ubiquitous it certainly is, that it is the simplest reaction might be debated. Proton motion can be very fast occurring on the timescale comparable to the period of vibration. On the other hand, the time necessary for the encounter between reaction partners, a proton donor and acceptor, can be quite long and is dictated for example by the diffusion coefficients. Opposed to the latter situation is the case when the reaction occurs along the preformed hydrogen bond. The involvement of all these factors makes it sometimes quite difficult to define a proper coordinate of the proton transfer reaction to find the rate-determining step, which is, of course necessary for understanding the kinetics of the reaction. In many systems the reaction can therefore be controlled by conformational characteristics. Such a situation is encountered, for instance, in the active site of enzymes where amino acid side chains can exist in two or more rotameric forms, of which only one is capable of forming an intramolecular hydrogen bond. In this case, it is the interconversion between rotamers, not the proton movement itself, that may turn out to be the rate-limiting factor for the proton transfer process. To gain a better understanding of the dynamics during the proton transfer reactions it is therefore advantageous not having to make any a priori assumptions about the possible pathways. Molecular dynamics simulations can be a very useful tool in this respect because we are not forced to put any constraints on the system. We can observe the whole system and all degrees of freedom and analyze their role in the proton transfer reaction.

### 2.2.1. Hybrid quantal/classical methods

Common force fields used in MD simulations are not appropriate for the description of processes involving bond forming and breaking. Quantum chemical methods are

usually required. The use of quantum chemical methods is normally only applicable for systems of small size and not for large complex systems, such as enzymes. However, the the region of space in which changes in electronic structure occur is often relatively small compared to the whole system. This situation is taken into account in hybrid quantal/classical or quantum mechanical and molecular mechanical QM/MM models, where the reactive part is treated with quantum chemical methods and the surrounding environment is described by a classical MM force field (14–16). The effective Hamiltonian  $H$  for the complete system can be written as

$$H = H_{QM} + H_{MM} + H_{QM/MM} \quad (2.8)$$

where  $H_{QM}$  account for the interaction energy between all quantum mechanical particles,  $H_{MM}$  accounts for the interaction energy of all classical particles with one other, and  $H_{QM/MM}$  accounts for the energy of interactions between quantum and classical particles.

A number of research groups have combined quantum chemical methods with molecular mechanics programs to study enzymatic reactions. The incorporated methods vary in the level of theory employed. In principle it is possible to interface any *ab initio* quantum chemistry method, like Hartree-Fock (HF) methods (e.g. restricted and unrestricted HF) and Post-Hartree-Fock methods (like MP2), with a MD program. The use of current *ab initio* simulation methods are computationally very demanding, and therefore restricted in their application to short simulation times. More often than not the QM part is therefore described using semi-empirical quantum chemistry methods that are based on the Hartree-Fock formalism but make many approximations and obtain some parameters from empirical data. AM1 and PM3 are such semi-empirical methods which are often used in hybrid QM/MM simulations and have been calibrated to increase their chemical accuracy in respect of proton transfer reactions (17).

Besides methods based on molecular orbital theory there are methods devised on valence bond theory. Warshel (18) established the empirical valence bond (EVB) method together with ideas of combining QM with MM methods for calculations of reactions in solutions and enzymes. At the heart of the EVB methods is the notion that arbitrarily complex reactions may be modeled as the influence of a surrounding environment on a process that may be presented by some combination of valence bond resonance structures. The basic idea of the VB treatment is to obtain the poten-

tial in terms of mixing between relevant states, where each state represents a specific bonding configuration. In a sense the EVB description is therefore much like a molecular mechanics representation of a chemical system. Although the general VB theory fell out of fashion in the chemical community its EVB descendant has been further developed and used regularly. In studies of proton transfer in acetylacetone Hinsen and Roux (19) makes use of the EVB approach developed by Warshel to combine standard molecular mechanics potentials for the reactant and product states to reproduce the interconversion between these two states. Recently Braun-Sand *et. al.* simulated the proton transport in carbonic anhydrase by EVB-based models (20).

Other quantum chemical methods that enjoys great popularity are density functional theory (DFT) methods (21, 22). Of the zoo of DFT functionals that are available today, perhaps the most prominent is the B3LYP functional (23, 24), where the hybrid DFT exchange functional, in this case from BLYP, is combined with the exact exchange functional from Hartree-Fock theory.

The self-consistent charge density functional tight-binding (SCC-DFTB) scheme (25) is another method that becomes increasingly popular. It is a general semi-empirical DFT based approach and is used as a method of choice in hybrid QM/MM with classical MM force fields (26) in simulations of biological systems, e. g. to study the proton transfer in the enzyme liver alcohol dehydrogenase (27). Although the computational speed of SCC-DFTB is very appealing for simulations of reactions in biological systems, the descent of SCC-DFTB from DFT inherits not only the qualities but also the underestimation of proton transfer barriers from DFT methods. The accuracy of any method to reproduce the proton transfer barriers is a major concern and the accuracy of SCC-DFTB regarding PT reaction barriers has been discussed recently (28).

The use of hybrid QM/MM simulation methods is not free of complications either. Questions arise where the boundary between QM and MM region is drawn, sometimes this choice is obvious but more often it is not trivial. Connected with the boundary is the problem how to correctly describe the interface between the two regions.

### 2.2.2. Reactive force fields

Proton transfer potentials have been calculated and fitted to functional forms in the past (29, 30) but are not found in the standard classical MD force field outlined ear-

lier. The reason is the challenge to describe the bond formation and breaking of the reaction. Reactive force fields are notoriously difficult to develop and their accuracy has to be established for each application. The ReaxFF force field (31), for instance, is one which is under active development and has been used to study many chemical reactions involving hydrocarbons.

### 2.3. Morphing of *ab-initio* based potential energy surfaces

The word 'morphing' is used as descriptive term for a mathematical transformation that converts an original potential energy surface (PES) into a new one (32, 33). If one imagines the PES as an elastic rubber sheet than we would be able to compress or stretch it and by doing so change the topology of the surface. We could increase barrier heights and move around the minima or transition points of our PES if we find the right morphing transformation like we can change features on a rubber sheet. The idea of morphing has its origins in the deficiencies of early *ab-initio* calculations. They could not be trusted to give reliable well depths for intermolecular systems. During the 1990s much progress was made in the spectroscopy of Van der Waals complexes. Spectra that probed the stretching and bending modes were extremely valuable to determine intermolecular potentials. The increasing number of experimental results lead to reliable empirical potentials for a range of molecular systems. These empirical potentials for prototype systems made it possible to evaluate the quality of theoretical methods and it was found that to reach spectroscopic accuracy certain scaling functions had to be applied to the *ab initio* potential. Although current state-of-the-art *ab initio* calculations of PESs are highly accurate it is usually still necessary to adjust the *ab initio* potential in order to account for small errors due to basis set and incomplete description of electron correlation. The morphed potential is related to the original *ab initio* potential by applying coordinate dependent scaling functions  $\lambda(\vec{r})$  to the original potential

$$V_{morph}(\vec{r}) = \lambda(\vec{r})V_{orig}(\vec{r}). \quad (2.9)$$

The morphing transformation is found by determining the parameter of the scaling function by least-square fitting to experimental data or in our applications to theoretical data. It is also possible to use this method to circumvent the problem that

---

calculation of high quality *ab initio* PESs for a large molecular system is very excessive in computer-time. Accurate PESs describing the proton transfer reaction of small prototype systems can be transformed to PESs of much larger systems where a similar construction of PESs would be computationally very demanding. In addition the morphing can be used in its original concept to improve the PESs whenever further experimental results become available.



## 3. Applications

### 3.1. Reactive force fields for proton transfer dynamics

#### 3.1.1. Introduction

MMPT, which stands for molecular mechanics with proton transfer, is our newly developed force field for molecular dynamics simulations of proton/hydrogen transfer reactions. The foundation on which our force field rests is the molecular dynamics (MD) program CHARMM (9) (13). It comes with a number of tools and molecular force fields to study macromolecular simulations of proteins. It has become one of the standard MD programs for biomolecular simulations. The main advantages of our approach resides in the speed, accuracy, and interactivity of the MMPT routine. The MMPT routine was designed to deliver an accurate model of the proton transfer reaction in various chemical and biological environments, while allowing the user to remain part of the modeling process through the illustrated interactive morphing approach (32).

#### 3.1.2. Method

##### Prototype systems and *ab initio* PES

Interesting systems for theoretical investigations of PES of proton transfer reactions are molecular systems of small size, because *ab initio* calculations can be performed at sufficiently high level of theory and large enough basis sets can be employed to capture all the intrinsic complexities of this reaction. With the biochemistry of enzymatic proton transfer reactions in mind, especially molecular complexes where nitrogen or oxygen atoms serve as donor or acceptor atoms, we choose systems with the recurring motif of O–H–O, N–H–N, and N–H–O proton bridges (34). Our prototype systems are the protonated homo dimer of water  $[\text{O}_2\text{H}_5]^+$  and ammonia  $\text{NH}_4^+ \cdots \text{NH}_3$  as well as the hetero dimer of protonated ammonia and water  $\text{NH}_4^+ \cdots \text{H}_2\text{O}$ . The structures

of these three molecular systems are shown in Fig. 3.1.

The coordinate system of the PES of the proton transfer reaction can be defined through the proton-donor distance  $r$ , the donor-acceptor distance  $R$  and angular distortion  $\theta$ . For the fitting procedure it is advantageous to define a dimensionless internal reaction coordinate  $\rho = (r - r_{\min}) / (R - 2r_{\min})$  to describe the proton position with respect to  $r$  and  $R$ , where  $r_{\min} = 0.8 \text{ \AA}$ . This transformation maps  $r$  to the range of  $\rho \in [1, 0]$  which considerably simplifies and stabilizes the fitting, particularly with respect to a possible Legendre expansion. The closest bond length  $r_{\min}$  between proton and donor or acceptor atom, can be found at  $\rho = 0$ , respectively  $\rho = 1$ . The midpoint along the reaction coordinate is then always found at  $\rho = 0.5$  irrespectively of the given donor-acceptor distance  $R$ .

The symmetry of the proton-bound homo dimers  $[\text{O}_2\text{H}_5]^+$  and  $\text{NH}_4^+ \cdots \text{NH}_3$  can be used to reduce the number of necessary evaluation points of the *ab initio* PES and subsequently the number of necessary fitting parameters. For both systems a fully relaxed three-dimensional PES scan on a grid for the relevant proton transfer coordinates  $(R, r, \theta)$  were completed using MP2/6-311++G(d,p) (35) (36) (37). The choice to use the Møller-Plesset perturbation theory to second order (MP2) as the level of theory is a good compromise between the accuracy of the level of theory and the computational speed. DFT methods seem to underestimate the barriers substantially, while Hartree-Fock (HF) overestimates them largely because of the neglect of electron correlation effects. Other possibilities are to include perturbation theory with higher order (MP3 or MP4) or other post-Hartree-Fock methods like configuration interaction (CI)(38) or coupled cluster (CC) (39) methods but the computational cost of such procedures is very expensive relative to that for HF or MP2. Another consideration is the size of the basis set. One can assume that the relatively large basis set used here minimizes the effect of basis set superposition errors, and that the addition of diffuse and polarization basis functions increases the accuracy of the energy calculations of the barrier for large values of  $R$ , in particular at the transition state. Larger basis set like aug-cc-pVDZ or even aug-cc-pVTZ are again of very high computational cost and at the moment not applicable to fully relaxed PES scan of the size presented here. All *ab initio* calculations were carried out with Gaussian03 (40). The grid for  $[\text{O}_2\text{H}_5]^+$  was defined by  $R \in [2.2, 3.2] \text{ \AA}$  and for  $\text{NH}_4^+ \cdots \text{NH}_3$  by  $R \in [2.4, 3.4]$  in increments of  $0.1 \text{ \AA}$  and  $r$  between  $0.8 \text{ \AA}$  and the midpoint between the donor and acceptor atoms in increments of  $0.05 \text{ \AA}$  and at angles  $\theta = 0^\circ, 11.98^\circ, 27.49^\circ, 43.10^\circ, \text{ and } 58.73^\circ$ . The angular grid was chosen to guarantee an efficient and stable representa-

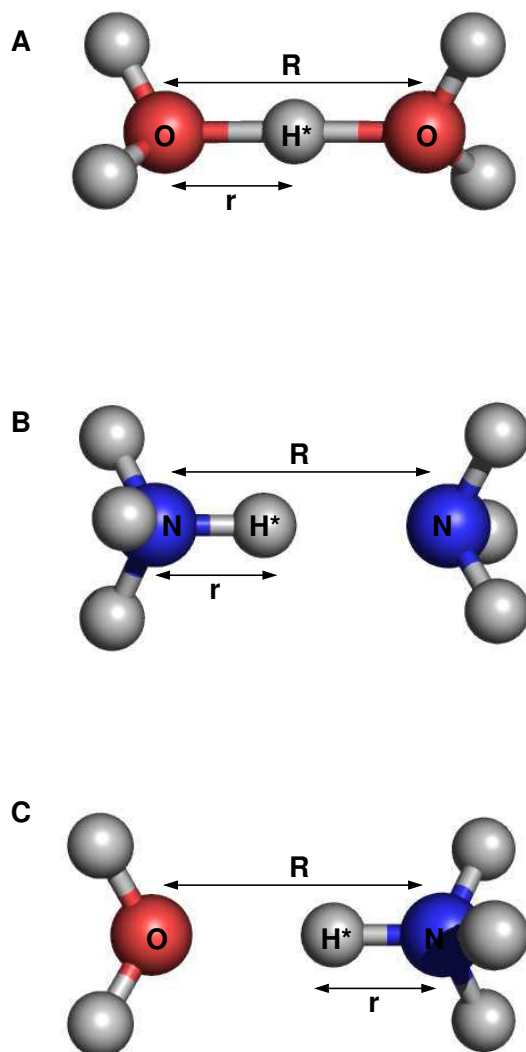


Figure 3.1: Prototypical proton transfer systems. (A) Protonated water dimer  $[O_2H_5]^+$ . (B) Protonated ammonia dimer  $NH_4^+ \cdots NH_3$ . (C) Protonated ammonia-water dimer  $NH_4^+ \cdots H_2O$ .

tion of the angular dependence by Legendre polynomials to describe internal rotation of the molecules. The symmetric PES of  $[\text{H}_5\text{O}_2]^+$  features a single minimum as can be seen in fig 3.2, whereas the PES of  $\text{NH}_4^+ \cdots \text{NH}_3$  shows two minima. The asymmetric PES of  $\text{NH}_4^+ \cdots \text{H}_2\text{O}$  is also shown in fig 3.2. It shows a single minimum, where the proton is in the bound state of the ammonium ion  $\text{NH}_4^+$ . The PES has been scanned on the same grid as  $\text{NH}_4^+ \cdots \text{NH}_3$ .

### Symmetric potential energy functions

The PES of the homo dimer prototype systems can be best described by symmetric potential functions. Many analytical functions have been devised (41, 42) and Morse functions have been shown to be adaptive enough to successfully describe the topology of the PES of proton transfer reactions. The symmetry can be utilized by defining a mirror plane along the midpoints  $\rho = 0.5$  for any given  $R$  and applying a second Morse function with a inverse position coordinate  $\rho$ . The total potential energy surface is given by the following equation:

$$\begin{aligned} V_{PT}(R, \rho, \theta) &= D_{eq}(R)[1 - \exp(-\beta(R)(\rho - R_{eq}(R)))]^2 \\ &+ D_{eq}(R)[1 - \exp(-\beta(R)(1 - \rho - R_{eq}(R)))]^2 \\ &- D_{eq}(R) - c + k\theta^2 \end{aligned} \quad (3.1)$$

where the parameters  $D_{eq}$ ,  $\beta$ , and  $R_{eq}$  are functions of  $R$ , and  $c$  and  $k$  are constants:

$$D_{eq}(R) = p_1(1 - \exp(-p_2R - p_3))^2 + p_4 \quad (3.2)$$

$$\beta(R) = p_5 + p_6R \quad (3.3)$$

$$R_{eq}(R) = p_7 \exp(-p_8R) + p_9 \quad (3.4)$$

$$k = p_{10} \quad (3.5)$$

$$c = p_{11} \quad (3.6)$$

The functional expressions for  $D_{eq}(R)$ ,  $\beta(R)$  and  $R_{eq}(R)$  using the fit parameters  $p_i$  were found to give the best fitting results. For strongly proton-bound systems a harmonic term for the angular part is a good approximation. To describe internal rotation (e.g. reorientation of  $\text{H}_3\text{O}^+$  in liquid water) such an expansion is not sufficient. It is, however, worthwhile mentioning that an 11-point Legendre expansion in  $\theta$  yields a very satisfactory fit of the full three dimensional potential. The potential energy

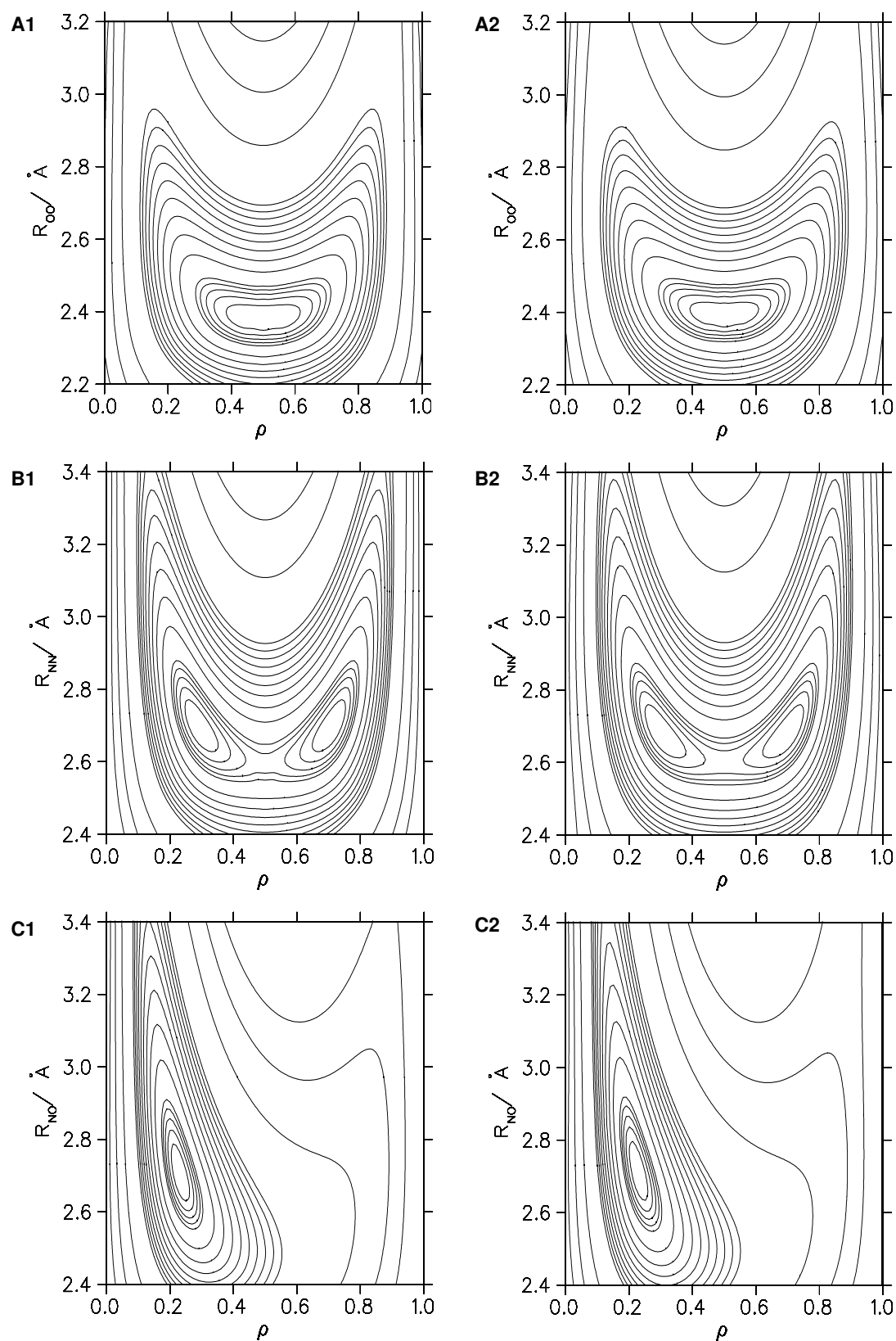


Figure 3.2: Comparison of *ab initio* (left column) and MMPT (right column) of relaxed PES from scanning the fully optimized PES. (A)  $\text{OH}_3^+ \cdots \text{OH}_2$ , (B)  $\text{NH}_4^+ \cdots \text{NH}_3$  and (C)  $\text{NH}_4^+ \cdots \text{H}_2\text{O}$ . Contour lines are drawn at intervals of 0.2 kcal/mol for energies below 1 kcal/mol, for energies between 1 and 10 kcal/mol at intervals of 1 kcal/mol and at intervals of 10 kcal/mol for higher energies.

functions can be used in classical, as well as in quantum or mixed quantum-classical molecular dynamics simulations.

### Asymmetric potential energy functions

In contrast to symmetric systems we need two independent descriptions of the donor and acceptor side to describe the asymmetry. We find that Morse functions have the necessary flexibility to describe the PES also when we deal with asymmetric systems. The total potential energy surface is completely defined by the following equation:

$$\begin{aligned} V_{PT}(R, \rho, \theta) &= D_1(R)(1 - \exp(-\beta_1(R)(\rho - R_1(R))))^2 \\ &+ D_2(R)(1 - \exp(-\beta_2(R)(R_2(R)) - \rho))^2 \\ &- c(R) + k\theta^2 \end{aligned} \quad (3.7)$$

where the parameters  $D_i$ ,  $\beta_i$ ,  $R_i$ , and  $c$  are functions of  $R$ , and  $k$  is a constant:

$$D_1(R) = p_1(1 - \exp(-p_2(R - p_3)))^2 + p_4 \quad (3.8)$$

$$\beta_1(R) = \frac{p_5}{1 - \exp(-p_6(R - p_7))} \quad (3.9)$$

$$R_1(R) = p_8(1 - \exp(-p_9(R - p_{10})))^2 + p_{11} \quad (3.10)$$

$$D_2(R) = p_{12}(1 - \exp(-p_{13}(R - p_{14})))^2 + p_{15} \quad (3.11)$$

$$\beta_2(R) = \frac{p_{16}}{1 - \exp(-p_{17}(R - p_{18}))} \quad (3.12)$$

$$R_2(R) = p_{19}(1 - \exp(-p_{20}(R - p_{21})))^2 + p_{22} \quad (3.13)$$

$$c(R) = p_{23}(1 - \exp(-p_{24}(R - p_{25})))^2 + p_{26} \quad (3.14)$$

$$k = p_{27} \quad (3.15)$$

The choices for  $D_i(R)$ ,  $\beta_i(R)$ ,  $R_i(R)$ , and  $c(R)$  ensure proper short and long range behavior. Morse functions have the desired properties to be repulsive at short range and for long range they become constant. Sigmoid functions become constant at short ranges.

### Legendre expansion of potential functions

As mentioned before it is also possible to separate the bond variables  $(R, \rho)$  and the angle variable  $\theta$  through a Legendre expansion. The potential function can then be

expressed as

$$V(R, r, \theta) = \sum_{\lambda=0}^n V_{\lambda}(R, r) \cdot P_{\lambda}(\cos \theta), \quad (3.16)$$

where  $P_{\lambda}(\cos \theta)$  are the corresponding Legendre polynomials. The expansion allows to treat  $V_{\lambda}(R, \rho)$  and  $P_{\lambda}(\cos \theta)$  separately. The curve fitting gave best results when  $V_{\lambda}(R, \rho)$  was of the form

$$\begin{aligned} V_{\lambda}(R, \rho) &= D(R)[1 - \exp(-\beta_1(R)(\rho - R_e(R)))]^2 \\ &+ D(R)[1 - \exp(-\beta_1(R)(1 - \rho - R_e(R)))]^2 \\ &+ c(R) \exp(-\beta_2(R)(\rho - 0.5))^2 \quad \text{for } \lambda = 0 \end{aligned} \quad (3.17)$$

using two Morse functions, plus a Gaussian function centered at the transition state for  $V_0$ . The peak like shape of higher order terms of  $V_{\lambda}$  is best described by a Lorentzian peak function. The Lorentzian line shape is characterized by having a very sharp narrow peak with most of the intensity of the peak located in the tails which extend into infinity. We add an additional parameter  $\delta$  to take into account that here the tails do not tend to zero and center the function at the transition state.

$$V_{\lambda}(R, r) = \frac{H_{\lambda}(R)}{4 \left( \frac{\rho - 0.5}{w_{\lambda}(R)} \right)^2 + 1} + \delta_{\lambda}(R) \quad \text{for } \lambda > 0. \quad (3.18)$$

The various parameters  $D_{eq}, \beta_1, \beta_2, R_{eq}, c, H_{\lambda}, w_{\lambda}, \delta_{\lambda}$  are modeled as linear functions in  $R$ .

### 3.1.3. Implementation

The CHARMM program (9) allows the user to interact directly with the main program by providing an user defined energy term. We use this feature to implement our ideas of a proton transfer energy term into the well-developed molecular dynamics program. We combine in the user energy term all necessary actions to seamlessly incorporate the molecular mechanics proton transfer force field by introducing our definition of the user energy term

$$\begin{aligned} E_{user} &= E_{bridge} \\ &+ E_{bond} + E_{angle} + E_{dihedral} + E_{improper} \\ &+ E_{Coulomb} + E_{vdW} \end{aligned} \quad (3.19)$$

Initially the hydrogen atom  $H^*$  is in a bound state, which is recorded in the protein structure file (PSF), where all conformational connections like bonds, angles, dihedral angles, and improper dihedral angles are stored. We will make intensive use of the information in the PSF to initialize and control the MMPT routine. The initialization determines which bonded and non-bonded interactions need to be removed or modified. The user can define multiple hydrogen bridges in an external file. The transferring hydrogen and its donor and acceptor atoms are identified in the hydrogen bridge file through their unique number in the PSF. The according PSF numbers have to be given in an order such that the numbering is: acceptor atoms first, secondly the transferring hydrogen atom, and donor atoms come last. In a conventional MD simulation the bonds are defined at the beginning of a calculation and can not be broken or formed subsequently. Additionally the harmonic potential is not capable to describe the dissociation of the bond. However, during the MMPT simulation the functional form of  $E_{bridge}$  allows the atom  $H^*$  to leave the donor atom D and bind to the acceptor atom A, and we need to remove the energy contribution  $E_{bond}$  for the bond between atom D and atom  $H^*$ . Further we need to treat the other intramolecular bonded terms. The angle, dihedral, and improper dihedral terms need to be modified with respect to the progress of the proton transfer. A switch function  $f_{sw}(R, r)$  is used to turn the necessary terms on or off. For this, a sigmoid function  $f_{sw}(R, r) = (\tanh(2R(r - R/2)) + 1)/2$  is chosen, which returns exactly 0.5 at the transition state and values close to one if  $H^*$  is bound to D and zero if  $H^*$  is bound to A. In the same manner some of the non-bonded interactions need to be removed, added or modified. Electrostatic and van-der-Waals contributions are calculated for all atom pairs which are not connected through a bond or an angle. These atom pairs are excluded from the calculation of non-bonded energy terms. Non-bonded energy terms for the hydrogen and acceptor atom and for the acceptor and donor atom are removed completely since these energetic contributions are included in the proton transfer potential, and would otherwise be taken into account twice. Non-bonded energy terms from atom pairs connected through an angle need to be switched off and on accordingly on the donor and acceptor side during the transfer. Atom pairs connected through a dihedral angle are included in the non-bonded calculations. A special case is the calculation of van-der-Waals interactions of aliphatic carbon, and peptide nitrogen and oxygen atoms connected through a dihedral angle. These special van-der-Waals terms use different scaled-down parameter to describe the van-der-Waals interaction between the first and fourth dihedral angle atoms. During a



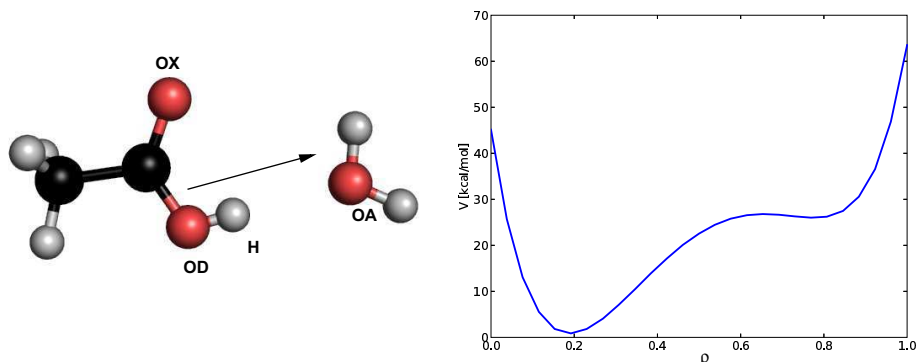


Figure 3.3: Schematic deprotonation of acetic acid  $\text{CH}_3\text{COOH}$  through a water molecule. The proton transfer potential is plotted along the reaction coordinate  $\rho$  for a donor-acceptor distance  $R_{OD-OA} = 2.8 \text{ \AA}$  and a linear configuration of the OHO atoms. The arrow indicates the reaction coordinate.

proton transfer the calculation of van-der-Waals terms must then be switched from a special to standard calculation of the energies on the donor side or vice versa the treatment of special terms on the acceptor side must be switched from standard to special. We achieve this by calculating both, the standard and special case, where necessary and switch these terms on or off accordingly to guarantee a smooth transition from a standard to special treatment of van-der-Waals interactions.

We illustrate some aspects of the described implementation using the deprotonation of acetic acid as an example. We monitor the energy terms during the proton transfer from the acetic acid to an acceptor side, here exemplified by a water molecule. The molecular structure and the proton transfer potential along the reaction coordinate is shown in Fig. 3.3 The switching of angle terms is shown for an interaction at the acceptor side and at the donor side in Fig. 3.4. Dihedral and improper dihedrals and non-bonded interactions are switched on or off in the same way. The switch

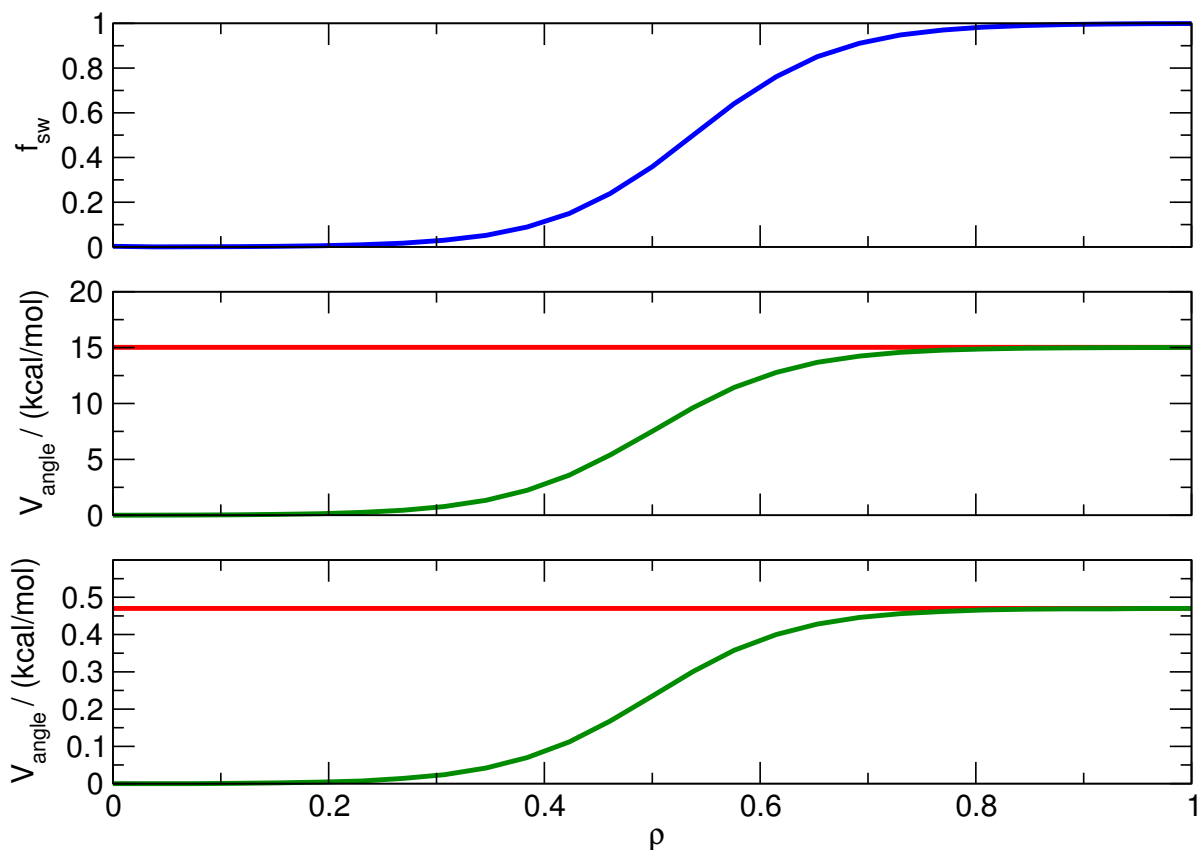


Figure 3.4: Upper panel: Switch function along the reaction coordinate for the conformation in Fig. 3.3. Middle panel: Angle energy of the existing angle formed by the transferring hydrogen atom H, the donating oxygen atom OD and the carbon atom of the acetic acid (red curve) and the correction for the angle energy subtracted from the angle energy (green curve). Lower panel: Angle energy of the new angle formed by the transferring hydrogen atom H, the accepting water oxygen OA and the hydrogen atom of the water molecule (red curve) and the correction added to the angle energy terms (green curve). Note that during the linear transfer of the proton the angles do not change and the angle energy stays constant (red curves) but the MMPT routine returns the angle energy multiplied with the switch function (green curves) which is either subtracted or added.

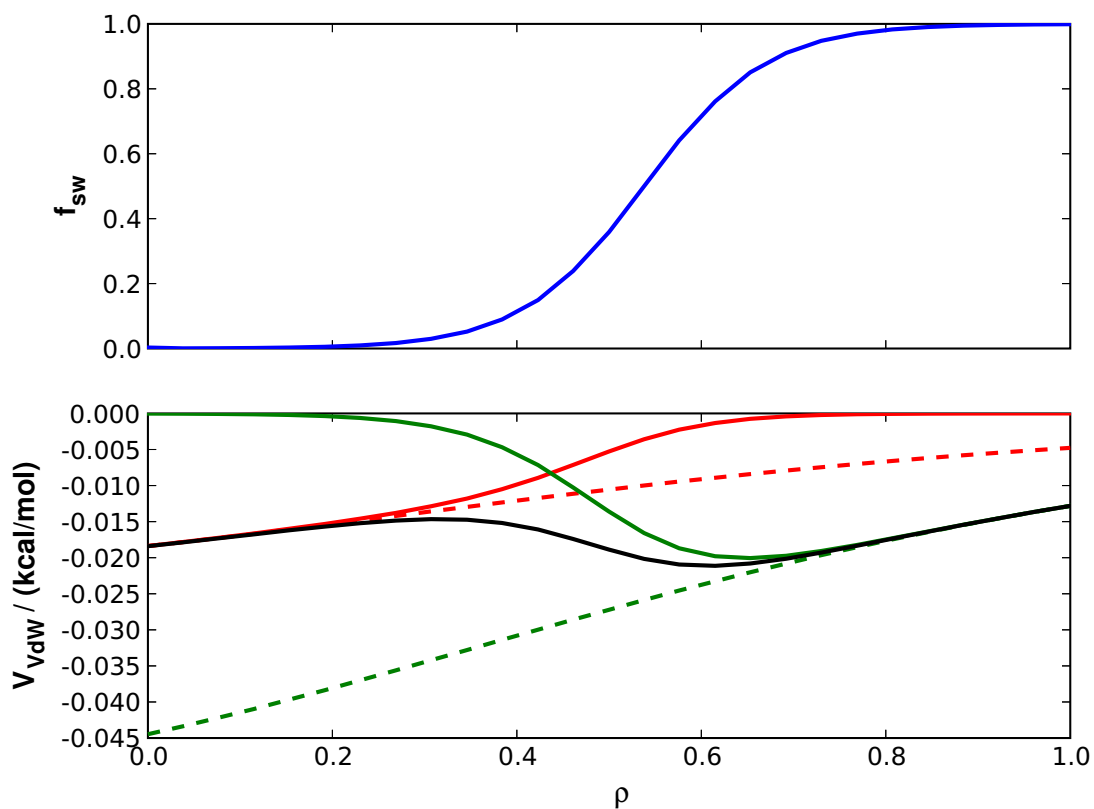


Figure 3.5: Upper panel: Switch function along the reaction coordinate for the conformation in Fig. 3.3. Lower panel: The dashed lines show the van-der-Waals energy of the atom pair of the transferring hydrogen atom H and the unprotonated oxygen atom OX of the acetic acid with special (red) and standard parameter (green). The solid green and red lines are the van-der-Waals energies multiplied with the switch function and the black line is the value returned by MMPT routine to ensure a smooth transition.

between standard and special van-der-Waals parameters is explained in Fig. 3.5.

### 3.1.4. Morphing Transformations

The three model systems of typical proton bound dimers show that the same functional form is suited for a successful fitting that reproduces symmetric and nearly symmetric potential energy surfaces as well as asymmetric PES with only one energetic minimum. Although it is in principle possible to repeat the fitting process for any desired proton bound molecular system, it is beneficial to recognize the similarities of the proton transfer PES and that they can be put to use to circumvent the computational cost of new PES scans and reduce the laborious task of fitting entirely new parameter sets. By introducing constant scaling factors we are able to change properties of the original PES, like barrier heights or minimum energy geometries. This transformation can be written mathematically as

$$V_{morph}(R', \rho', \theta') = \lambda(R, \rho, \theta)V_{orig}(R, \rho, \theta), \quad (3.20)$$

where the definition of  $\lambda$  can be a plain constant or a complex function of one or more of the coordinates. A natural choice to control the barrier height would then be to introduce a potential scaling, whereas to affect the minimum energy geometries could be achieved by scaling the coordinates  $R, \rho, \theta$ . Several choices of possible morphing transformations are illustrated in the next sections where we present some applications of the MMPT force field.

### 3.1.5. Proton bound homo dimer $\text{NH}_4^+ \cdots \text{NH}_3$

We employed the molecular mechanics proton transfer (MMPT) to study the dynamics of the proton transfer reaction of the proton bound ammonia dimer  $\text{NH}_4^+ \cdots \text{NH}_3$ . The vibrational spectrum of the proton bound dimer has been studied experimentally (43, 44) as has the association reaction leading to the proton bound dimer (45). Theoretical investigations relied on *ab initio* methods (46–49), semi-empirical *ab initio* methods of the AM1 type (50), empirical valence bond methods (51) as well as an approximate density functional theory method, the SCC-DFTB method (52–54), to study the structure and dynamics of the dimer. The reactive MMPT molecular dynamics simulation describes explicitly all degrees of freedom. Particularly the motions of the proton bridge  $\text{N}_d\text{-H}^+ \cdots \text{N}_a$ , formed between the donating  $\text{N}_d$  and accepting  $\text{N}_a$  nitrogen atom, are here naturally coupled to the atoms of the  $\text{NH}_3$  moieties. The MMPT module describes the bond formation and breaking between the proton and the am-

monia molecule  $\text{NH}_3$  to form and dissociate the ammonium ion  $\text{NH}_4^+$ . The dynamics of the atoms forming  $\text{NH}_3$  are described by the conventional CHARMM force field and only the interactions between the donor and acceptor atoms, and the proton, are controlled by the MMPT module.

We ran several MD simulations to generate trajectories at various temperatures. The system was heated every 10 steps by 1 K, followed by a short equilibration phase of 5 ps until the simulation temperature was reached and stabilized. Unconstrained molecular trajectories were recorded during 50 ps for subsequent analysis. A leap-Verlet integrator and a particularly small time step of 0.25 fs was used to capture the very fast hydrogen motions along the proton transfer reactions. In figure 3.6 we see a typical section of a time series of the relevant proton bridge  $\text{N}_1\text{-H}^+\text{-N}_2$  distances. We analyzed the trajectories using the time series of bond distances. To inspect the influence of temperature on the the proton transfer dynamics we counted the number of proton transfer events which occurred during the simulation time. A proton transfer event was registered whenever one of the bond lengths between the nitrogen atoms  $\text{N}_1$  or  $\text{N}_2$  and the proton  $\text{H}^+$  became shorter than the other. To avoid rapid recrossing events entering the statistics we demand that the bond length is also shorter than a certain distance  $r_c$ . In figure 3.6 such a transfer happens when the distances  $\text{N}_1\text{-H}^+$  and  $\text{N}_2\text{-H}^+$  intersect and the bond length continues to decrease below  $r_c$ .

To determine the reaction rate we calculate hazard plots from the distribution functions of residence times (52, 55). We define the residence time as the time passed between the interchange of bound states. The residence times are measured whenever the transition state is crossed and the bond length between the accepting nitrogen atom and the proton drops below the threshold value  $r_c$ . The threshold bond length  $r_t$  ensures that fast recrossings are not considered as completed proton transfer events. A choice of the threshold value in the range  $1.1 \text{ \AA} < r_c < 1.2 \text{ \AA}$  hardly influences the observed number of proton events. The following residence times were always measured with  $r_c=1.15$ . The resulting distribution functions are plotted in Fig. 3.7 for a 1 ns simulation at 300 K. The striking feature within the distribution plot is that the residence times do not tail off evenly but their occurrence is periodically modulated. The peaks in the residence times distribution occur at almost regular periods of about 0.11 ps or about 9 times per ps. This period converts to  $300 \text{ cm}^{-1}$  which is well within the expected frequency range of the N-N stretch vibration. We sort the residence times in ascending order. The ordered residence times are then plotted against the expectation value of the cumulative hazard. The expectation value at the k-th transition is given

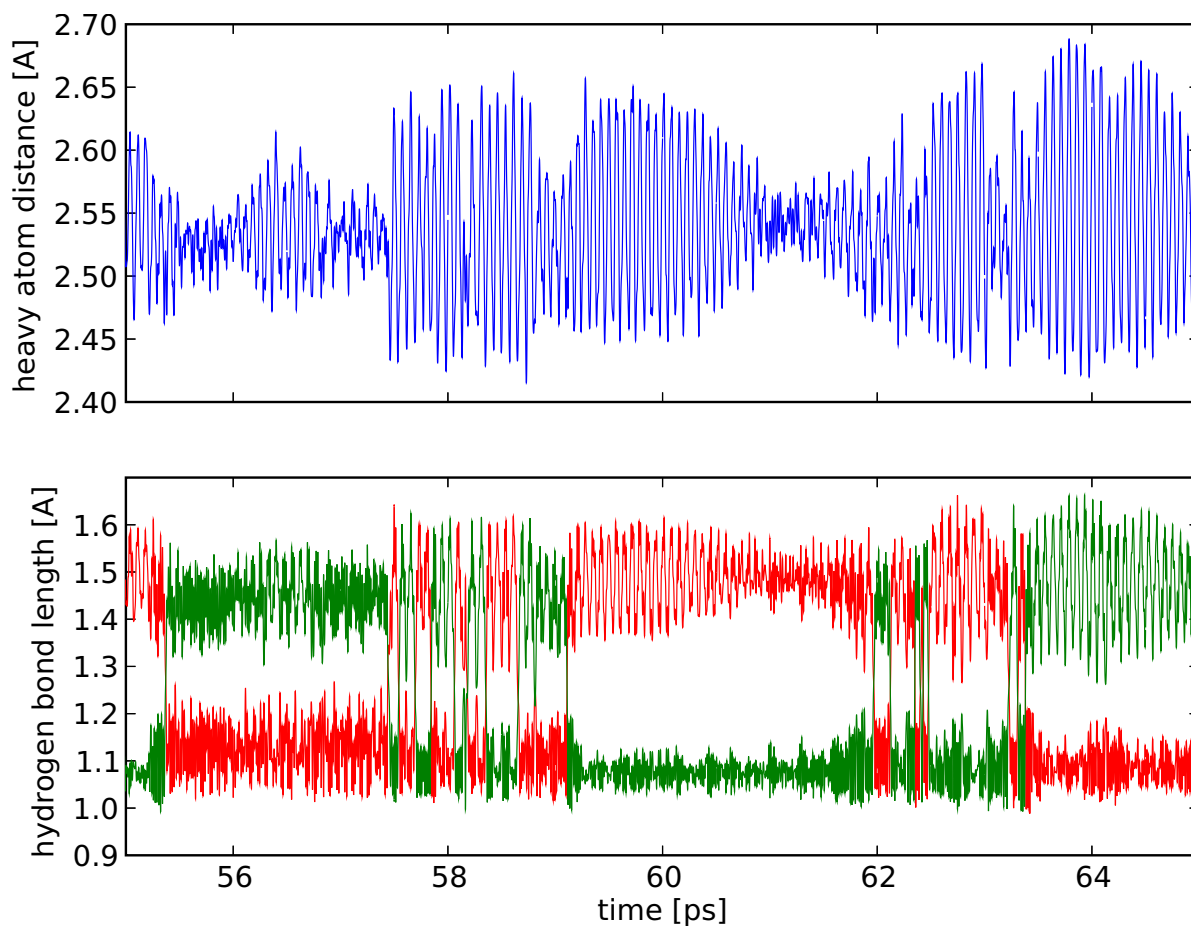


Figure 3.6: This section shows a typical time series of distances of the relevant atoms from a trajectory at  $T = 300$  K. The top panel shows the distance fluctuations of the donor - acceptor distance. The bottom panel shows distances between the nitrogen atoms and the proton,  $N_1-H^+$  shown in green and  $N_2-H^+$  shown in red. This example illustrates the range of residence times from sub-picoseconds up to multiple picoseconds.

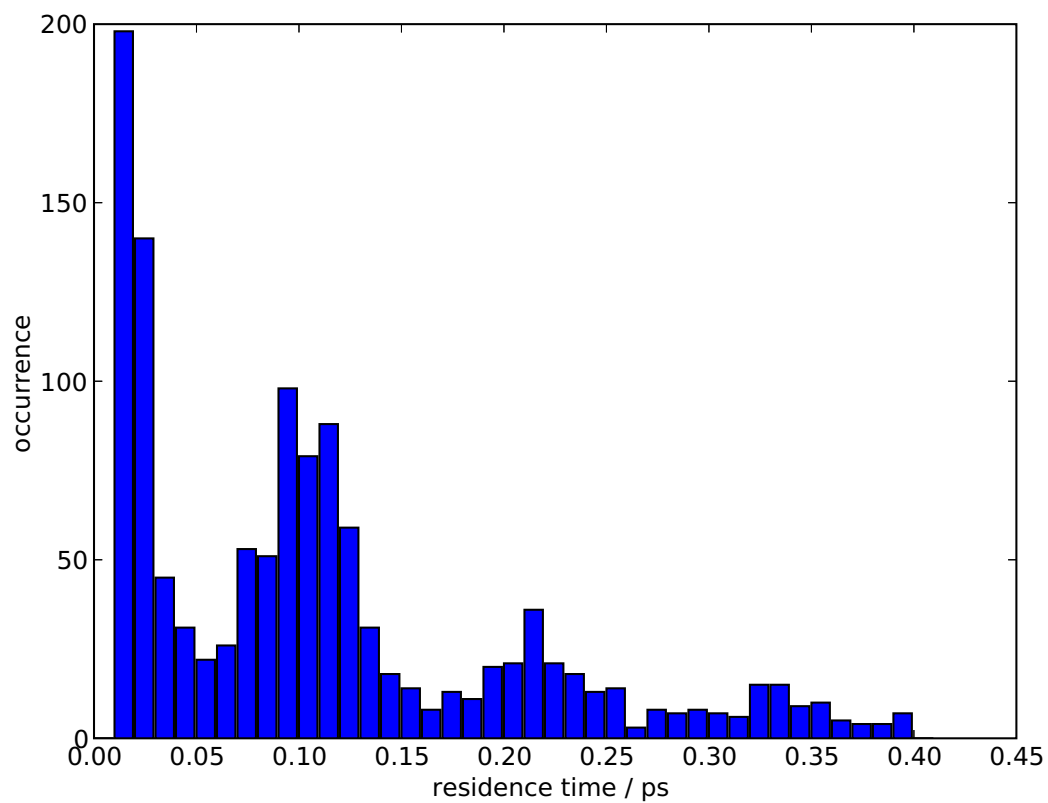


Figure 3.7: The residence time distributions for a 1 ns simulation at 300 K. The majority of residence times fall in the range between 0.01 and 0.4 ps.

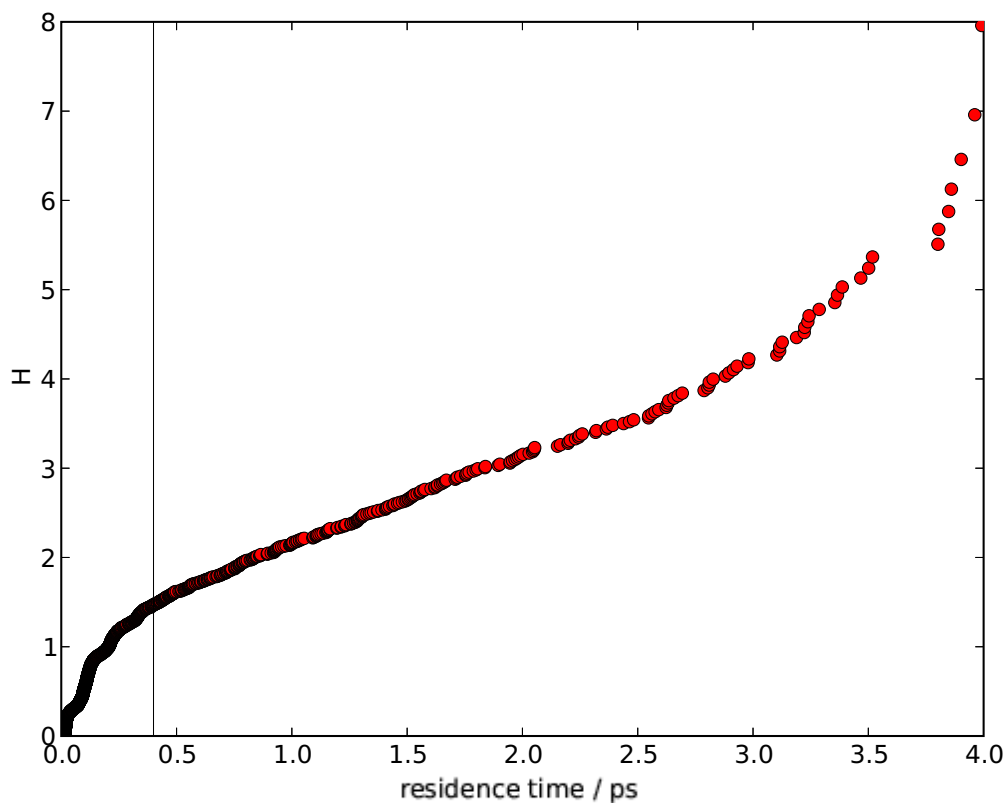


Figure 3.8: Hazard plot from a 1 ns long trajectory at 300 K. Most residence times are found to be short, 1236 out of total 1650 have residence times shorter than 0.4 ps. Rare events exist where long residence times up to 40 ps occur. The vertical line indicates the cutoff for the linear regression fit to determine the slope.

by

$$H_k = \sum_{i=0}^{k-1} \frac{1}{n-i}. \quad (3.21)$$

For a Poisson process the hazard plot follows a straight line and the reaction rate is then given by the slope of this line. The Hazard plot from our example 1ns trajectory is shown in figure 3.8. The hazard plot diverges from a straight line for longer residence times. This agrees with our observation of a periodic pattern in the residence time distributions. To determine the fast reaction rate it is sufficient to restrict the linear regression to short residence times. We found that the length of the simulation does not have a large effect on the residence time distributions. The chosen simulation length assures that about 10 to 100 proton transfer events occur, enough to perform the linear regression. We performed 100 independent 50 ps long trajec-



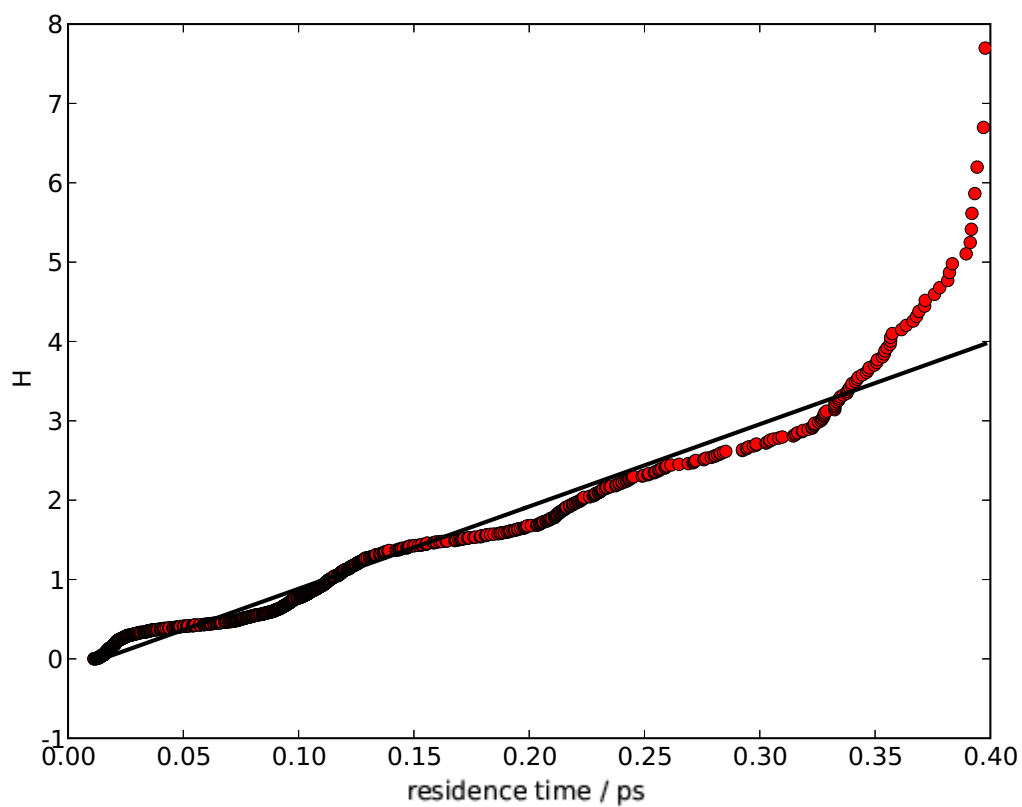


Figure 3.9: Subset of the hazard plot of residence times smaller than 0.4 ps of Fig.3.8. The linear regression fit returns a slope of 10.36.

tories at  $T = 50, 100, 150, 200, 250, 300, 350,$  and  $400\text{K}$  for energy scaling parameters  $\lambda_E = 0.5, 0.75, 1,$  and  $2$  and calculate the average slope of a linear regression fit to the hazard plots in the range of residence times between  $0$  and  $0.4$  ps. All resulting slopes of the linear regression of all reactive trajectories at a given temperature are plotted in a scatter plot where each point is drawn at the slope or reaction rate and the given number of transfer events of a certain trajectory. High temperature trajectories are always reactive, with a high number of transfer events for which the reaction rate can be determined. As the temperature decreases the maximum number of transfer events in the given time is also reduced. For temperatures below  $40$  K the trajectories do not yield any transfer events. From the scatter plots (see Fig. 3.10) we are able to determine an average reaction rate at temperature  $T$ . The average reaction rate as a function of the temperature are shown in Fig. 3.11. The onset of the transfers around  $T = 40$  K marks the steep rise of the reaction coordinate until it quickly reaches a plateau value of about  $10$  crossings/ps relatively constant over the complete investigated temperature range. It appears that the available kinetic energy at a certain temperature is always sufficient to overcome the energetic barrier once it has reached a certain value. The reaction rate is relatively temperature independent once a critical temperature is reached. Through the energy scaling parameter  $\lambda_E$  we are able to control the barrier height of the PES and study the effect on the reaction rates at different temperatures and energy scaling parameters (see Fig. 3.12). Also here we note that the high temperature rate is limited independently of the barrier height. Above a certain temperature the reaction rate stays constant and we find reaction rates in the range from  $8.8$  to  $10$  crossings/ps. Again we can connect this to a frequency range of  $294$  to  $333\text{ cm}^{-1}$ . Calculation of the power spectrum of the time series of  $\text{N}\cdots\text{N}$  distances shows a maximum peak at  $309\text{ cm}^{-1}$ . This coincides with the symmetric stretch vibration  $\text{NH}\cdots\text{N}$  at  $312\text{ cm}^{-1}$  found in frequency calculations at the  $\text{MP2/6-311++G(d,p)}$  level (compare Fig. 3.13).

We computed the potential of mean force along the proton transfer coordinate  $\rho$  for various temperatures  $T$  using the formula

$$V_{PMF} = k_B T \ln[P(\rho)] \quad (3.22)$$

where  $P(\rho)$  is the probability distribution of  $\rho$ , computed as the normalized histogram of the time series  $\rho(t)$  collected during the  $1$  ns long simulations, and  $k_B$  is Boltzmann's constant. The simulation protocol is the same as used to determine the reac-

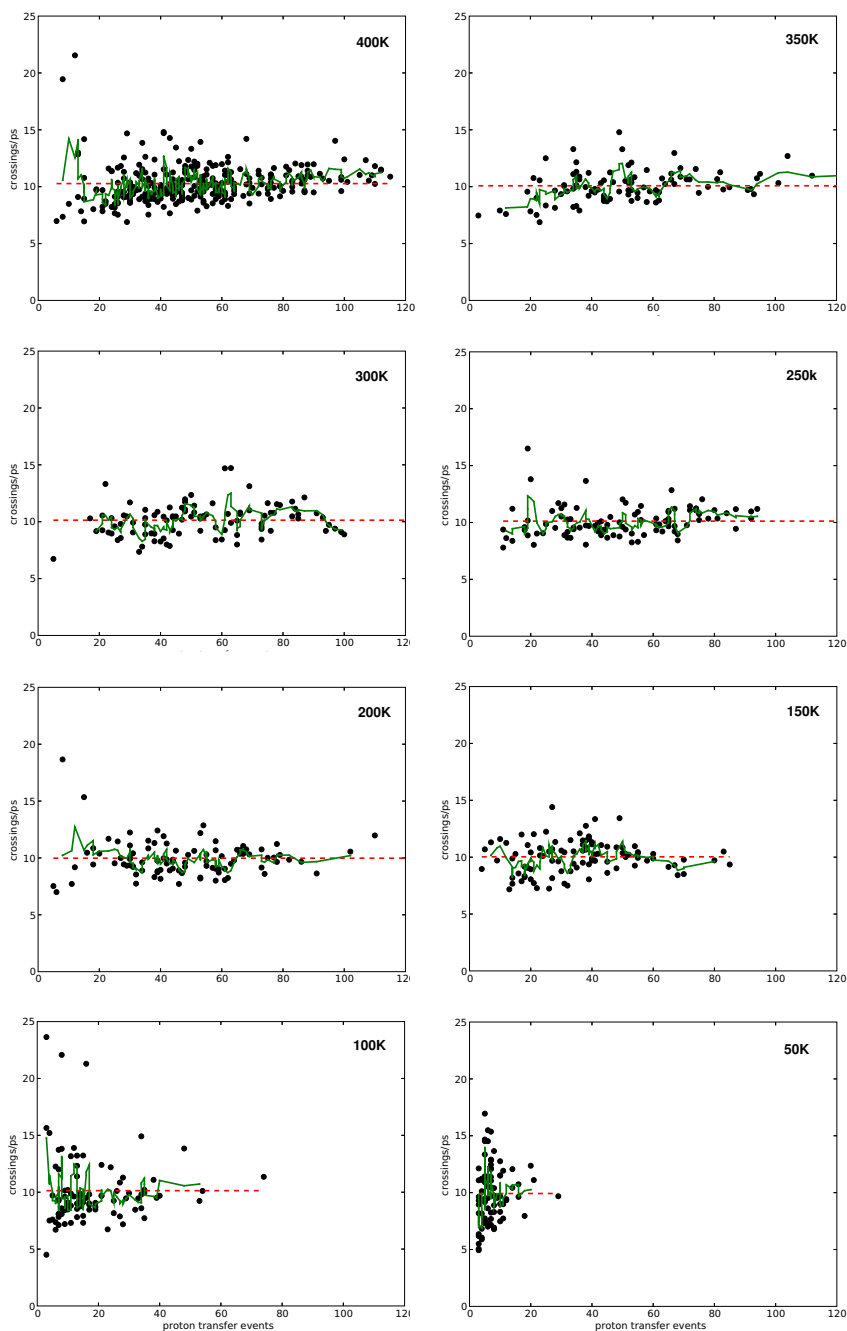


Figure 3.10: Scatter plots of all reactive trajectories show at each point the slope and number of proton transfer events at temperature  $T$ . Running average of the reaction rates are shown as green line and the average value of all reaction rates is indicated as dashed red line.

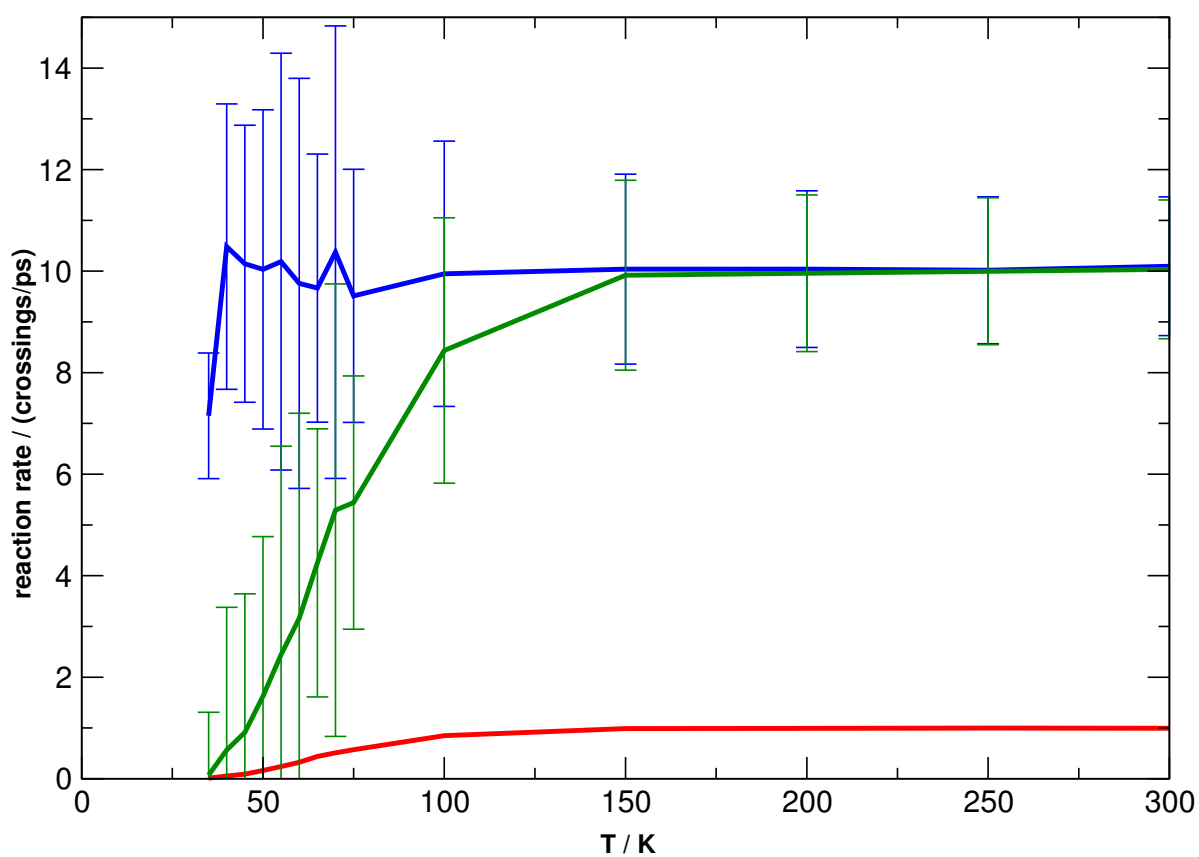


Figure 3.11: Reaction rates from hazard plots of residence times for 500 trajectories at each temperature. The blue curve shows the calculated rate from reactive trajectories only, whereas the green curve is the rate weighted by the ratio of the number of reactive over the number of total trajectories (red curve).

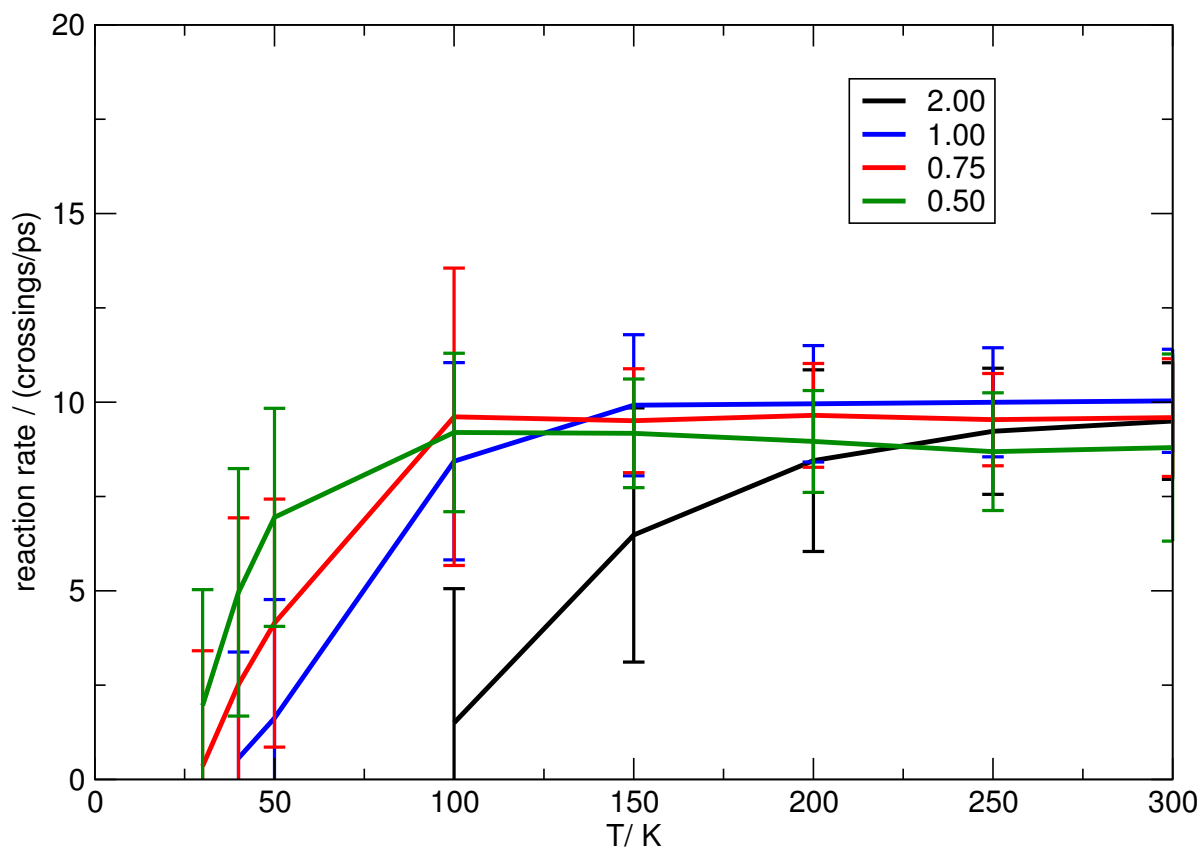


Figure 3.12: Reaction rates from hazard plots of residence times for 500 trajectories at each temperature with various energy scaling factors  $\lambda_E$ .

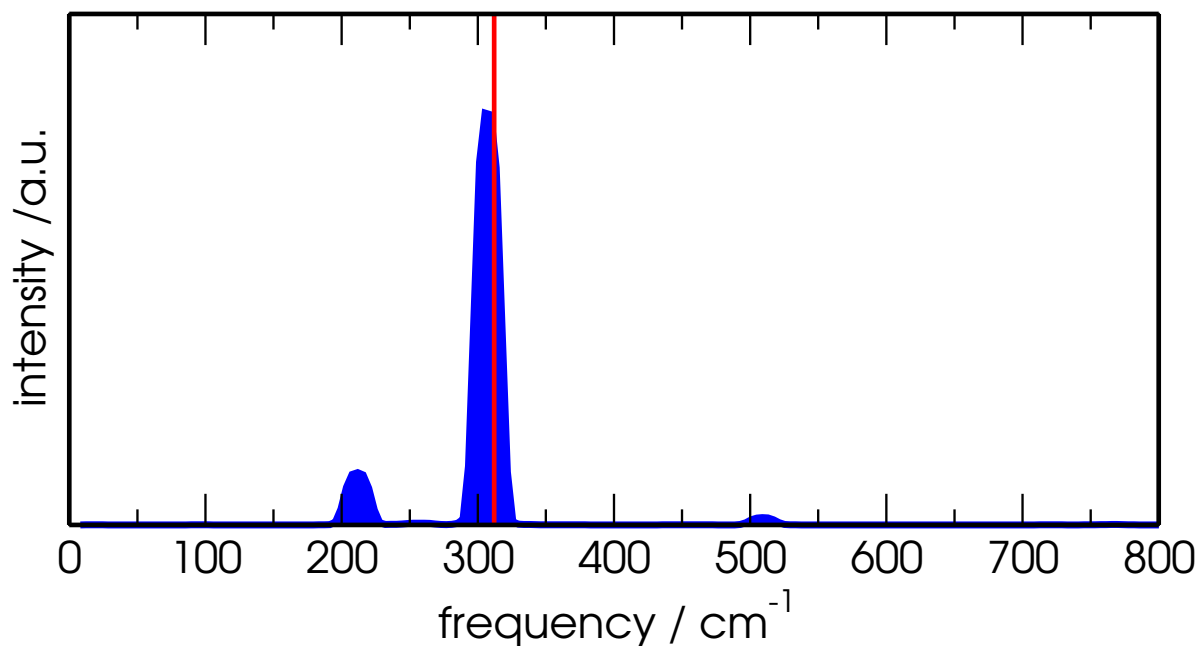


Figure 3.13: Power spectrum of the N $\cdots$ N distance (blue curve). The maximum peaks coincides with the vibrational frequency of the NH $\cdots$ N stretch (red line).

tion rates. The symmetric potential of mean force are shown in fig 3.14 for several temperatures. The barrier height  $\Delta V_{PMF}$  is found to be directly proportional to the temperature for temperatures above 50 K. For lower temperatures the determination of  $\Delta V_{PMF}$  becomes impossible because the hydrogen stays trapped in one minimum of the double well potentials and at temperatures where only a few reactions are observed this proportionality breaks down.

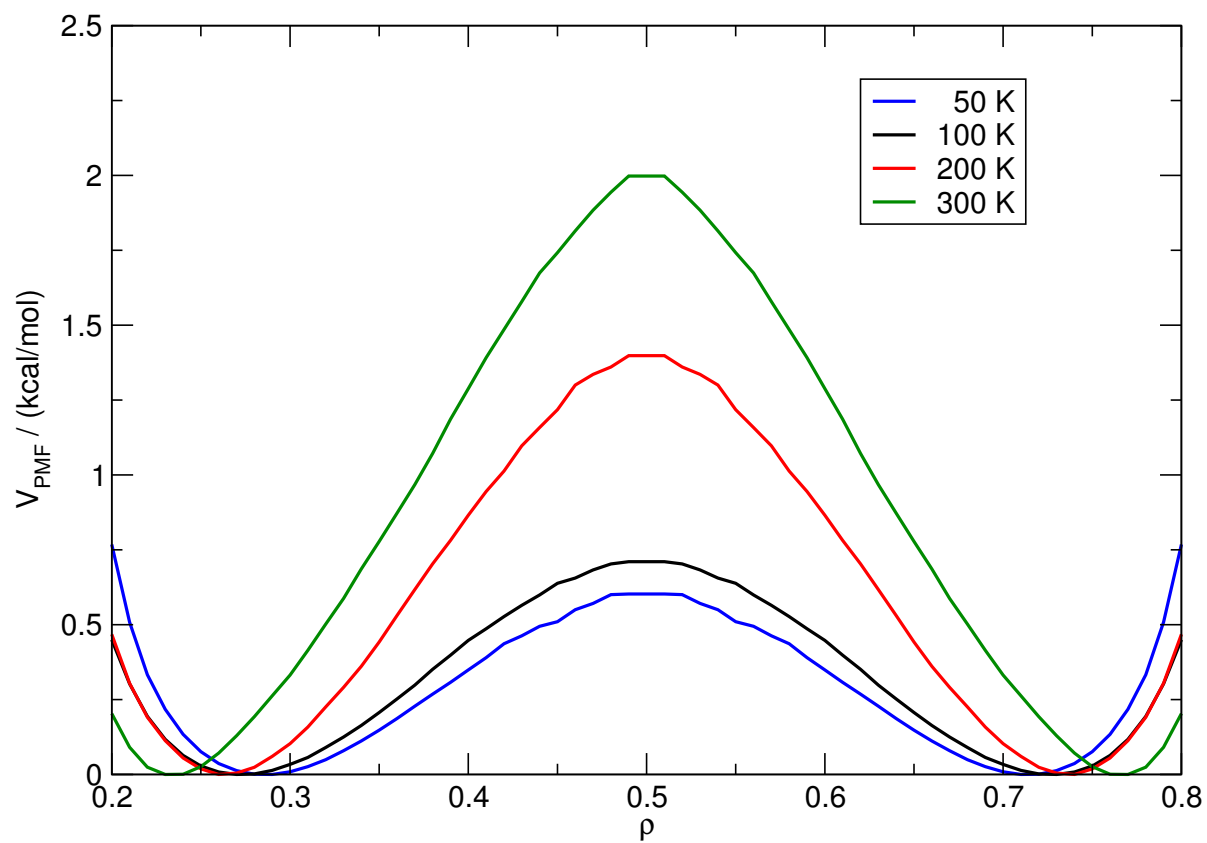


Figure 3.14: Potential of mean force at various temperatures for  $\text{NH}_4^+ \cdots \text{NH}_3$

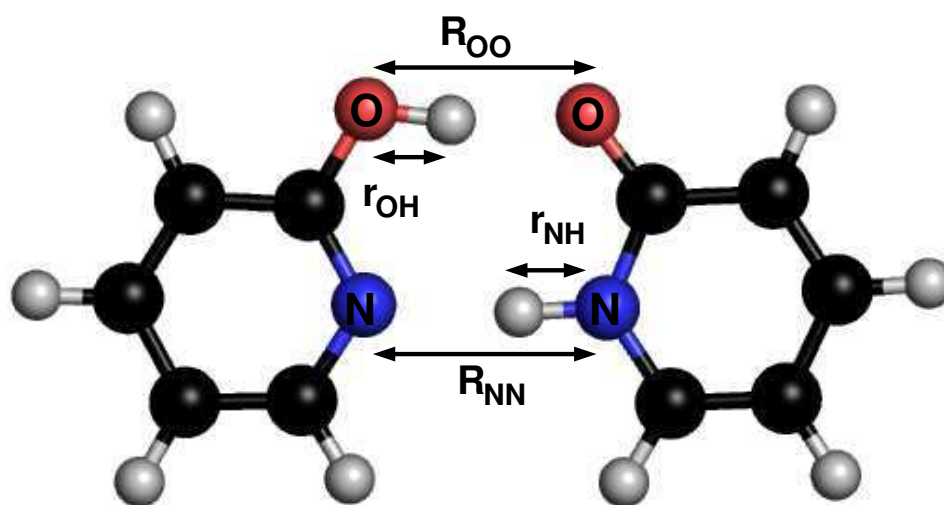


Figure 3.15: Structure of 2-pyridone · 2-hydroxy-pyridine (2PY2HP).

### 3.1.6. Double proton transfer in 2PY2HP

Tautomerism phenomena have drawn the attention of biologists for many decades. For example, the tautomerism of purine and pyrimidine bases occurs naturally in nucleic acids, nucleotides, and enzymes, which may play a key role in mutagenesis. The two stable tautomeric forms of 2-hydroxy pyridine are the enol form (2HP) and the keto form (2PY). The tautomerization as one of the simplest systems of intramolecular and intermolecular proton-transfer reactions has been extensively investigated experimentally (56–59) and also theoretically (60–63). The optimized structure of 2-pyridone · 2-hydroxy-pyridine (2PY2HP) is shown in Fig. 3.15. We describe all atomic motions through the appropriate force field parameters from the CHARMM parameter sets for pyridines. However we define the NHN and OHO hydrogen bonds as new three-body potential term as in our model systems. The inspection of the structure shows that the protons are not shared as in  $[\text{H}_5\text{O}_2]^+$ . One rather needs nearly



symmetrical potentials as in  $\text{NH}_4^+ \cdots \text{NH}_3$  to model the tautomeric character of the proton exchange for the NHN as well as for the OHO hydrogen bridge. Starting point is therefore the parameter set derived for  $\text{NH}_4^+ \cdots \text{NH}_3$ . If we initially use this parameter set to describe the NHN hydrogen bond and OHO we find already satisfying agreement with  $R_{NN}$  compared to the distance found in the *ab initio* geometry. To bring  $R_{OO}$  also in agreement with the *ab initio* results we employ a coordinate scaling  $\lambda_{R_{OO}} = 0.07$ . Additionally the barrier height for the double proton transfer at different levels of theory was found to be between 8.0 kcal/mol (MP2/6-311++G\*\*) and 11.5 kcal/mol calculated with semiempirical density functional (DFT) methods. The potential scaling  $\lambda_E$  can be applied to both the NHN and OHO PES. We developed several  $\lambda_R$  scaled parameter sets, namely for  $\lambda_R = 0.95, 0.97, 0.99, 1, 1.01, 1.03, 1.06,$  and  $1.10$ . Starting from  $\lambda_R = 1$  we investigate the conformations after a geometry optimization as a function of  $\lambda_R$ . In particular we focus our attention on the distance of the donor and acceptor atoms of the two proton bridges. We recorded the distances between the oxygen  $R_{OO}$  and nitrogen atoms  $R_{NN}$  for several combinations of scaling factors  $\lambda_R$ . The results are summarized in Tab 3.1. If we take the results of the B3LYP/6-311++G(d,p) calculation as reference ( $R_{OO} = 2.64 \text{ \AA}$  and  $R_{NN} = 2.87 \text{ \AA}$ ) we observe that the unscaled potential surfaces cannot be simply transferred to describe the geometry of 2PY2HP. We observe a too short  $R_{NN}$  distance and a too long  $R_{OO}$  distance. We stepwise increase the scaling factor  $\lambda_{R_{NHN}}$  until we achieve a  $R_{NN}$  distance in better agreement with the DFT results. In a similar manner we decrease the scaling factor  $\lambda_{R_{OHO}}$ . The PES of the double proton transfer (DPT) is shown for  $\lambda_{R_{OHO}} = 0.95$  and  $\lambda_{R_{NHN}} = 1.10$  in Fig. 3.16f. The distances found for the optimized geometry are  $R_{OO} = 2.660 \text{ \AA}$  and  $R_{NN} = 2.914 \text{ \AA}$ , respectively. The minimum geometry is comparable to the DFT results. The barrier height of about 6 kcal/mol is slightly lower as the DFT barrier height of about 8 kcal/mol. This is of minor concern since an energy scaling parameter can be applied to reproduce the correct barrier height. However the largest divergence is observed for the location of the transition state. We find the transition state at rather  $\rho_1 = 2.7 \text{ \AA}$  than at  $2.5 \text{ \AA}$  as the DFT calculation suggests. The potential surface of  $\text{NH}_4^+ \cdots \text{NH}_3$  is steep for short  $R$ , and therefore the transition state on a the double proton transfer surface is found at a larger  $\rho_1$  values than desired. The simple scaling factor by itself is insufficient to reproduce this important feature of the DPT PES of 2PY2HP. To achieve this we need to find a more sophisticated scaling function which takes the transition state location into account.

Molecular dynamics simulations have been performed on the different PES. For 10

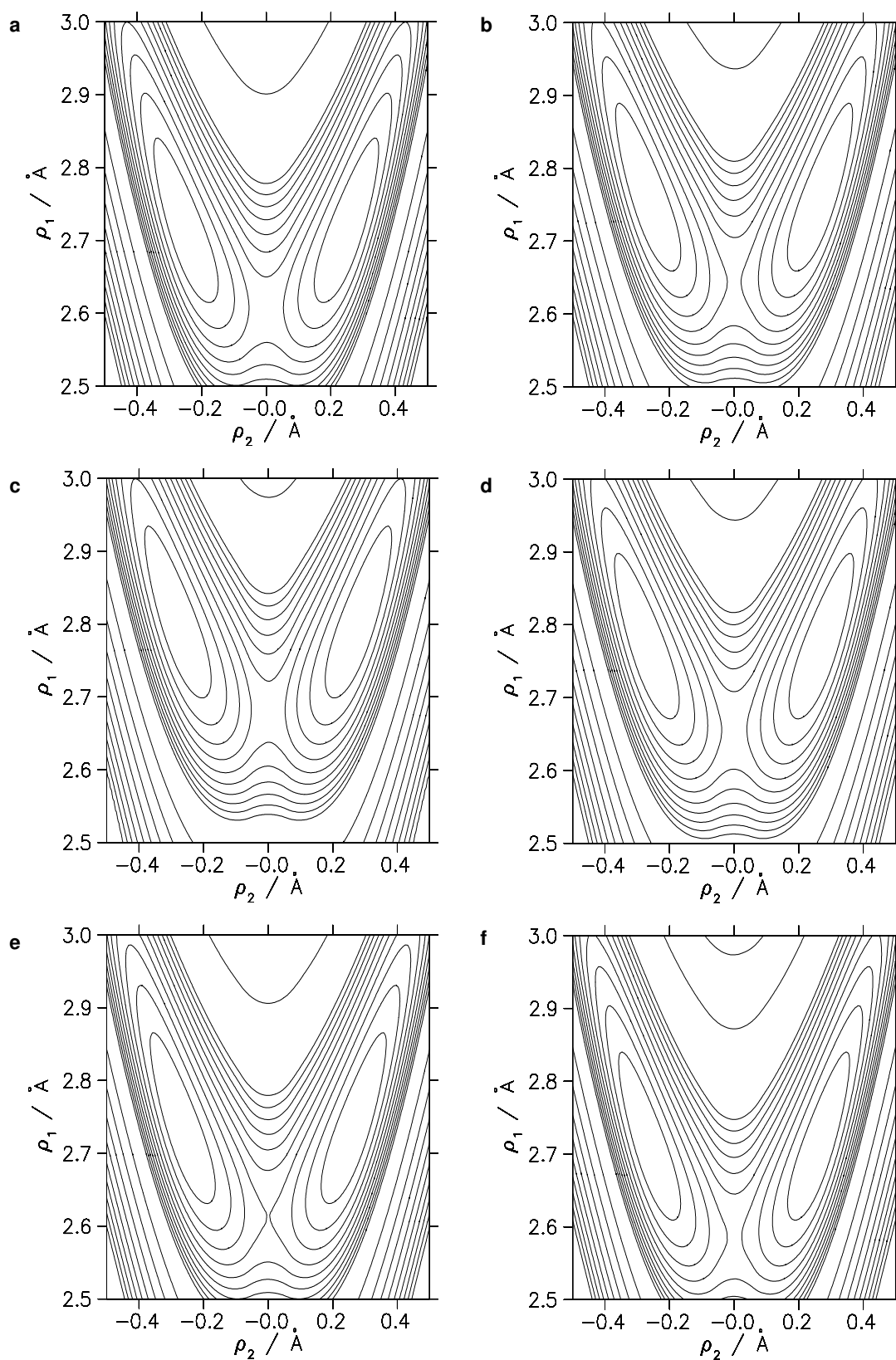


Figure 3.16: Relaxed potential energy surface of the double proton transfer of 2PY2HP. Contour lines are plotted at intervals of 1 kcal/mol below  $E=10$  kcal/mol and at intervals of 10 kcal/mol above. Energies are calculated at grid points after geometry optimization using the MMPT routine and  $\lambda_{R_{OH_2}}$ ,  $\lambda_{R_{NH_2}}$  as scaling parameters as summarized in table 3.1 .

Table 3.1: Pairs of  $\lambda$  scaling parameters and properties of the double proton transfer PES.

	$\lambda_{R_{OHO}}$	$\lambda_{R_{NHN}}$	$R_{OO_{min}} / \text{\AA}$	$R_{NN_{min}} / \text{\AA}$	$\delta / \text{\AA}$	$\Delta E / \text{kcal/mol}$
a	1.00	1.00	2.746	2.683	0.11	4.11
b	1.00	1.03	2.755	2.759	0.12	4.88
c	1.00	1.06	2.763	2.829	0.11	5.46
d	1.00	1.10	2.775	2.923	0.12	6.50
e	0.97	1.10	2.701	2.920	0.15	6.14
f	0.95	1.10	2.660	2.914	0.15	6.08

ps at 300 K the bond distances of the atoms forming the two hydrogen bridges have been recorded. The time series are shown in Fig. 3.17. Inspection of the time series shows that the DPT is a synchronous process rather than a asynchronous. The OH and NH distances are measured with respect to the equilibrium structure and give the distance between the donating and the hydrogen atom. We observe only very short periods where both hydrogen atoms are located on the same side. A cross-correlation analysis of the OH and NH bond distances (fig 3.18) shows that the cross-correlation rapidly drops and already after 0.5 ps a correlation is not detectable. This is noteworthy because the two hydrogen bonds are not explicitly coupled in the MMPT force field.

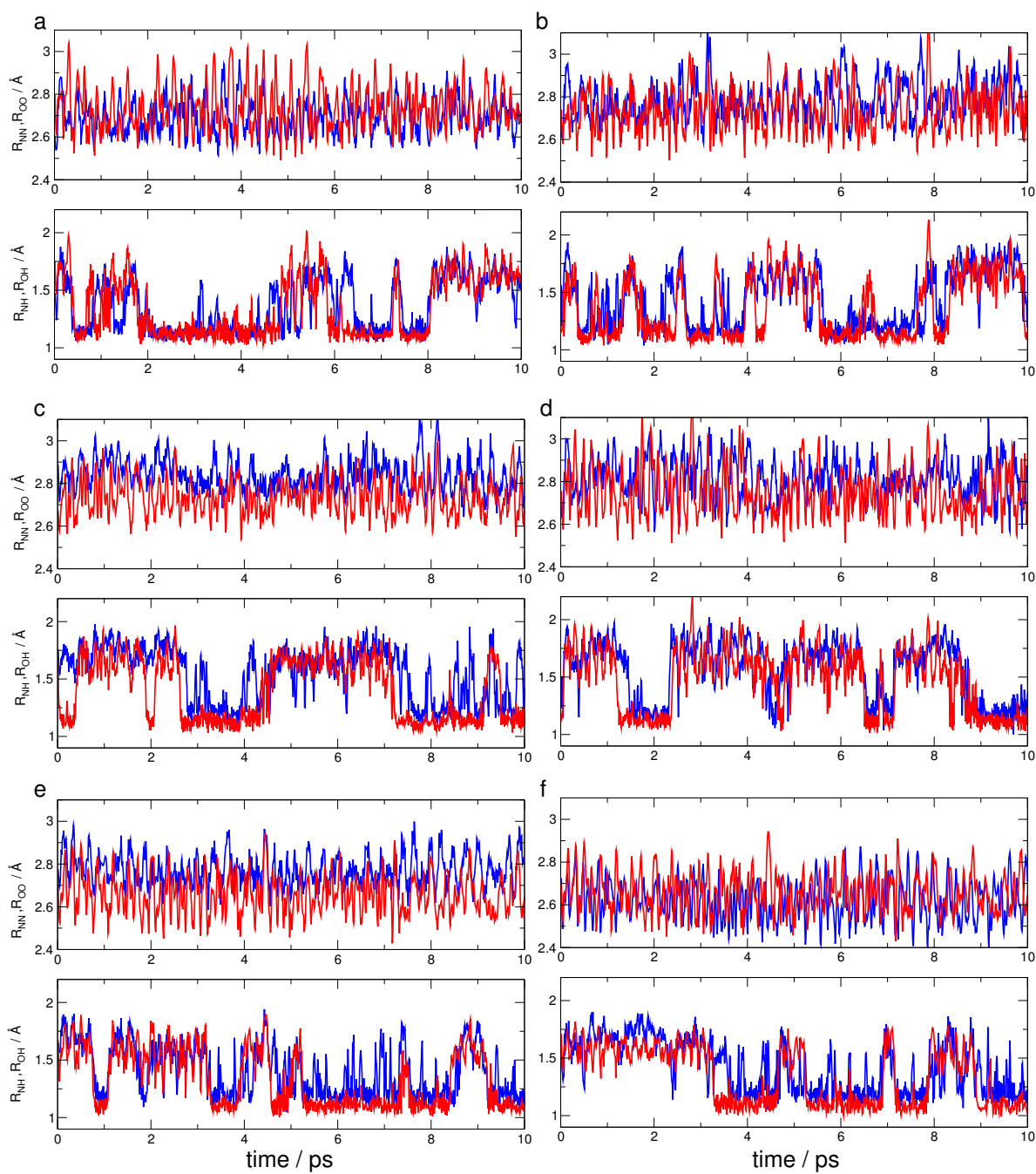


Figure 3.17: Time series of bond distances between the atoms forming the hydrogen bonds in 2PY2HP for different PES. Labels corresponds to table 3.1 and Fig. 3.16.

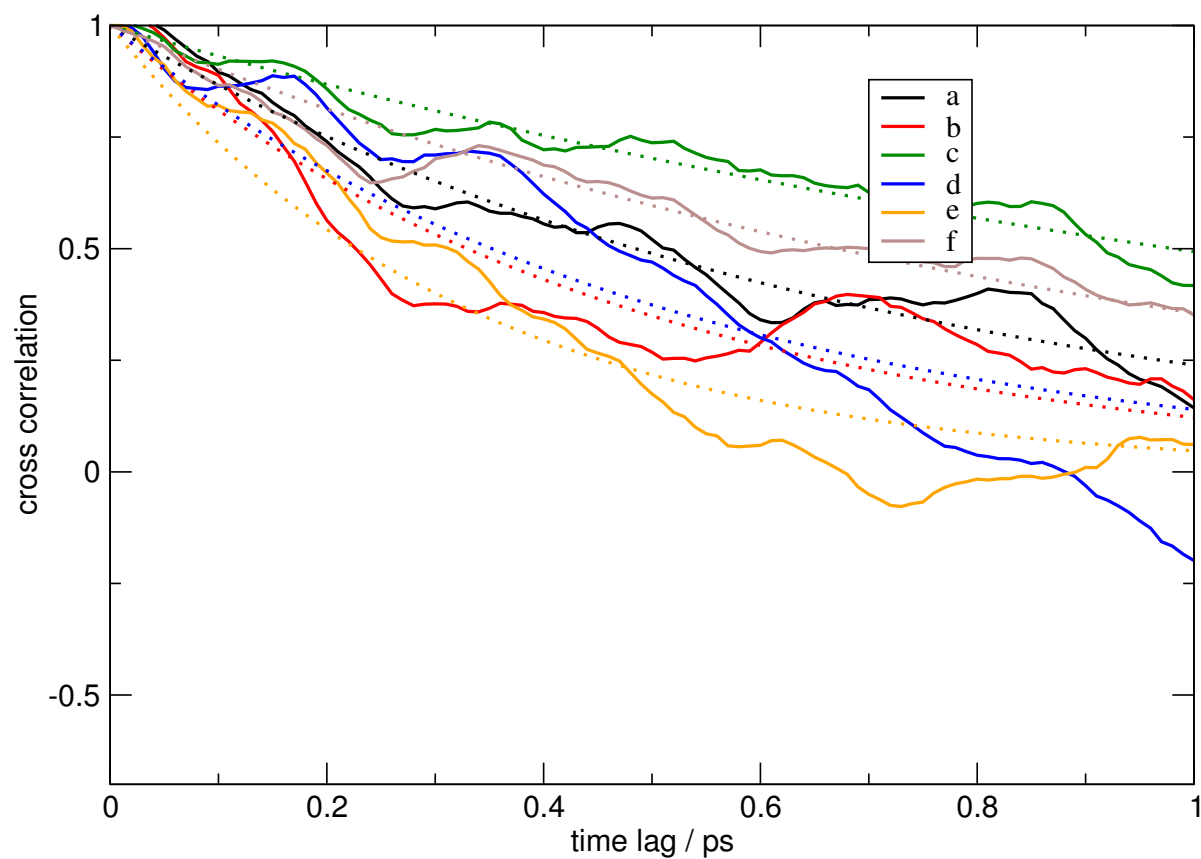
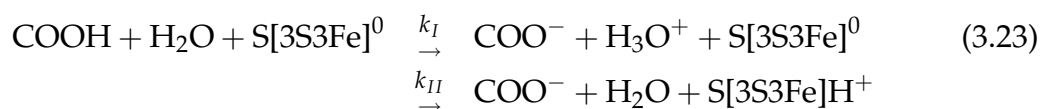


Figure 3.18: Cross-correlation of the OH and NH bond distances. The correlation drops quickly after 0.5 ps suggesting that the DPT transfer is a synchronous process. An exponentially decaying function is fitted to the correlation (dotted lines).

### 3.1.7. Ferredoxin I

Many systems will have similar asymmetric PES like our  $\text{NH}_4^+ \cdots \text{H}_2\text{O}$  prototype system when we probe the reaction coordinate of the proton transfer. As an example we like to investigate an alternative mechanism of the PT between a protonated aspartic acid residue to a buried redox center in ferredoxin I and look at the possible role of solvent water molecules (64, 65) in the active site. Bacterial ferredoxin I of *Azotobacter vinelandii* (AV Fd I) is an iron-sulfur protein that mediates electron transfer in the mitochondrial electron transfer chain across the mitochondrial membrane. The protonation of the iron-sulfur cluster is a necessary step in the proton couple electron transfer function of Fd I. The proposed reaction mechanism (66–69) assumes a direct transfer of the proton from Asp 15 to form the protonated species  $\text{H}^+ - [\text{Fe}_3\text{S}_4]^0$ . It does not involve a solvent water molecule. It is known that many enzymatic reactions utilize solvent water molecules and we find that the active site of Fd I is accessible for water molecules and a water molecule is stabilized through hydrogen bonding long enough to act as a possible proton relay. Reconsidering an alternative reaction scheme



we employ the MMPT approach to describe the deprotonation step between the protonated Asp 15 residue and a water molecule in the active site, as a possible first step towards the protonation of the iron-sulfur cluster. The PES of this intermolecular proton transfer is not easily accessible with high level DFT calculations and simulations of fully solvated ferredoxin I is a far too large system to be studied using *ab initio* MD simulations. It is possible to derive model systems but the complete system cannot be investigated with sufficient accuracy. A smaller model system of acetic acid and water  $\text{CH}_3\text{COOH} \cdots \text{H}_2\text{O}$  will therefore serve as an initial description.

#### Morphing PES

Although the minima are found at roughly the same separation of donor and acceptor atom, the cuts through the energetic minima (Fig. 3.20) show substantial differences in the shape of the energetic wells. Through coordinate scaling parameters we are able to morph our initial PES of  $\text{NH}_4^+ \cdots \text{H}_2\text{O}$  into one that reproduces the one of acetic acid and water. The scaling parameters are used to derive new parameters from

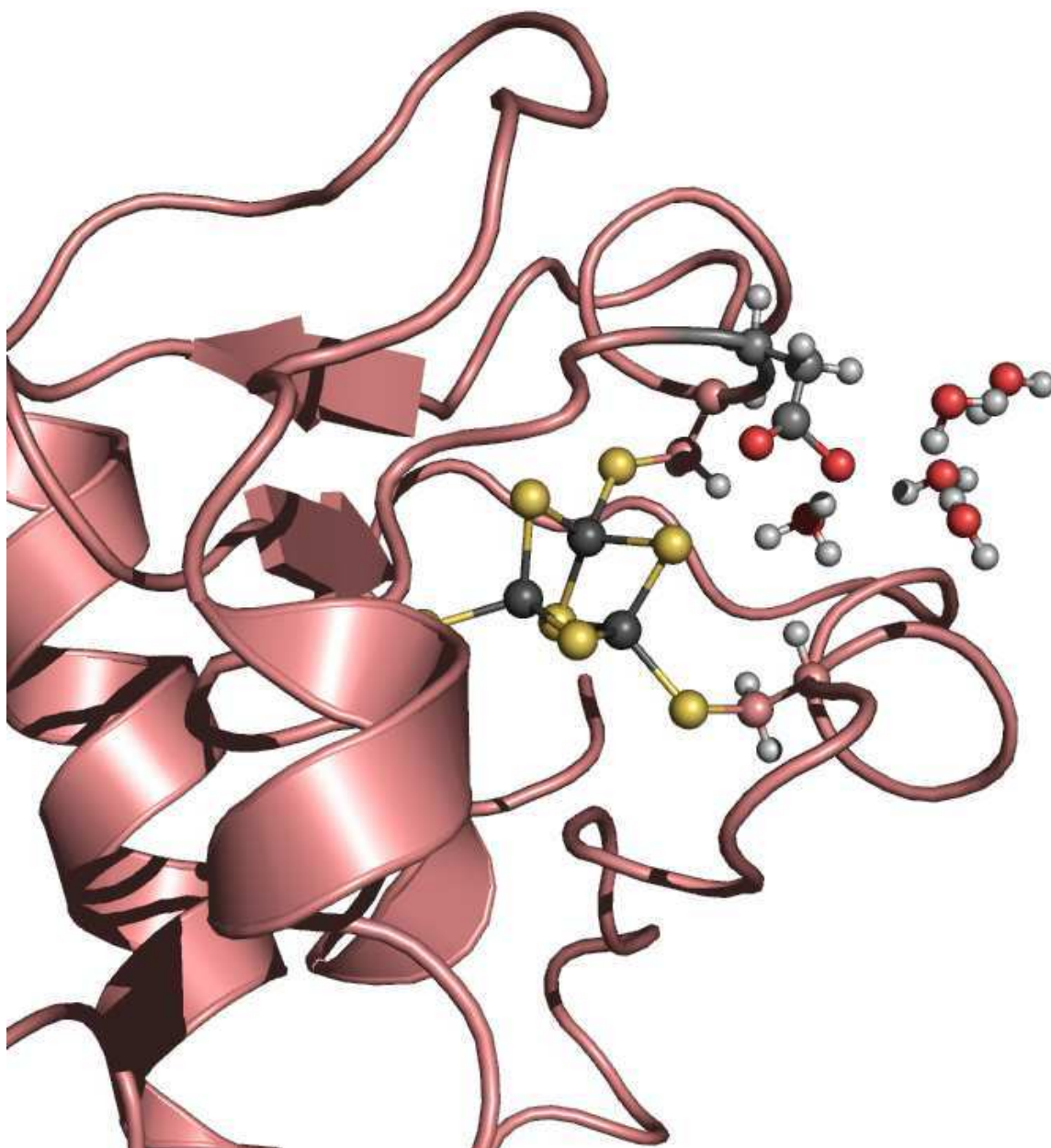


Figure 3.19: Snap shot of the active site ferredoxin I. The protein environment is shown as a schematic drawing. Residue Asp15, three cysteine residues that bind the iron-sulfur  $\text{Fe}_3\text{S}_4$  cluster, a protonated water molecule  $\text{H}_3\text{O}^+$  and further solvent water molecules close to the active site are shown in detail.

the initial parameters without a complete reparametrization. The minimum on the relaxed  $\text{C}_2\text{H}_4\text{O}_2 \cdots \text{H}_2\text{O}$  PES is located at  $R=2.71 \text{ \AA}$  and  $\rho=0.17$  compared to  $R_a=2.78 \text{ \AA}$  and  $\rho=0.23$  on the  $\text{NH}_4^+ \cdots \text{H}_2\text{O}$  PES. The first step in the morphing transformation is therefore to match the locations of the minimum on the  $\text{NH}_4^+ \cdots \text{H}_2\text{O}$  PES with the minimum on  $\text{C}_2\text{H}_4\text{O}_2 \cdots \text{H}_2\text{O}$  PES. We achieve this transformation through the coordinate scaling using the ratio

$$\lambda_R = R_a/R_b.v5.7.2.tgz \quad (3.24)$$

Multiplying  $\lambda_R = 1.025$  with the initial  $R_a$  coordinates leads to a stretching of the PES. The location along the  $R$  coordinate of the morphed PES coincides then with the  $R$  value of the target PES. The scaling causes the whole PES to stretch. To shift the location of the minimum along the  $\rho$  coordinate we choose a different approach that focuses on the well region for short hydrogen bonds. As we can conclude from 2D cuts of the PES through the minima the other important coordinate to morph is the reaction coordinate of the proton transfer. A possible scaling function as an adjustable model parameter is

$$\lambda_\rho(\rho) = (1 - \rho_{min}(1 - 1/(1 + \exp(-k_{s_\rho}(\rho - 0.5))))))\rho. \quad (3.25)$$

The adjustable parameters are the location of the minimum along the reaction coordinate  $\rho_{min}$ . The energetic well is deep and the chosen functional form of the morphing will match the location of the minima and leave the high energy areas mainly unchanged. The parameter  $k$  controls how fast the transition from morphed to unmorphed region proceeds. The next morphing step focuses on the high energy region for large hydrogen bond distances. The difference in energy between the two cuts can be described by a third order polynomial in combination with a sigmoidal function that accounts for long hydrogen bonds and neglects the short bond region. The energy difference can be calculated by

$$V_{\lambda_E} = (1/(1 + \exp(-k_{s_V}(\rho - \rho_s)))) \cdot (a_1 + a_2x + a_3x^2 + a_4x^3) \quad (3.26)$$

and the morphed energies are then expressed as

$$V_{morph}(R', \rho', \theta') = V_{orig}(\lambda_\rho(\rho), \lambda_R R, \theta) + V_{\lambda_E}. \quad (3.27)$$



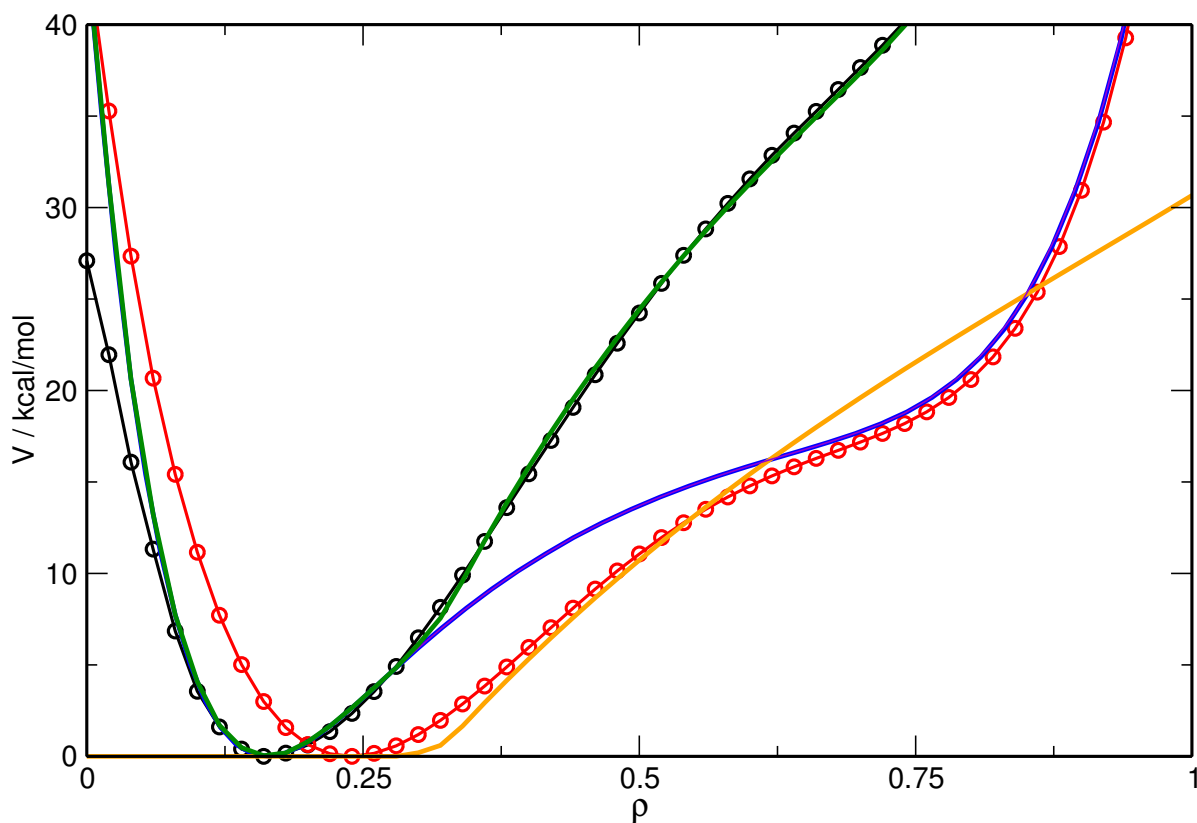


Figure 3.20: Cuts through the energetic wells of the PES of protonated acetic acid (black curve) and water and  $\text{NH}_4^+$  and bound water molecule (red curve). The effect of the coordinate scaling along  $\rho$  of Eq. 3.25 is demonstrated by the blue curve. The energy correction provided by  $V_{\lambda_E}$  is shown in orange. The circles mark the grid points of the PES scan. The result of the all morphing steps combined  $V_{morph}$  is shown in green.

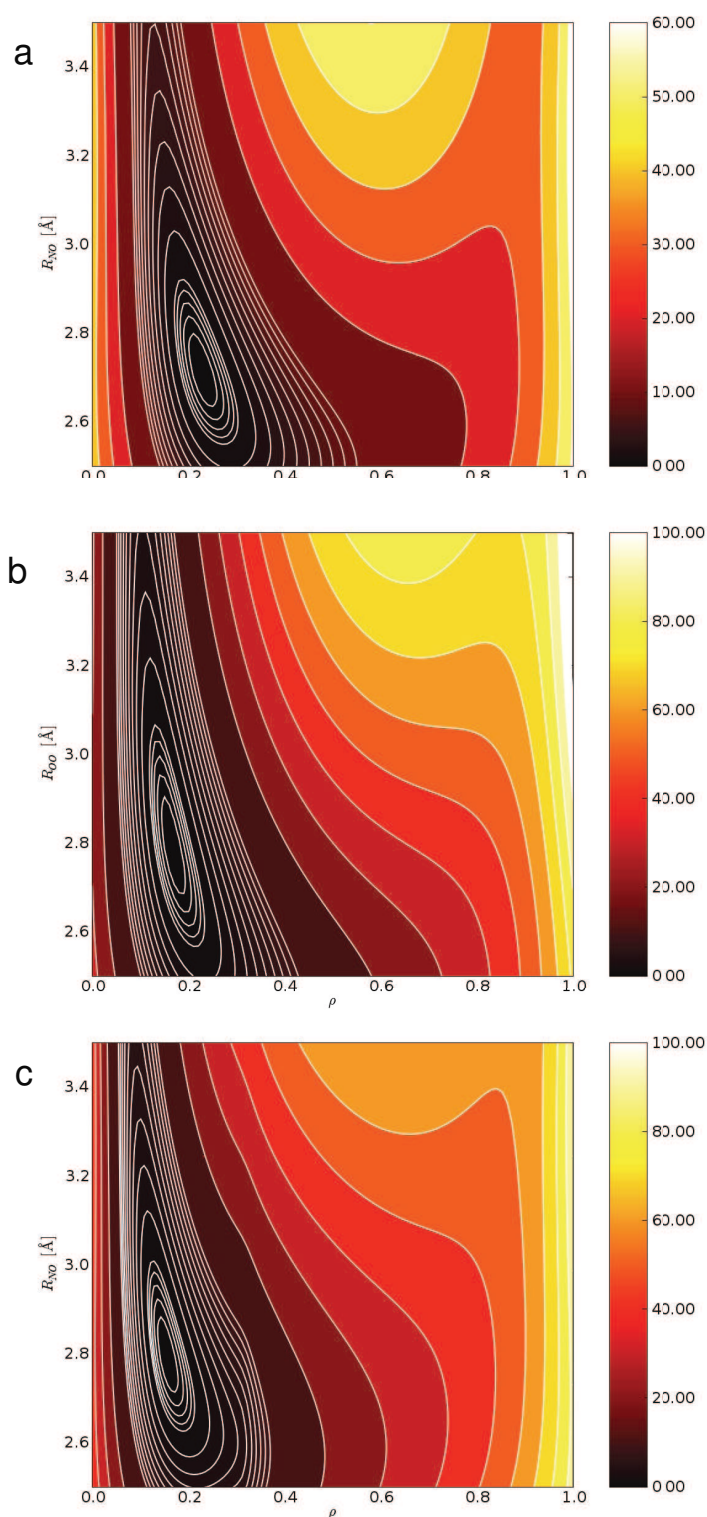


Figure 3.21: Comparison of the PES of (a) the protonated ammonia-water dimer  $\text{NH}_4^+ \cdots \text{H}_2\text{O}$ , (b) the model system acetic acid and water  $\text{CH}_3\text{COOH} \cdots \text{H}_2\text{O}$ , and (c) the morphed PES to model the PT in the active site in Fd I.

### Free energy profile and rate constant

Using the morphed PES we are able to study the dynamics of the proton of a protonated water molecule in the vicinity of the aspartic acid residue Asp 15 with our MMPT description. Since the proton transfer reaction involves an energy barrier that is significantly larger than the thermal energy, an umbrella potential and reactive MD simulations were combined to map the free energy profile along the PT coordinate. For this purpose we define the progression coordinate as the ratio  $r_{OH}/R_{OO}$ , where  $r_{OH}$  is the bond length between proton and the donating oxygen atom of Asp 15 and  $R_{OO}$  is the distance between the oxygen atoms of a proton accepting water molecule and Asp 15. We performed a 10 ps MD simulation with an additional adaptive umbrella potential (70) at temperature  $T=300\text{K}$ . The resulting free energy profile is shown in Fig. 3.22. We can estimate the free energy barrier  $\Delta G$  of 8.2 kcal/mol for the reaction if we assume the activation barrier between the minimum and the point where the profile starts to form a plateau. We can then calculate an estimate for the transition state theory (TST) rate constant using (71)

$$k_{TST}(T) = \frac{k_B T}{h} e^{-\Delta G^{act}(T)/RT} \quad (3.28)$$

where  $k_B$  is Boltzmann's constant,  $h$  is Planck's constant, and  $R$  is the gas constant. This gives a calculated value for  $k(300\text{K})$  of  $1.7 \times 10^5 \text{ s}^{-1}$  for the transfer of the proton. Reconsidering the reaction scheme (see Eq. 3.24) it becomes clear that the calculated rate constant  $k_{TST}$  compares with  $k_I$  whereas the experimentally measured would be the combination of the two steps  $k_I + k_{II}$ . It therefore appears plausible that the deprotonation rate constant occurs to be two magnitudes faster.

### 3.1.8. Conclusion

This section introduced the MMPT method to study proton transfer reactions. To characterize the reaction dynamics we developed functional expressions suitable to accurately reproduce the PES of our prototype systems. We implemented these into the standard CHARMM MD program to describe classically the bond formation and breaking of the proton transfer. We presented dynamical simulations of proton transfer reactions in the prototype system of  $\text{NH}_4^+ \cdots \text{NH}_3$ . The very fast MD simulations allow us to calculate the temperature dependence of the free energy profiles directly

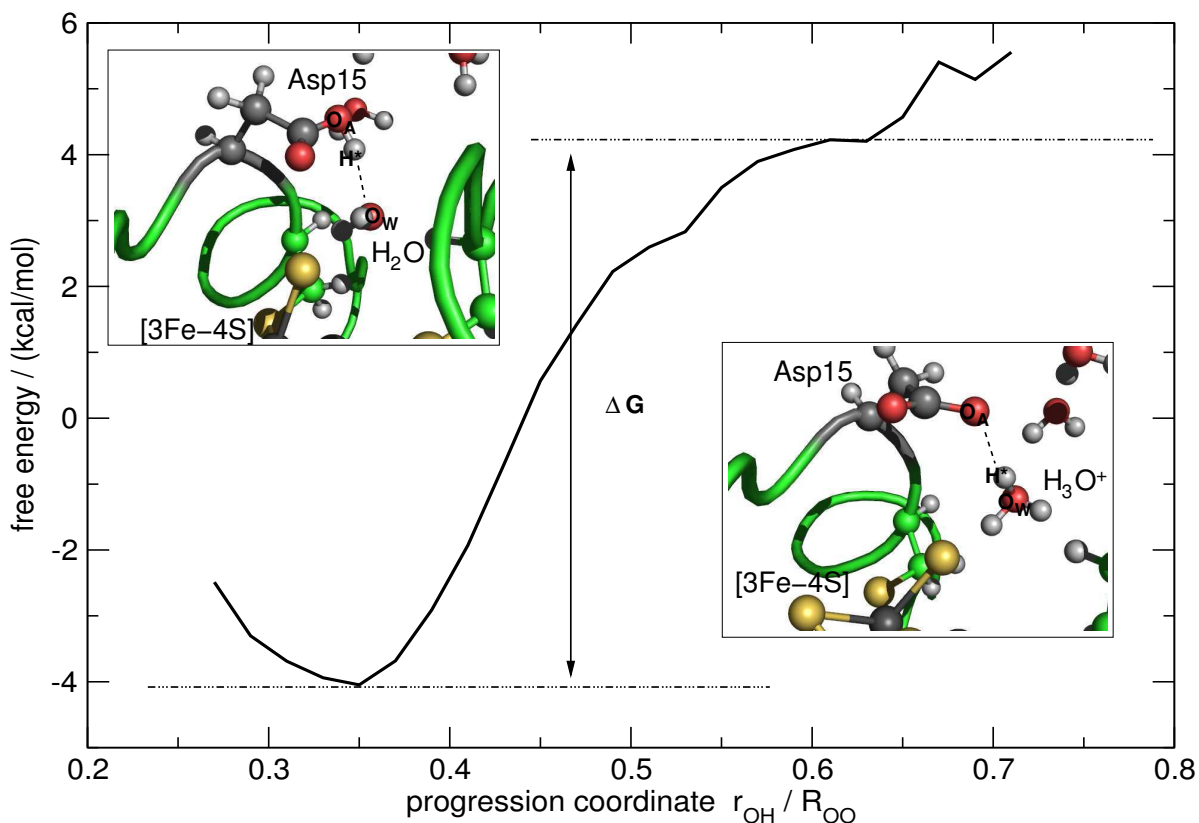


Figure 3.22: Free energy profile of proton transfer between Asp 15 and a water molecule in the active site of Fd I (red curve) calculated from MD simulation using umbrella sampling and the corresponding potential energy calculated for average values of  $r_{OH}$  and  $R_{OO}$  for a given value of the progression coordinate  $\delta$ . Taken from from the umbrella sampling trajectory are two exemplary conformations, picturing the reactant state  $COOH + H_2O + S[3S3Fe]^0$  with  $R_{OO} = 2.79 \text{ \AA}$  and  $r_{OH} = 0.94 \text{ \AA}$  (left inset) which corresponds to a reaction coordinate value of 0.34 and the product state  $COO^- + H_3O^+ + S[3S3Fe]^0$  (right inset) with  $R_{OO} = 3.03 \text{ \AA}$  and  $r_{OH} = 2.04 \text{ \AA}$  which leads to a reaction coordinate value of 0.67.

by a statistical analysis of the trajectories. Also we were able to derive a value of the temperature-dependent 'reaction rate' for the proton oscillation. We found 10 crossings/ps is the maximum number of observed crossings for high temperatures and that this limit originates from the nitrogen–nitrogen stretch frequencies. An important part of this section has been reserved to illustrate the morphing approach. We presented the effect of barrier scaling through  $\lambda_E$  for  $\text{NH}_4^+ \cdots \text{NH}_3$ . Also we show how several scaling factors  $\lambda_R$  can be combined to model the double proton transfer PES of 2PY2HP. More complex scaling functions were developed to model the proton transfer reaction between an acetic acid and water. The parameters of this model system were then used to calculate the free energy profile of a proton abstraction from an aspartic acid residue by a solvent water molecule within the active site of Ferredoxin I to investigate an alternative reaction mechanism.

## 3.2. Investigating the Relationship between Infrared Spectra of Shared Protons in Different Chemical Environments: A Comparison of protonated diglyme and protonated water dimer

### 3.2.1. Introduction

The transfer of protons in chemically (acid-base chemistry, proton conducting wires) and biologically (enzymatic reactions) relevant systems is of fundamental importance for a variety of processes. Early models go back to Grotthus in the 1800s which view proton transfer (PT) in liquid as a shuttling process between reorienting molecules (72). Despite the tremendous progress in experimental techniques it was for a long time only possible to infer proton transfer in the ground state and in the gas phase *indirectly*, since it is a transient process. This is in contrast to experiments in the condensed-phase where it is possible to investigate hydrogen bonds using infrared spectroscopy because of the larger number-densities (73). For electronically excited state, PT is a much better characterized process, in particular since double resonance and molecular beam techniques were developed and matured (74–76). With the advent of tunable, high-luminosity light sources in the mid-infrared (free electron lasers or optical parametric oscillators), the use of direct absorption spectroscopy to characterize strongly bound protonated systems in the gas phase has become possible. The first observation of the protonated water dimer in the region between  $600\text{ cm}^{-1}$  to  $1900\text{ cm}^{-1}$  is an example for this recent success (1). Additional experiments on the same and related systems have provided further information about the vibrational spectroscopy of the shared proton (77, 78). Alternatively, vibrational predissociation spectroscopy of mass-selected, rare gas-solvated  $\text{H}_5\text{O}_2^+(\text{Ar})_n$  and  $\text{H}_5\text{O}_2^+(\text{Ne})_n$  has been used to characterize the molecular vibrations of  $\text{H}_5\text{O}_2^+$  as a function of the degree of solvation  $n$  (79). This study has provided some evidence that the asymmetric OH\*O stretching frequency is around  $1000\text{ cm}^{-1}$ . However, because complexation with a Ne atom lowers the symmetry of the system, it is possible that some bands split. This is observed in the experiment but could not be reproduced by several computational techniques and the authors were not prepared to make a firm assignment, in particular, of the identity and origin of the lower frequency component of the doublet (79).

Recently, it has been suggested that from the assignment of vibrational bands in  $\text{H}_5\text{O}_2^+$ , the vibrational spectrum of a proton shared between two oxygen atoms for a series of  $\text{AO}\cdots\text{H}^+\cdots\text{OA}$  motifs (where A forms the chemical environment for the bridging proton transfer motif;  $\text{A}=\text{H}_2$  for  $\text{H}_5\text{O}_2^+$ ) can be inferred. In particular, the asymmetric stretch vibration in protonated diglyme ( $[\text{diglyme-H}]^+$ ) has been assigned by visually comparing the spectrum with that of  $\text{H}_5\text{O}_2^+$  (78). A possible justification for the hypothesis that the vibrational spectra of the shared proton in  $\text{H}_5\text{O}_2^+$  and in  $[\text{diglyme-H}]^+$  are related, is that the potential energy surfaces that govern proton transfer between two oxygen atoms in  $\text{H}_5\text{O}_2^+$  and  $[\text{diglyme-H}]^+$  are topologically related. In the present work we test this hypothesis by using state-of-the art interaction potentials designed to describe proton transfer.

Over the past few years, computational and theoretical investigations of proton transfer in isolated or solvated systems have attracted considerable interest (80–93). Some of these studies used empirical potentials, (81–83, 86, 88) whereas others treated the electronic energy with Car-Parrinello or related approaches (87, 89, 90, 94, 95). Examples include the proton transfer dynamics along a chain of water molecules (86, 89, 94, 96) or a mixed water-ammonia chain (87). Other work was concerned primarily with the proper treatment of the nuclear dynamics using path integral (82, 83, 86, 88) or basis set methods (84). For  $\text{H}_5\text{O}_2^+$  in particular computational studies have investigated the structure, harmonic and anharmonic vibrations at various levels of sophistication (84, 91, 93, 97–99). They range from classical molecular dynamics (MD) simulations (84, 93, 99) to fully-dimensional diffusion Monte Carlo (DMC) calculations (98). Molecular dynamics simulations play a central role for the investigation of such systems because simulations at finite temperature are able to sample and characterize the properties of the system at configurations that are far from the equilibrium structure. In the present work this is important because we are interested in the dynamics of the proton transfer and the spectroscopic information derived from it. Furthermore, previous computational work showed that the vibrational spectrum of  $\text{H}_5\text{O}_2^+$  is temperature-dependent (93, 100) and the experiments are carried out at high laser power which provides considerable amounts of internal energy to the species considered (1, 77, 78). Contrary to high-resolution spectroscopic experiments in cold, supersonic expansions for which many successful bound state calculations exist (32, 101), the assignment of vibrational spectra for molecular species recorded at extreme (high laser power) conditions is likely to require alternative methods than those previously employed for high-resolution spectroscopic experiments (101).

One of the difficulties in using molecular dynamics (MD) simulations to investigate the energetics, dynamics and spectroscopy involving reactive processes is that the potential energy functions are not suited to describe bond formation and bond breaking. For sufficiently small systems (several atoms) it is possible to calculate and fit a fully dimensional potential energy surface and to use it in MD simulations. For larger systems, such as protonated diglyme or proton transfer in a protein environment, this approach is not feasible because of the high dimensionality to describe the PES. On the other hand the energy expression of a conventional force field, which is usually fitted to structural and spectroscopic data, is not suitable for investigating bond breaking and bond forming processes (9, 10). Possible extensions to describe reactive phenomena include mixed quantum mechanics/molecular mechanics calculations (QM/MM) (14, 15, 102). They decompose the system into a part that is directly involved in the reaction and treat it by quantum mechanics, while the rest of the system is treated by a molecular mechanics force field. Examples for the QM part are explicit *ab initio* techniques (103) or density functional theory, semiempirical treatments (e.g. AM1/PM3), empirical valence bond theory (EVB) (18) or approximate valence bond theory (AVB) (104). However, even in the QM/MM framework high level QM approaches are difficult to use for sufficiently long simulation times (several picoseconds up to nanoseconds) due to the large amount of computer time required for dynamical studies.

In the present work an approach inspired by mixed QM/MM calculations is used which combines a potential energy surface (PES), the QM part, suitable for describing the proton transfer between an acceptor and a donor atom with a force field, the MM part, for the remaining degrees of freedom. The three-dimensional PES is calculated at the MP2 level for  $\text{H}_5\text{O}_2^+$  as a model system for proton transfer and then transformed to describe PT in protonated diglyme. Previous work has studied topological similarities of PESs calculated at different levels of *ab initio* theory (32, 105, 106) while in the present case the chemical environment motivates a relationship between the PESs (“morphing”) via a transformation. In its original formulation, morphing was used to systematically modify an *ab initio* potential to fit experimental data. The procedure retains the general shape of the *ab initio* potential, but allows, e.g., barrier heights and the absolute and relative depths and distances of potential minima to change. The first application showed that it is possible to transform an approximate PES (calculated at a lower level of *ab initio* theory) into a high quality PES that is capable of reproducing all experimental observables for Ne–HF to within spectro-



scopic accuracy (32). Here, the morphing approach is used to transform a generic, high-quality, multidimensional PES for proton transfer in  $\text{H}_5\text{O}_2^+$  to a PES that captures the energetics of proton transfer in protonated diglyme. The two PESs are then used in finite-temperature MD simulations which allows us to exhaustively sample the multidimensional PES.

The work is organized as follows: in the next section the computational methods used are presented. Next, the dynamics and the infrared spectra for both, protonated diglyme and  $\text{H}_5\text{O}_2^+$  are analyzed and compared. Finally, the results are discussed and conclusions are presented.

### 3.2.2. Computational Methods

#### Intermolecular Interactions

In the following, the  $\text{O} \cdots \text{O}$  (donor-acceptor) distance is  $R$  and the  $\text{O}-\text{H}^*$  distance (separation of transferring hydrogen to the donor atom) is  $r$ . The angle  $\theta$  is defined as the scalar product between the unit vectors  $\hat{R}$  and  $\hat{r}$  (see Figure 3.23). *Ab initio* calculations were carried out at the MP2/6-311++G(d,p) (for  $\text{H}_5\text{O}_2^+$ ) and B3LYP/6-311++G(d,p) (for protonated diglyme) using Gaussian03 (40). For scanning the fully relaxed potential energy surfaces (PESs) in the collinear  $\theta = 0$  conformation of the PT motif, the  $(R, r)$  grid was defined by  $R \in [2.2, 3.2]$  Å in increments of 0.1 Å and  $r$  between 0.8 Å and the midpoint between the two oxygen atoms in increments of 0.05 Å. For each geometry  $(R, r)$  all other coordinates were optimized which finally leads to a relaxed PES. To describe the bending degrees of freedom in  $\text{H}_5\text{O}_2^+$  further calculations were carried out at angles  $\theta = 11.98^\circ, 27.49^\circ, 43.10^\circ$ , and  $58.73^\circ$  on the same  $(R, r)$ -grid as for  $\theta = 0$ . This gives a total of 1265 points. The  $\theta$ -grid was chosen for an efficient and stable representation of the angular dependence by Legendre polynomials and to describe internal rotation of the  $\text{H}_3\text{O}^+$  molecule. However, for the present applications the angular dependence is sufficiently well described by a harmonic potential (as in a conventional force field) in  $\theta$ , since reorientation phenomena are not of interest. To enhance the robustness of the fit in its short and long range  $R$ -region, very short (1.8 and 2.0 Å) and very long (4.0, 6.0, and 8.0 Å) O–O distances  $R$  were included in the fit for selected angular cuts. The data were fit using I-NoLLS, a program for interactive non-linear least squares fitting of the calculated energies to a functional form of the potential energy surface (107).

For the MD simulations, the three-dimensional PES  $V(R, r, \theta)$  was implemented

into the CHARMM program. A fuller account of the implementation can be found in Ref. (108). The total electronic energy of the system (with coordinates  $\vec{x}$ ) is decomposed into a part for the proton transfer motif ( $V_{\text{PT}}(R, r, \theta)$ ) and the remaining degrees of freedom  $\vec{y}$  of the system. Thus, the total interaction is written as

$$V(\vec{x}) = V_{\text{PT}}(R, r, \theta) + V_{\text{MM}}(\vec{y}) \quad (3.29)$$

The resulting potential, Eq. 3.29, is called molecular mechanics with proton transfer (MMPT).

In a conventional MD simulation the bonds are defined at the beginning of a calculation and can not be broken or formed subsequently. The present setup follows this standard procedure in that the hydrogen/proton ( $\text{H}^*$ , see Figure 3.23) of interest is initially bonded to the donor D. However, during the simulation the functional form of  $V_{\text{PT}}(R, r, \theta)$  (see below) is suited to describe the atom  $\text{H}^*$  leaving D and binding to the acceptor atom A. Both, D and A are usually bonded to other atoms, X, of the molecular framework. This involves angular (bonded) terms such as  $\text{XDH}^*$ . Whenever  $\text{H}^*$  attempts to transfer from D to A, such bonded terms are damped from the total energy and corresponding new terms (e.g.  $\text{YAH}^*$ ) are introduced in a smooth fashion. A switch function  $f_{\text{sw}}(R, r)$  is used to turn the necessary terms on or off. For this, a sigmoid function  $f_{\text{sw}}(R, r) = \frac{1}{2}(\tanh(a \cdot R(r - \frac{R}{2})) + 1)$  is chosen. With  $a = 2 \text{ \AA}^{-2}$ ,  $f_{\text{sw}}$  yields 0.5 at the transition state and values close to one if  $\text{H}^*$  is bound to D and zero if  $\text{H}^*$  is bound to A. Non-bonded terms are treated in an analogous manner. The above scheme is valid for symmetric systems (identical terms are removed and introduced on the D and A side, respectively).

For rapid evaluation of the energies and gradients, the functional form of  $V(R, r, \theta)$  is chosen with some care. To stabilize the fitting it was found advantageous to express the potential energy surface as  $V_{\text{PT}}(R, \rho, \theta)$  with  $\rho = (r - r_{\text{min}})/(R - 2r_{\text{min}})$  and  $r_{\text{min}} = 0.8 \text{ \AA}$ . Thus, the coordinates of  $V_{\text{PT}}(R, \rho, \theta)$  are  $R$  (D–A separation),  $\rho$  (position of  $\text{H}^*$  relative to D for a particular  $R$ ) and the angle  $\theta$ . Overall,  $V_{\text{PT}}(R, \rho, \theta)$  is given by:

$$\begin{aligned} V_{\text{PT}}(R, \rho, \theta) &= D_{\text{eq}}(R)[1 - \exp(-\beta(R)(\rho - R_{\text{eq}}(R)))]^2 \\ &+ D_{\text{eq}}(R)[1 - \exp(-\beta(R)(1 - \rho - R_{\text{eq}}(R)))]^2 \\ &- D_{\text{eq}}(R) + c + k\theta^2 \end{aligned} \quad (3.30)$$

where the parameters  $D_{eq}$ ,  $\beta$ , and  $R_{eq}$  are functions of  $R$ , and  $c$  and  $k$  are constants :

$$v5.7.2.tgz D_{eq}(R) = p_1(1 - \exp(-p_2R - p_3))^2 + p_4 \quad (3.31)$$

$$\beta(R) = p_5 + p_6R \quad (3.32)$$

$$R_{eq}(R) = p_7 \exp(-p_8R) + p_9 \quad (3.33)$$

$$k = p_{10} \quad (3.34)$$

$$c = p_{11} \quad (3.35)$$

The fit parameters  $p_i$  can be found in Tab. 3.2.

For protonated diglyme, the proton transfer motif is described with the same functional form of  $V(R, \rho, \theta)$ . However, its shape is modified through a transformation ( $V(R, \rho, \theta) \rightarrow \tilde{V}(R, \rho, \theta)$ ) to capture the essential features of the relaxed PES from the B3LYP/6-311++G(d,p) calculations. For this, two morphing parameters were introduced, namely an energy scaling  $\lambda_1$  ( $V \rightarrow \lambda_1 V$ ), and a distance scaling  $\lambda_2$  ( $R \rightarrow \lambda_2 R$ ). The two parameters  $\lambda_1$  and  $\lambda_2$  are determined such as to reproduce the location of the minimum energy structure  $R_{\min}$  calculated with B3LYP/6-311++G(d,p) and to better represent the flatter surface of protonated diglyme compared to  $\text{H}_5\text{O}_2^+$  for large separations  $R$ . As mentioned above, the 2d-reference potential for protonated diglyme was calculated for the collinear proton transfer only because a fully relaxed 3-dimensional PES for protonated diglyme would be computationally very demanding.

### Molecular Dynamics Simulations and Analysis

All molecular dynamics simulations were carried out with CHARMM (9) and the CHARMM22 force field (13). The time step used was 0.25 fs, sufficiently small to follow the rapid hydrogen motions and to ensure energy conservation. The systems ( $\text{H}_5\text{O}_2^+$  and protonated diglyme) were heated and equilibrated at the target temperatures (5 K, 10 K, 25 K, 50 K, and 100 K) for 5 ps. All production MD simulations were 125 ps in length and all atoms were free to move.

MD simulations were started from the optimized *ab initio* structures. The atom types and force constants are taken from the CHARMM22 force field and are summarized in Table 3.3 together with the force field parameters in Table 3.4. The parametrization of water corresponds to the TIP3P force field with a modified OH force constant ( $k_{\text{OH}} = 550 \text{ kcal/mol/\AA}^2$ ) to reproduce the frequency of the symmetric O-H stretch-

ing vibration.

MD simulations provide coordinates and the total dipole moment of the system as a function of time  $t$ . Infrared spectra are calculated from the Fourier transform of the dipole-dipole autocorrelation function. To this end, the total dipole moment  $M(t)$  recorded along the trajectory, was correlated over  $2^{15}$  time origins to give  $C(t)$ . Using a Blackman filter (109) to suppress noise and a fast Fourier transform, the spectral signal  $C(\omega)$  is obtained. To arrive at the infrared spectrum  $A(\omega)$  the function  $C(\omega)$  is weighted with the correct Boltzmann weight (110, 111)

$$A(\omega) = \omega \{1 - \exp[-\omega/(kT)]\} C(\omega), \quad (3.36)$$

where  $\omega$  is the frequency,  $k$  is the Boltzmann constant and  $T$  is the temperature in Kelvin. The resolution of the spectra is  $2 \text{ cm}^{-1}$ .

In a conventional force field calculation the total dipole moment  $M(t)$  is calculated from the atom-centered partial charges of the atoms. For the present simulations two possibilities were explored. In the first one, partial charges from a natural bond order (NBO) analysis (112) were calculated on the energy minimized structure for  $\text{H}_5\text{O}_2^+$  and protonated diglyme, respectively, using the electronic structure methods mentioned above. Secondly, for protonated water dimer the fully (15-)dimensional dipole moment surface of Huang *et al.* (113) was used to calculate  $M(t)$  from the coordinates along the trajectory.

For the MD simulations of protonated water dimer no partial charges were assigned to the atoms to avoid double counting of electrostatic interactions. This is not appropriate for protonated diglyme. Here we used scaled NBO partial charges in the MD simulations. The scaling was determined such as to reproduce the B3LYP/6-311++G(d,p) energies together with the morphing as closely as possible. A factor of 1/10 was found to be appropriate (see Figure 3.2.4 (C)).

### 3.2.3. Results

For both systems five independent MD simulations, 125 ps in length, were run at each temperature and averaged subsequently. The dynamics of the systems is analyzed using the atomic trajectories, the dipole-dipole time correlation functions and the corresponding infrared spectra. Power spectra for all internal motions of interest are calculated from the associated time series. These motions include the O–O stretch, the O–H\* stretch, and the O–H\*–O bending vibrations. The power spectra can be used

to reveal couplings between the different degrees of freedom.

### Energetics, Power and Infrared Spectra from MMPT/MD simulations

*Protonated water dimer:* The minimum energy structure of  $\text{H}_5\text{O}_2^+$  from MP2/6-311++G(d,p) calculations is shown in Figure 3.23(a). The O–O equilibrium distance is  $R_{\text{eq}} = 2.38$  Å with  $\rho_{\text{eq}} = 0.5$  and a slightly nonlinear structure  $\theta_{\text{O-H}^*-\text{O}} = 177^\circ$ . This is in agreement with other, higher-level *ab initio* calculations (113–115). The calculated MP2/6-311++G(d,p) *ab initio* energies (Figure 3.2.4 (A1)) and the fitted PES (Figure 3.2.4 (A2)) for  $\theta = 0$  are shown together in Figure 3.2.4 (D). The fit of the functional form to the *ab initio* points is satisfactory.

The infrared spectrum of  $\text{H}_5\text{O}_2^+$  and  $\text{DH}_4\text{O}_2^+$  at  $T = 5$  K (see Figure 3.2.4) was evaluated from the coordinates along the trajectories with the 15-dimensional dipole moment surface of Huang *et al.* (113) Spectral lines were assigned to particular motions using normal mode calculations and comparison between the H\* - and D\* -containing species (black and red curves, respectively). The OHO water bend is barely shifted ( $1772\text{ cm}^{-1}$  for  $\text{H}_5\text{O}_2^+$  and  $1767\text{ cm}^{-1}$  for  $\text{DH}_4\text{O}_2^+$ ), because the transferring H\*/D\* atom is essentially not involved in this mode. At lower frequency, small, broad features appear at  $1332\text{ cm}^{-1}$  and  $1260\text{ cm}^{-1}$  (center frequencies) for  $\text{H}_5\text{O}_2^+$  which shift to  $1126\text{ cm}^{-1}$  and  $1060\text{ cm}^{-1}$  upon deuteration. This corresponds to deuteration shifts of 1.19. Using normal mode analysis and the power spectra (Figure 3.2.4) of intermolecular coordinates, these bands are assigned to  $(\text{O-H}^*-\text{O})_{x,y}$  bending vibrations. However, the power spectra (Figure 3.2.4) suggest that the two modes are coupled to other modes. The peaks at  $890$  and  $856\text{ cm}^{-1}$  are essentially unshifted between the two isotopically substituted molecules and correspond to  $\text{H}_2\text{O}$  torsion coupled to the O–O stretch. At  $724\text{ cm}^{-1}$  the asymmetric OH\*O stretch appears which is shifted down to  $521\text{ cm}^{-1}$  upon deuteration. This is a deuteration shift of 1.39. At even lower wavenumbers ( $438\text{ cm}^{-1}$  and  $389\text{ cm}^{-1}$ , respectively), collective bending vibrations involving the bridging H\*/D\* atom appear.

Compared to the harmonic frequency from the MP2/6-311++G(d,p) calculations ( $899\text{ cm}^{-1}$ ) the asymmetric OH\*O stretch frequency is shifted considerably to the red ( $724\text{ cm}^{-1}$ ) which amounts to a relative shift of 24 %. There are a number of factors that potentially contribute to this observation. First, the asymmetric OH\*O coordinate has a substantial anharmonicity which will lower the frequency. As a comparison, in the ionic complex  $\text{He-HCO}^+$  the intermolecular stretching frequency (He-stretch) calculated from the second derivative of the potential at the minimum is found at  $140$

$\text{cm}^{-1}$  (MP2/aug-cc-pVTZ) whereas the anharmonic value is at  $87 \text{ cm}^{-1}$  (116). For a much more strongly bound system such as Ar-HCO<sup>+</sup> the harmonic (117) and anharmonic (118) frequencies along the intermolecular stretching coordinate are  $149.4 \text{ cm}^{-1}$  and  $132.8 \text{ cm}^{-1}$ , respectively. Thus, in these cases anharmonicity leads to a reduction of the harmonic value of 60 % and 13 % for the He and Ar-containing complex, respectively, which brackets the value for the asymmetric OH\*O stretch in H<sub>5</sub>O<sub>2</sub><sup>+</sup>. A second reason for the difference between the harmonic and anharmonic values is related to the accuracy of fitting the *ab initio* energies. Although the fit is satisfactory, small inaccuracies will affect the vibrational frequencies and lead to differences between *ab initio* calculations and the surfaces derived from them. Finally, the coupling between the various degrees of freedom in the quantum chemical calculations is likely to differ from the ones in the MMPT potential.

Since for a comparison with experiment simulations at higher temperature are more relevant, the infrared spectra of H<sub>5</sub>O<sub>2</sub><sup>+</sup> (black) and DH<sub>4</sub>O<sub>2</sub><sup>+</sup> (blue) were also calculated at 50 K. They are shown together with power spectra for selected coordinates of H<sub>5</sub>O<sub>2</sub><sup>+</sup> in Figure 3.2.4. Most experimental line positions (red bars), at  $750 \text{ cm}^{-1}$ ,  $900 \text{ cm}^{-1}$ ,  $1330 \text{ cm}^{-1}$ , and  $1770 \text{ cm}^{-1}$ , correspond to features in the calculated infrared spectra. The power spectra for the different coordinates are useful to detect couplings between different modes. Figure 3.2.4 shows that motion along the O-H\* coordinate (involved in the O-H\*-O asymmetric stretch) is coupled to the O-O stretching and the OH\*O and HOH\* bending coordinate. Together with the infrared spectrum, the power spectra are used to approximately assign the vibrational band. In addition to the assignments made in the previous paragraph, the O-O mode is found at  $617 \text{ cm}^{-1}$  which agrees quite favorably with  $630 \text{ cm}^{-1}$  from MD simulations on the CCSD(T)/aug-cc-pVTZ surface (93). It is also observed that the infrared spectrum does not show a band around  $600 \text{ cm}^{-1}$ . This is expected because the symmetric O-O stretch is infrared inactive.

Table 3.5 presents harmonic and anharmonic frequencies for the O-O symmetric and the O-H\*-O asymmetric stretch and the two O-H\*-O bending vibrations. Data are shown from BCCD(T)/TZ2P calculations (115) and calculations on the OSS3(p) PES (113, 114), the most recent CCSD(T)/aug-cc-pVTZ PES (113) and MP2/6-311++G\*\*, the method used for the MMPT potential. All harmonic frequencies agree fairly well. However, their value in understanding the experimental spectra is very limited because of the anharmonicities and the flat PES along different coordinates. The lower part of Table 3.5 compares anharmonic frequencies calculated on the OSS3(p) PES

using 15-dimensional vibrational configuration interaction (VCI) (91) or Quantum Monte Carlo (CFQMC) calculations (98) along with MD simulations on the CCSD(T)/aug-cc-pVTZ (93) and the MMPT (this work) potential energy surfaces at 100 K. The O–O stretching vibration on the OSS3(p) is lower by about  $50\text{ cm}^{-1}$  to  $100\text{ cm}^{-1}$  compared to the other two PESs whereas the two MD simulations give quite similar results. For the O–H\*–O asymmetric stretch QMC calculations on the OSS3(p) PES yield two modes with considerable O–H\*–O amplitude ( $737$  and  $870\text{ cm}^{-1}$ ) whereas the VCI calculations find one mode at  $902\text{ cm}^{-1}$ . The MD simulations have this mode at  $861\text{ cm}^{-1}$  and  $830\text{ cm}^{-1}$ . Cho and Singer (98) observe that, while they use the same PES as Dai *et al.*, it is not clear, which of the two O–H\*–O asymmetric stretch modes from the CFQMC calculations correspond to the  $902\text{ cm}^{-1}$  mode from the VCI calculations. Finally, O–H\*–O bending vibrations from VCI and MD simulations are in the  $1300\text{ cm}^{-1}$  region. It was previously found (99) that, depending on the method and the PES, the splitting between the  $(\text{O–H}^*\text{–O})_x$  and  $(\text{O–H}^*\text{–O})_y$  bend ranges from 11 to  $58\text{ cm}^{-1}$  which agrees with  $55\text{ cm}^{-1}$  from the actual simulations. The almost quantitative agreement with MD simulations on the 15-dimensional CCSD(T) surface and the fair agreement with different calculations on the OSS3(p) potential suggest that the MMPT surface is of sufficiently high quality to serve as a zeroth-order approximation for morphing and use in a related system such as protonated diglyme.

*Protonated diglyme:* The fully relaxed B3LYP/6-311++G(d,p) PES along  $R$  and  $\rho$  is shown in Figure 3.2.4 (B1). It exhibits a faint double-minimum structure with a barrier for PT below  $0.2\text{ kcal/mol}$ . Constraining the molecule at its MP2/6-311++G(d,p) optimized geometry this barrier is calculated to be  $1.2\text{ kcal/mol}$  which is an upper limit at this level of theory and is considerably lower than the previously reported value of  $4.6\text{ kcal/mol}$  (78). Comparison of the PES for protonated diglyme and for  $\text{H}_5\text{O}_2^+$  shows that at large  $R$  the PES is flatter for the former. Since the topologies of the two PESs shown in Figures 3.2.4 (A1) and (B1) are similar, a 3-dimensional PES for describing PT in protonated diglyme can be derived from the PES for proton transfer in  $\text{H}_5\text{O}_2^+$  in the following way. In the spirit of the original morphing (32) and previous PES-scaling approaches (119), the surface for proton transfer in  $\text{H}_5\text{O}_2^+$  is used as a zeroth-order approximation and related to PT in protonated diglyme *via* the transformation  $\tilde{V}_{\text{diglyme}}(R, \rho, \theta) = \lambda_1 V(\lambda_2 R, \rho, \theta)$ . To determine approximate morphing parameters, the fully relaxed B3LYP/6-311++G(d,p) PES along  $V(R, \rho, \theta = 0)$  serves as the reference.

The most obvious difference between the B3LYP/6-311++G(d,p) PES for protonated diglyme and the MP2/6-311++G(d,p) PES for protonated water (compare Figures 3.2.4 (B1) and 3.2.4 (A1)) is the location of the O–O minimum (2.38 Å in  $\text{H}_5\text{O}_2^+$  compared to 2.43 Å in protonated diglyme) and the curvature around the minimum: for protonated diglyme the interaction potential is flatter than for  $\text{H}_5\text{O}_2^+$  at large  $R$ . By applying  $\tilde{R} = \lambda_1 R$  and  $\tilde{E} = \lambda_2 E$  with  $\lambda_1 = 1.025$  and  $\lambda_2 = 0.95$  to the protonated water dimer PES it can be transformed into a PES suitable for describing PT in protonated diglyme. This is the MMPT PES for protonated diglyme. Figures 3.2.4 (B1) and (B2) compare the B3LYP/6-311++G(d,p) PES and  $\tilde{V}_{\text{diglyme}}(R, \rho, \theta)$ . Around the minimum, the region probed by the MD simulations, the two PESs are very similar (see Figure 3.2.4 (C) which compares the two PESs for  $R_{\text{OO}}^{\text{min}}$ , i.e. the cut for  $R_{\text{OO}} = \text{const}$  through the minimum of the respective PES) while for larger  $R$  the curvature of the morphed PES differs from the B3LYP/6-311++G(d,p) PES. Once sufficient reference data is available, a more detailed morphing can be envisaged. However, the dynamics on PES (B2) shows that motion along  $R$  is restricted to the phase space enclosed by the 0.2 kcal/mol contour, i.e.  $R \leq 2.5$  Å which is the region where (B1) and (B2) are very similar.

Molecular dynamics simulations for protonated diglyme ( $[\text{diglyme-H}]^+$  and  $[\text{diglyme-D}]^+$ ) were run using the morphed  $\tilde{V}_{\text{diglyme}}(R, \rho, \theta)$  for the transferring proton/deuteron. From the total dipole moment  $M(t)$  the infrared spectrum and power spectra along coordinates relevant for proton transfer were calculated. The power spectra reveal considerable coupling between the different modes. For better assignments in particular of the modes involving the bridging proton  $\text{H}^*$ , spectra were calculated at low temperature (1 K, see Figure 3.2.4). To assist the assignments of the lines, MD simulations were carried out by varying the mass of the transferring particle between 1 and 2 amu in steps of 0.2 amu. The averaged spectra display a number of lines that exclusively appear in the hydrogenated and deuterated species, respectively. First the asymmetric  $\text{OH}^*\text{O}$  stretching vibration is assigned. With increasing mass of the transferring particle the band at  $870\text{ cm}^{-1}$  shifts progressively down to  $635\text{ cm}^{-1}$ . Furthermore, comparison of the power spectra (as was done for  $\text{H}_5\text{O}_2^+$ , see Figure 3.2.4) of the  $\text{OH}^*$  and  $\text{OD}^*$  stretching coordinates establishes this assignment. The deuteration shift for the asymmetric  $\text{OH}^*\text{O}$  stretch is 1.37, somewhat lower than for protonated water dimer (1.39).

Additional sets of lines ( $1340\text{ cm}^{-1}$  and  $1400\text{ cm}^{-1}$ ) and ( $1100\text{ cm}^{-1}$  and  $1210\text{ cm}^{-1}$ ) have deuteration shifts of 1.20 and 1.16, compared to shifts of 1.19 for  $\text{OH}^*\text{O}$  bending



modes in  $\text{H}_5\text{O}_2^+$ . Their assignment to OH\*O bending motions is not as firm as for the asymmetric OH\*O stretch. Starting from the blue end of the spectrum, the two lines above  $1450\text{ cm}^{-1}$  are not influenced by isotopic substitution and thus are not involved in either H\* stretching or bending motion. Conversely, the congested spectral pattern around  $1400\text{ cm}^{-1}$  in [diglyme-H]<sup>+</sup> has only one line in the deuterated species. Thus, the pattern around  $1400\text{ cm}^{-1}$  must be related to H\* motion. Deuteration shifts of H-bending vibrations are expected between 1.1 and 1.2. A comparison of the two spectra in Figure 3.2.4 shows that the lines at  $1210\text{ cm}^{-1}$  and  $1100\text{ cm}^{-1}$  in [diglyme-D]<sup>+</sup> have no companion in the [diglyme-H]<sup>+</sup> spectrum. This suggests the correspondence as indicated in Figure 3.2.4. Normal mode analysis based on both, the MMPT surface and the optimized B3LYP/6-311++G(d,p) level confirm that these lines involve the OH\*O in-plane bending vibration which is, however, strongly mixed with other degrees of freedom. The relative intensities of the lines differ partly due to the simplified model used for the dipole moment (see e.g. the lines at  $1500$  and  $1550\text{ cm}^{-1}$ ). Further experiments on the deuterated species will help in the assignment of the lines.

*Comparison of the MMPT/MD simulations for  $\text{H}_5\text{O}_2^+$  and protonated diglyme:* Figure 3.2.4 shows IR spectra for  $\text{H}_5\text{O}_2^+$  at 5 K, 50 K, 100 K and 350 K (calculated from 5 trajectories) and for protonated diglyme at 10 K and 50 K. It is apparent that the spectra of  $\text{H}_5\text{O}_2^+$  are considerably more affected by temperature than the ones for protonated diglyme. The temperature dependence of the  $\text{H}_5\text{O}_2^+$  spectra has already been found previously (93, 100).

The dominant asymmetric stretching vibrations are at different frequencies in  $\text{H}_5\text{O}_2^+$  and in [diglyme-H]<sup>+</sup>. In  $\text{H}_5\text{O}_2^+$  the O–H\*–O asymmetric stretching vibration shifts from  $724\text{ cm}^{-1}$  (at 5 K) to  $830\text{ cm}^{-1}$  (at 100 K) whereas it is at  $870\text{ cm}^{-1}$  in protonated diglyme at all temperatures investigated. One possible explanation for this observation is that the molecular scaffold couples differently to the PT motif in protonated diglyme compared to  $\text{H}_5\text{O}_2^+$ , i.e. that the relatively free motion of the water molecules along the OH\*O motif in  $\text{H}_5\text{O}_2^+$  has a different influence on the spectroscopy than the more constrained motion of H\* in the  $\text{H}_3\text{C}-\text{CH}_2\text{O}-\text{H}^*-\text{OCH}_2-\text{CH}_3$  motif in [diglyme-H]<sup>+</sup> (see Figure 3.23). The coupling between stretch and bending vibrations to the OH\*O asymmetric stretch in [diglyme-H]<sup>+</sup> has been assessed through modifications of particular force field parameters. Possible candidates that can couple to the OH\*O motion in [diglyme-H]<sup>+</sup> include the CO bond, and the COC and CCO valence an-

gles (see Figure 3.23). The particular force constants (see Table 3.4) were varied by  $\pm 10\%$  and the infrared spectrum was calculated as before. Compared to the center value ( $k_{\text{C-OH}} = 450 \text{ kcal/mol/\AA}^2$ ) the band at  $870 \text{ cm}^{-1}$  shifts to  $874 \text{ cm}^{-1}$  and  $865 \text{ cm}^{-1}$  for a stronger or weaker  $k_{\text{C-OH}}$ , respectively. Modifications of the angular force constants, which are typically weaker than stretching force constants by a factor of 10, have smaller effects on the location of the OH\*O asymmetric stretch. The same is observed for modifications of  $k_{\text{COC}}$ . In summary, the frequency of the asymmetric stretching motion in [diglyme-H]<sup>+</sup> is coupled to the environmental degrees of freedom, but changes in the force constants by up to 10% shift the frequency by no more than  $10 \text{ cm}^{-1}$ .

### 3.2.4. Discussion and Conclusion

In this work, the MMPT potential has been used to investigate proton transfer dynamics and to characterize the infrared spectra of  $\text{H}_5\text{O}_2^+$  and protonated diglyme. The MMPT potential allows us to investigate the long-time (several 100 ps) bond-breaking and bond-forming (i.e. reactive) dynamics similar to mixed QM/MM MD simulations. The vibrational spectra were calculated from the dipole-dipole autocorrelation function and assignments were made using simulations with deuterated species and power spectra calculated along the most relevant coordinates. For protonated water dimer a state-of-the-art 15-dimensional dipole moment surface (113) was used to calculate the infrared spectrum while for [diglyme-H]<sup>+</sup> only a point charge model is available. The quality of the MMPT PES for  $\text{H}_5\text{O}_2^+$  was validated by comparing vibrational excitations with previous MD, DMC, and VCI calculations on high-quality PESs. The results suggest that the MMPT PES is suitable as a zeroth-order approximation for other proton transfer motifs of the form  $\text{XO}\cdots\text{H}^+\cdots\text{OX}$ , such as in protonated diglyme. The recent MD simulations by Bowman and coworkers on a high-quality, 15-dimensional PES bear most similarities with the present investigation (113). For 100 K they find the asymmetric O-H\*-O stretching vibration (possibly coupled with a torsional mode) at  $860 \text{ cm}^{-1}$  which agrees favorably with the  $830 \text{ cm}^{-1}$  at the same temperature calculated with the MMPT potential. Furthermore, the infrared inactive symmetric OH\*O stretching vibration is found at  $620 \text{ cm}^{-1}$  (see Figure 3.2.4) while Bowman *et al.* find it at  $630 \text{ cm}^{-1}$  (93). Deuteration shifts for the vibrations involving the transferring H\* are 1.39 and 1.19 for the asymmetric O-H\*-O stretching and bending modes from MMPT/MD simulations which compares with

1.33 and 1.25 from VCI calculations on the OSS3(p) PES (91).

Meaningful *ab initio* MD simulations for protonated diglyme at the correlated level (e.g. MP2) are beyond current computing power, and probably remain so for the foreseeable future. Even calculating and fitting a relaxed 3d PES for protonated diglyme at the B3LYP/6-311++G(d,p) level would be extremely laborious. Thus, alternative computational methodologies beyond the harmonic approximation are required to follow the proton motion and to understand the associated spectroscopy in a system such as [diglyme-H]<sup>+</sup>. Here, the intermolecular potential was formulated in a manner inspired by mixed QM/MM methods and an approximate energy- and coordinate-scaling was applied to the 3d PES for H<sub>5</sub>O<sub>2</sub><sup>+</sup> to reproduce the shape and major features of the 2d relaxed PES for protonated diglyme. This morphed PES was subsequently used in long MD simulations. For [diglyme-H]<sup>+</sup> a one-to-one comparison of the vibrations with assignments from experiment is difficult. This is mainly because coupling between modes leads to mixing between “pure” O···H<sup>+</sup>···O asymmetric stretch and in- or out-of-plane bend modes decoupled from other framework vibrations. From careful analysis and comparison with simulations of the deuterated species, the bands at 870 cm<sup>-1</sup>, 1340 cm<sup>-1</sup> and 1400 cm<sup>-1</sup> are assigned to the O···H<sup>+</sup>···O asymmetric stretch and in-plane bending modes, respectively. For the O···H<sup>+</sup>···O asymmetric stretch this compares with frequencies between 724 cm<sup>-1</sup> and 830 cm<sup>-1</sup> in H<sub>5</sub>O<sub>2</sub><sup>+</sup>, depending on the temperature. Thus, it is possible that the experimentally observed spectral features for protonated diglyme below 800 cm<sup>-1</sup> indeed belong to the O···H<sup>+</sup>···O asymmetric stretch (78).

It is possible that quantum effects, in particular proton tunneling and zero-point effects, modify the spectra. On the other hand, it has previously been shown that although classical MD simulations neglect quantum effects, they are useful for interpreting vibrational spectra of molecular species (93). Quantum effects are expected to play an important role at low temperature. However, most of the vibrationally resolved spectra that probe the H<sup>+</sup>-transfer region are from studies with high laser power (1, 77, 78). As such, the measured spectra likely involve fairly hot species with considerable amounts of internal energy where quantum effects are usually found to be of minor importance. Even studies under relatively mild experimental conditions found internal temperatures between 130 K and 170 K in NH<sub>4</sub><sup>+</sup>(H<sub>2</sub>O)<sub>n</sub> clusters for ( $n \leq 6$ ) (120).

The advantage of the present simulations is that they take the full dimensionality of the phase space into account. For strongly bound clusters and molecules tem-

temperatures can be derived from the widths of rotational line profiles and the assignment of hot bands. However, for a floppy system such as  $\text{H}_5\text{O}_2^+$  with a strongly anharmonic potential the available phase space and the effective potential on which the dynamics takes place can change as a function of temperature. The shifting and broadening of vibrational bands associated with  $\text{H}^+$  displacement has been previously found in classical MD spectra of  $\text{H}_5\text{O}_2^+$  (93, 100) and is confirmed by the present simulations. This is in contrast to protonated diglyme where, as expected, no temperature dependence of the vibrational bands is found. Linear extrapolation of the band maximum of the asymmetric O–H\*–O stretch in  $\text{H}_5\text{O}_2^+$  from Figure 3.2.4 to  $921\text{ cm}^{-1}$  yields  $T \approx 200\text{ K}$  which is somewhat higher than previously estimated temperatures in supersonic jets (120). A more recent study of the infrared spectroscopy of larger protonated water clusters has estimated the excess internal energy in the  $\text{H}^+[\text{H}_2\text{O}]_{21}$  cluster to be around 1.5 eV, which amounts to 270 K per soft degree of freedom (121).

It is of interest to compare the IR spectra calculated from the fully-dimensional dipole moment surface (113) and from a simpler point-charge description. To this end five additional MD simulations at 10 K were carried out for  $\text{H}_5\text{O}_2^+$  and  $M(t)$  was calculated from these trajectories using the two different models. The averaged spectra are shown in Figure 3.2.4. It is found that the positions of the lines are essentially identical whereas the relative intensities can differ considerably. In particular, the region around  $1300\text{ cm}^{-1}$  appears far more intense using the NBO charges. This suggests that the potential energy surface largely determines the location of the spectral lines whereas accurate knowledge of the dipole moment surface provides realistic relative intensities.

Previously, the “morphing potential” approach has been successfully used for complexes such as Ne–HF, Ar–HBr or He–OCS (32, 105, 122). It is important to stress that the final potential is an *effective* potential which means for the above systems that it is only valid for the frozen monomer configuration (e. g. HF bond length in Ne–HF) chosen. This is also true for the present work. Once firm assignments are available, the MMPT potential for  $\text{H}_5\text{O}_2^+$  itself can be systematically improved to optimally reproduce the experimental observables and will yield an effective MMPT surface which is valid for the force field parameters chosen. In the present work we applied the morphing procedure in a slightly different manner, namely to approximately morph an initial PES to reproduce the *ab initio* surface for proton transfer in protonated diglyme. The morphed surface was then used to explore the vibrational states of the molecule. It is of interest to mention that the present approach should

also be suitable to investigate systems in the condensed phase. For example, it is possible to solvate the system in question (e.g. protonated water dimer) and to calculate its spectroscopic properties from an MD simulation. Comparison with experimental data will provide the necessary data to apply the morphing procedure. This will involve iterative, non-linear least squares fitting of the calculated values to the experimental data.

In summary, the present work reports computational studies of the relationship between the infrared spectra for  $\text{H}_5\text{O}_2^+$  and  $[\text{diglyme-H}]^+$  in view of their common proton-transfer motif. The underlying PES is suitable to describe proton transfer and is based on a morphed, 3-dimensional PES which explores the similarity between  $\text{H}_5\text{O}_2^+$  and protonated diglyme. The MMPT surface for  $\text{H}_5\text{O}_2^+$  was validated against recent MD simulations. Comparison of the infrared spectra of  $[\text{diglyme-H}]^+$  and  $\text{H}_5\text{O}_2^+$  show that there is not necessarily a straightforward relationship between these spectra which would allow for an assignment of the bands. Based on the present investigations it is however possible that the experimentally observed feature below  $800\text{ cm}^{-1}$  corresponds to the asymmetric O–H\*–O stretch. It is also found that, as expected, the infrared spectrum of  $[\text{diglyme-H}]^+$  is largely unaffected by temperature whereas the bands in  $\text{H}_5\text{O}_2^+$  considerably shift and broaden. For the as yet unobserved infrared spectrum of  $[\text{diglyme-D}]^+$  a deuteration shift of 1.37 for the asymmetric OH\*O stretch is predicted. Experimental studies of  $[\text{diglyme-D}]^+$  would be useful to test this proposition.

Table 3.2: The parameter set for the fit of of the proton transfer potentials in  $\text{H}_5\text{O}_2^+$  (see Eqs. (2) to (7)).

$D_e(R)$		$\beta(R)$		$\rho_{\text{eq}}(R)$	
$p_1$	141.902 kcal/mol	$p_5$	$-0.977 \text{ \AA}^{-1}$	$p_7$	$357.171 \text{ \AA}$
$p_2$	$2.229 \text{ \AA}^{-1}$	$p_6$	$1.348 \text{ \AA}^{-2}$	$p_8$	$3.393 \text{ \AA}^{-1}$
$p_3$	1.960			$p_9$	$0.102 \text{ \AA}$
$p_4$	11.879 kcal/mol				
<hr/>			<hr/>		
$k$		$c$			
$p_{10}$	0.009 kcal/mol	$p_{11}$	35.621 kcal/mol/deg		

Table 3.3: Atom types for  $\text{H}_5\text{O}_2^+$  and protonated diglyme from the CHARMM22 force field (13).

$\text{H}_5\text{O}_2^+$		Protonated diglyme	
Atom Type	Atom Number	Atom Type	Atom Number
H	H1 ... H5	H	H1 ... H15
O	O1, O2	C	C1 ... C6
		O	O2
		OH	O1, O3

Table 3.4: Force field parameters for bonded and non-bonded interactions for  $\text{H}_5\text{O}_2^+$  and protonated diglyme from the CHARMM22 force field (13).

Bond			Angle			Dihedral				Nonbonded		
Atoms	$k$	$r_e/\text{\AA}$	Atoms	$k$	$\theta_e/^\circ$	Atoms	$k$	$n$	$\phi_e/^\circ$	Atoms	$\epsilon$	$\sigma/\text{\AA}$
O H	550.0	0.9572	H O H	55.0	104.52					H	-0.046	0.2245
										O	-0.1521	1.7682

protonated diglyme												
O C	450.0	1.45	H O H C	50.0	120.0	O H C C H	0.25	2	180.0	H	-0.046	0.2245
O H C	450.0	1.45	C O C	50.0	130.0	O C C H	0.25	2	180.0	O	-0.12	1.7
O H H	450.0	1.00	C O H C	50.0	120.0	H C C H	0.25	2	180.0	OH	-0.12	1.7
C C	450.0	1.45	C C O	50.0	140.0	C O C H	0.25	2	180.0	C	-0.11	2.0
C H	320.0	1.10	C C H	35.0	110.0	C O H C C	0.25	2	180.0			
			O C H	35.0	110.0	C O C C	0.25	2	180.0			
			C C O H	50.0	140.0	O H C C O	0.25	2	180.0			
			C O H	60.0	115.0	H O H C C	0.25	2	180.0			
			H C H	35.0	109.0	C O H C H	0.25	3	180.0			
			O H C H	50.0	109.0	H C O H H	0.25	3	180.0			

Table 3.5: Comparison of harmonic (upper half) and anharmonic frequencies (lower half) for stretching and bending modes involving the transferring H\* and the symmetric O–O stretching vibration in  $\text{H}_5\text{O}_2^+$ . Data from the literature and the present calculations are compared. The two states for the asymmetric O–H\*–O stretch from the CFQMC calculations contain a significant amplitude along this mode (98). For the anharmonic frequencies, the first header refers to the interaction potential and the second line to the method to calculate the vibrational frequencies. n.a. labels states for which no assignment has been made in the respective works. Frequencies are given in  $\text{cm}^{-1}$ . \*The MD simulations in Ref. (93) do not give the anharmonic frequencies themselves but the overlap matrix between the driven frequencies with the normal modes. For example, driving at  $860 \text{ cm}^{-1}$  leads to considerable overlap with the normal mode at  $861 \text{ cm}^{-1}$  and some overlap with the mode at  $630 \text{ cm}^{-1}$ .

Harmonic Vibrational Frequencies				
Mode	Ref. (115) BCCD(T)/TZ2P	Ref. (113, 114) OSS3(p)	Ref. (113) CCSD(T)/a-VTZ	This work MP2/6-311++G**
O–O stretch	650	688	630	633
OH*O <sub>as</sub> stretch	794	857	861	899
OH*O <sub>x</sub> bend	1505	1486	1494	1516
OH*O <sub>y</sub> bend	1596	1505	1574	1564
Anharmonic Vibrational Frequencies				
	OSS3(p) VCI (15d) (91)	OSS3(p) CFQMC (98)	CCSD(T)/a-VTZ MD 100K (93)	MMPT MD 100K
O–O stretch	569	$516 \pm 4$	630*	617
OH*O <sub>as</sub> stretch	902	$737 \pm 3$ $870 \pm 6$	861*	830
OH*O <sub>x</sub> bend	1354	n.a.	n.a.	1266
OH*O <sub>y</sub> bend	1388	n.a.	n.a.	1321



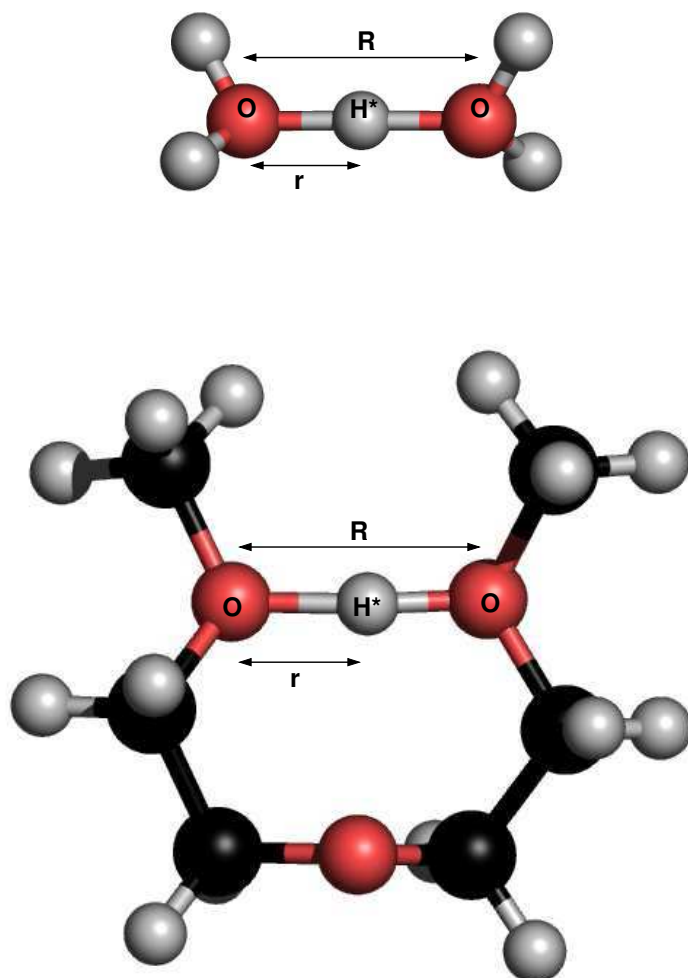


Figure 3.23: Minimum energy structures of (a) protonated water dimer at the MP2/6-311++G(d,p) level of theory and (b) protonated diglyme (b) at the B3LYP/6-311++G(d,p) level of theory. The heavy-heavy distance ( $\text{O} \cdots \text{O}$ ) is  $R$ , while the hydrogen coordinate is  $r$  and the angle  $\theta$  is the angle between the two. For the linear arrangement  $\theta = 0$ . The transferring hydrogen/deuteron is labelled  $\text{H}^*/\text{D}^*$

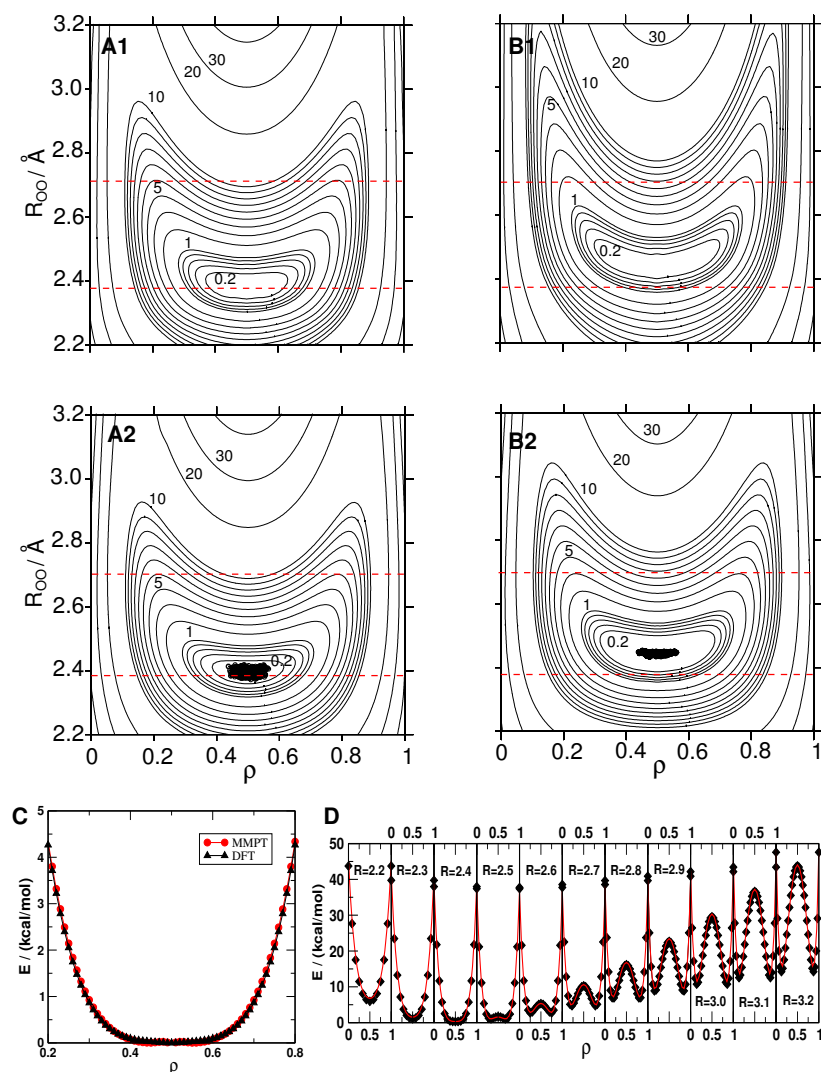


Figure 3.24: (A1) Relaxed PES scan from MP2/6-311++G(d,p) calculations for the hydrogen bridge for oxygen-oxygen distances  $R_{OO}$  from 2.2 to 3.2  $\text{\AA}$  and  $\rho$  ranging from 0 to 1 and  $\theta = 0^\circ$  for  $H_5O_2^+$ . The minimum energy is found at  $R = 2.38 \text{ \AA}$  and  $r = 1.19 \text{ \AA}$  (i.e.  $\rho = 0.5$ ). (A2) Fitted PES from the analytical energy function using the fitted parameters (Eqs. (2) to (7) and Table 3.2). (B1) PES along the PT coordinates ( $R, \rho$ ) for protonated diglyme from B3LYP/6-311++G(d,p) calculations. (B2) MMPT (morphed potential of (A2)) with  $\lambda_1 = 1.025$  (shift of equilibrium geometry) and  $\lambda_2 = 0.95$  (flattening of the PES). Contours are drawn every 0.2 kcal/mol up to 1 kcal/mol, then every 1 kcal/mol up to 10 kcal/mol and at 20 kcal/mol and 30 kcal/mol. The dashed red lines guide the eye to compare the two sets of surfaces. They cross through the minimum of the  $H_5O_2^+$  potential and through the line at 5 kcal/mol at long range. Computationally, (A1) and (B1) correspond to the “expensive” PESs while (A2) and (B2) are rapid to evaluate. (A2) and (B2) also show the phase space sampled by a typical trajectory at 50 K. (C) Comparison of the B3LYP/6-311++G(d,p) potential and the MMPT potential for  $R_{OO} = \text{const.}$  through the minimum of the respective PES. (D) Calculated MP2/6-311++G(d,p) energies (diamonds) for  $H_5O_2^+$  and fitted (solid line) analytical form for the PES as a function of  $\rho$  for 11 cuts  $R = \text{const.}$  and for  $\theta = 0$ . Energies are in kcal/mol.

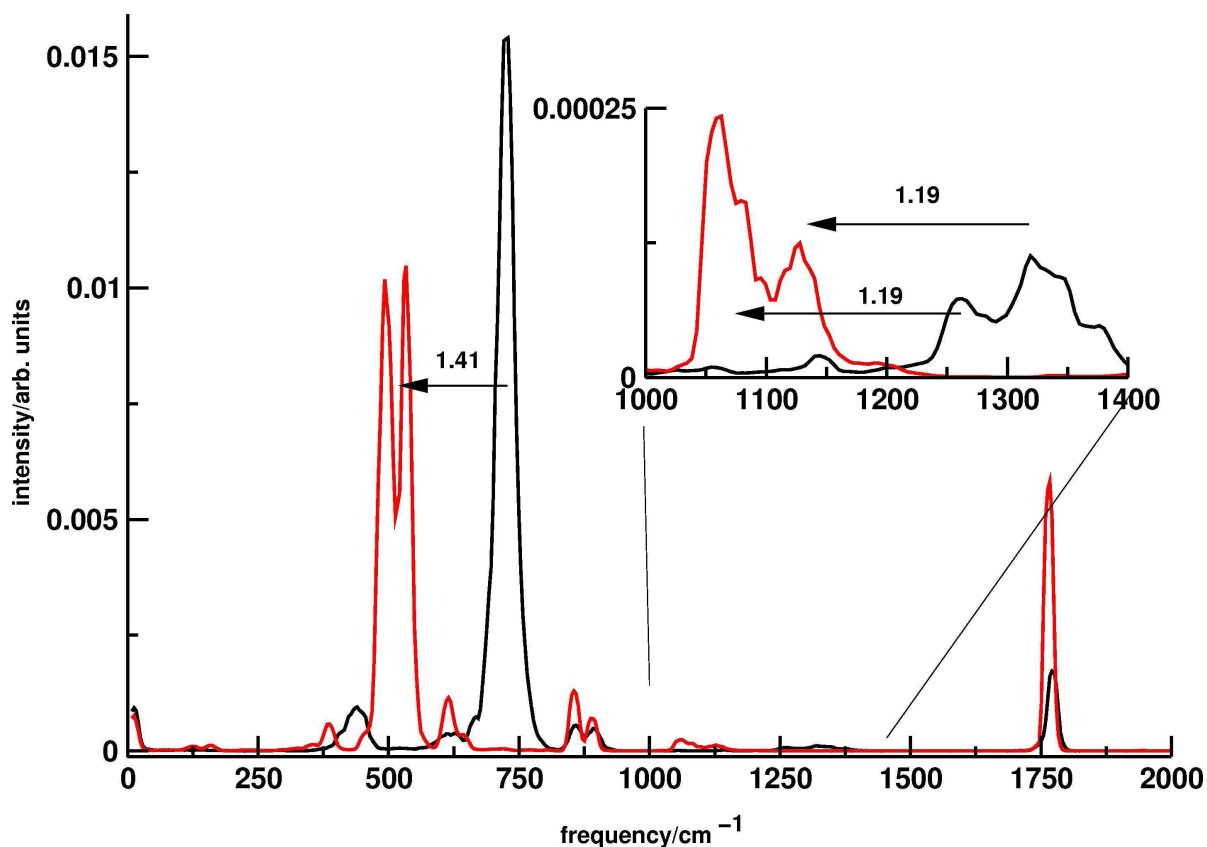


Figure 3.25: Averaged infrared spectra for  $\text{H}_5\text{O}_2^+$  (black trace) and  $\text{DH}_4\text{O}_2^+$  (red trace) from MMPT/MD simulations at 5 K. The spectra are calculated from the 15-dimensional dipole moment surface by Huang et al. (see text) (113) and averaged over 5 runs. Isotope shifts are given as horizontal arrows. The inset shows a magnification of signal in the bending region (see Table 3.5) with corresponding isotope shifts. The HOH bending mode is essentially unshifted. All spectra are normalized to unity.

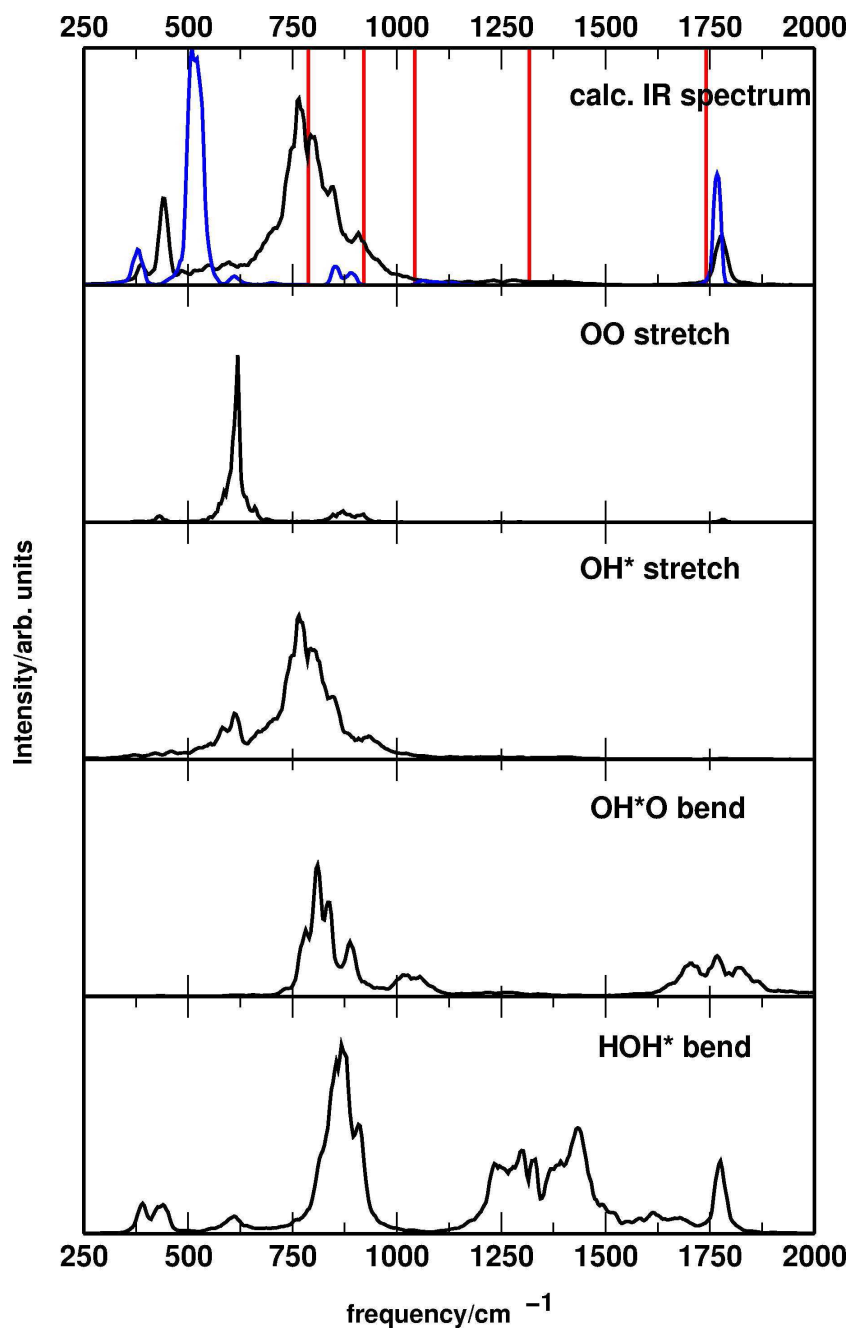


Figure 3.26: Averaged infrared spectra for  $\text{H}_5\text{O}_2^+$  (black) and  $\text{DH}_4\text{O}_2^+$  (blue) at 50 K (top panel) together with the experimental line positions (red bars for wavenumbers). The four lower panels show the averaged power spectra of the O–O and OH\* stretching, and the OH\*O and HOH\* bending vibrations, respectively.

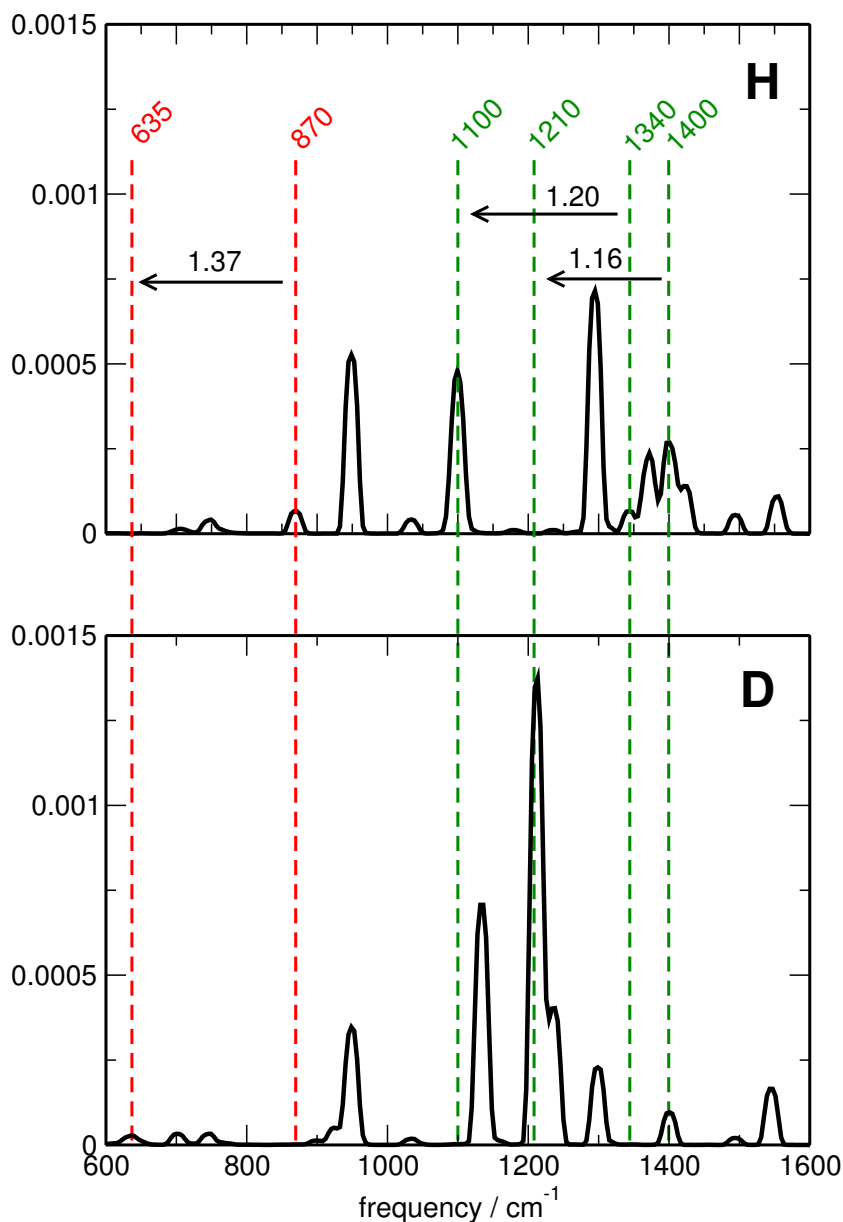


Figure 3.27: Averaged infrared spectra for protonated diglyme from MMPT/MD simulations at 1 K. Spectra for different masses of the transferring particle ( $m_{\text{H}^*}=1.008$  amu,  $m_{\text{D}^*}=2.016$  amu) and lines connecting corresponding peaks are shown. Energies are in  $\text{cm}^{-1}$  and intensities in arbitrary units. The red dashed lines are for spectral features corresponding to the OH\*O asymmetric stretch while the green dashed lines are for the bending modes that are present in the  $[\text{diglyme-H}]^+$  and in  $[\text{diglyme-D}]^+$ , respectively. Corresponding deuteration shifts are indicated by horizontal arrows.

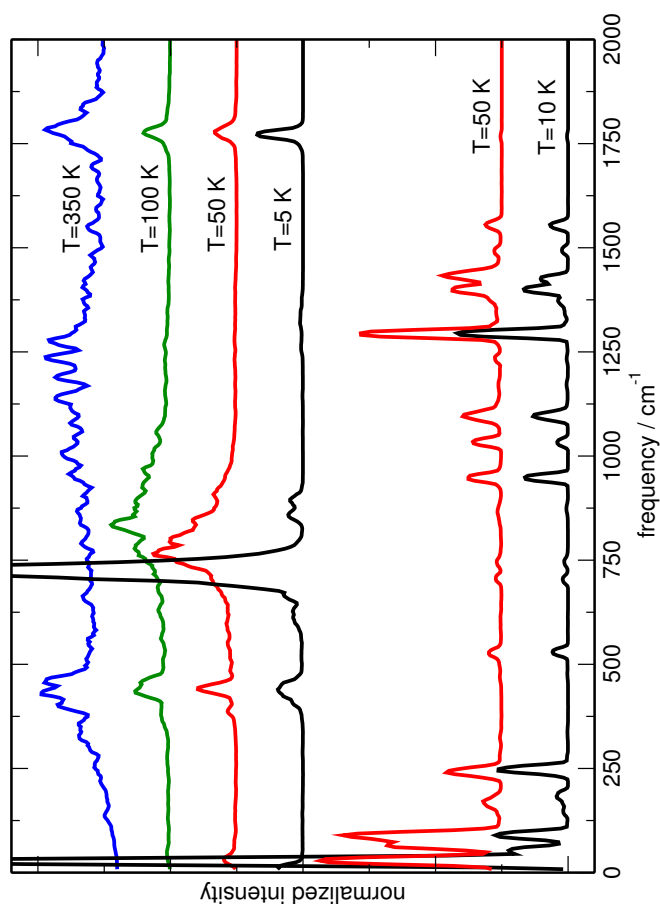


Figure 3.28: Infrared spectra for  $\text{H}_5\text{O}_2^+$  (upper four traces) and protonated diglyme (lower two traces) from MMPT/MD simulations. Temperature effects are found to be small for protonated diglyme while they are more pronounced for  $\text{H}_5\text{O}_2^+$ . Energies are in  $\text{cm}^{-1}$  and intensities in arbitrary units. The quality of the dipole moment surface for  $\text{H}_5\text{O}_2^+$  and  $[\text{diglyme-H}]^+$  is not comparable (see text).

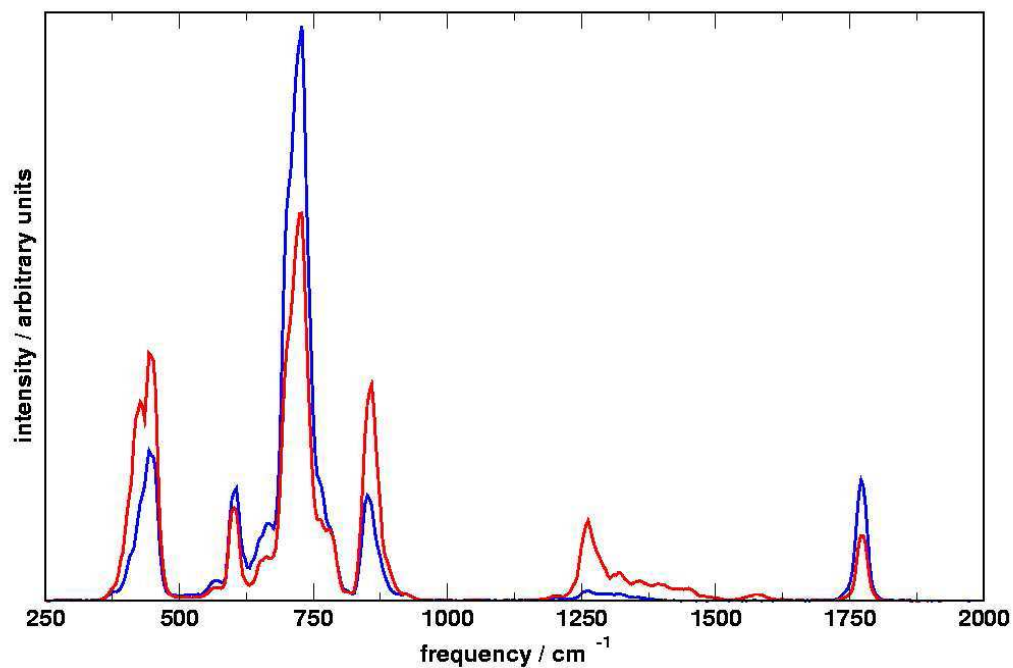


Figure 3.29: Averaged infrared spectra for  $\text{H}_5\text{O}_2^+$  at 10 K calculated from atom-centered, partial NBO charges (red curve) and from the 15-dimensional dipole moment surface (blue curve). The positions of the lines are essentially identical whereas their intensities depend on the model from which  $M(t)$  is calculated. This is particularly apparent for the region around  $1300\text{ cm}^{-1}$  which is related to the HOH\* bending vibrations.





## 4. Published Work

The following paper appeared as

S. Lammers and M. Meuwly, *Australian Journal of Chemistry*, **57(12)** 1223–1228 (2004).

## Double Proton Transfer using Dissociable Force Fields

Sven Lammers<sup>A</sup> and Markus Meuwly<sup>A,B</sup>

<sup>A</sup> Department of Chemistry, University of Basel, 4056 Basel, Switzerland.

<sup>B</sup> Corresponding author. Email: m.meuwly@unibas.ch

The construction, implementation, and use of dissociable classical force fields are discussed. Starting from zeroth-order interaction potentials for  $\text{O}_2\text{H}_5^+$  and  $\text{N}_2\text{H}_7^+$  calculated with MP2/6-311++G\*\*, energy scaling of the potential energy surfaces allows adjustment of quantities such as the barrier heights to describe a range of physical situations observed in realistic systems. As an example, ‘potential morphing’ is used to investigate the dynamics of double proton transfer in 2-pyridone · 2-hydroxypyridine for which previous estimates of the barrier to tautomerization are available. Scaling factors to give barrier heights for double proton transfer between 3.6 and 17.6 kcal mol<sup>-1</sup> are chosen to demonstrate the utility of the method to describe a range of different barrier heights and shapes. Considerable savings in computing time can be achieved compared to alternative methods such as mixed quantum/classical methods.

Manuscript received: 14 July 2004.

Final version: 21 September 2004.

Classical force fields (CFFs) have made possible the study of the energetics and dynamics of quite complex processes in molecular and condensed phase systems.<sup>[1]</sup> Together with the time propagation of the coordinates and velocities, a wide range of physical properties of a system can be described by such an approach. However, one of the shortcomings of CFFs is that it is difficult to describe rearrangements of the bonding pattern in molecular systems because the connectivity between the atoms remains the same throughout a simulation. With mixed quantum mechanical/molecular mechanics (QM/MM) methods some of these difficulties could be overcome.<sup>[2-4]</sup> There also exist empirical valence bond (EVB) models for chemical reactions which mix two or more diabatic potential energy surfaces (PESs) in an empirical fashion, that eventually lead to an adiabatic surface on which to propagate the system.<sup>[5]</sup> However, their construction starts from a molecular orbital picture that takes electronic interactions in a more empirical way into account.

Here we describe a method by which it is possible to break and form bonds in a molecular system and that retains the central ideas and advantages of CFFs such as speed and ease of use. In addition, the present approach allows adjustment of the shape and energetics of the PES by using energy, and eventually coordinate, scalings. This so-called ‘morphing’ of PESs has already been successfully used in fitting PESs to high-resolution spectroscopic data of small van der Waals complexes.<sup>[6-9]</sup> The construction and implementation of the method in molecular dynamics simulations are described and tested for the double proton transfer (DPT) reaction in 2-pyridone · 2-hydroxypyridine (2PY · 2HPY).<sup>[10-12]</sup>

Double proton transfer has attracted considerable interest over the past few years. This stems from both detailed spectroscopic investigations, such as for the formic acid

dimer<sup>[13]</sup> or 2PY · 2HPY, and theoretical work on the structures, energetics, and dynamics of DPT.<sup>[10-12,14]</sup> Also, DPT between amino acid base pairs is a possible source for spontaneous or radiation-induced mutations, especially for the guanine–cytosine pair,<sup>[15,16]</sup> since rare tautomers are formed in such a process.

### Computational Methods

#### *Construction and Fit of the Potential Energy Surfaces*

Since the hydrogen-bonding pattern in 2PY · 2HPY (see Fig. 1) consists of an N ··· HN and an OH ··· O motif the proton-transfer potentials in protonated water ( $\text{H}_2\text{O} \cdots \text{HOH}_2^+$ ) and protonated ammonia dimer ( $\text{H}_3\text{N} \cdots \text{HNH}_3^+$ ) are useful choices as the zeroth-order potentials. Three-dimensional potential energy functions were calculated using ab initio calculations at the MP2/6-311++G\*\* level. For ( $\text{H}_3\text{N} \cdots \text{HNH}_3^+$ ) the barrier height for proton transfer along the minimum energy path is 0.6 kcal mol<sup>-1</sup>, while for ( $\text{H}_2\text{O} \cdots \text{HOH}_2^+$ ) the minimum energy path has a single minimum (namely, no barrier). The PESs explicitly depend upon the heavy–heavy atom distance  $R$ , the distance  $r$  between the heavy atom and the transferring proton, and the angle  $\theta$  between the two (vectors  $\vec{R}$  and  $\vec{r}$  (see Fig. 1)). For each configuration characterized by  $(R, r, \theta)$  all remaining coordinates are relaxed, which leads to a fully-relaxed three-dimensional PES for both systems. The grid included intermolecular distances  $R$  between 2.4 and 3.4 Å in increments of 0.05 Å, while the bond length  $r$  varied between 0.8 Å to the midpoint between the two heavy atoms in increments of 0.05 Å. The angular dependence was calculated for the linear conformation (0°) and at angles  $\theta = 11.98^\circ, 27.49^\circ, 43.10^\circ, \text{ and } 58.73^\circ$ , respectively. These angles constitute a Legendre grid of period three, which allows for efficient fitting in terms of Legendre polynomials. A total of 675 points were calculated. All ab initio calculations were carried out using *Gaussian 98*.<sup>[17]</sup>

Since the calculations were done at Gauss–Legendre quadrature points it is possible to project out the radial strength functions for  $\lambda < 10$

$$V(R, r, \theta) = \sum_{\lambda=0}^n V_{\lambda}(R, r) \cdot P_{\lambda}(\cos \theta) \quad (1)$$

where  $P_{\lambda}(\cos \theta)$  are the corresponding Legendre polynomials.

Inspection of the radial strength functions led us to choose different functional forms for the  $V_i(R, r)$ . For  $V_0(R, r)$  the form is a double-well Morse potential to which a Gaussian function is added to optimally fit the barrier region. The final functional form for  $V_0(R, r)$  is then

$$V_0(R, r) = D_e(R)\{1 - \exp[-\beta_1(R)(r - r_e(R))]\}^2 + D_e(R)\{1 - \exp[-\beta_1(R)(1 - r - r_e(R))]\}^2 + c(R)\exp[-\beta_2(R)(r - 0.5)]^2 \quad (2)$$

The parameters  $D_e(R)$ ,  $\beta_1(R)$ ,  $\beta_2(R)$ ,  $r_e(R)$ , and  $c(R)$  in Eqn (2) are quadratic polynomials in  $R$ .

Since in the present case the angular excursions are limited due to the hydrogen-bonding network, no higher-order radial strength functions were required to describe the  $\theta$  dependence in full detail. However, it is worthwhile to mention that a satisfactory fit in three dimensions is possible on the entire interval  $\theta = [0^\circ, 180^\circ]$  if the functional form of  $V_i(R, r)$  for  $\lambda > 0$  is carefully chosen. Instead, we used a simple harmonic potential in  $\theta$  for the angular dependence. This is justified because ab initio calculations on 2PY · 2HPY confirmed that the potential energy varies quadratically as a function of  $\theta$  up to  $\approx 30^\circ$ . The complete function is then

$$V(R, r, \theta) = V_0(R, r) + k\theta^2 \quad (3)$$

which depends upon 16 free parameters. Eqn (3) is fitted to the ab initio data using I-NoLLS.<sup>[18]</sup> The fitting focussed on data points

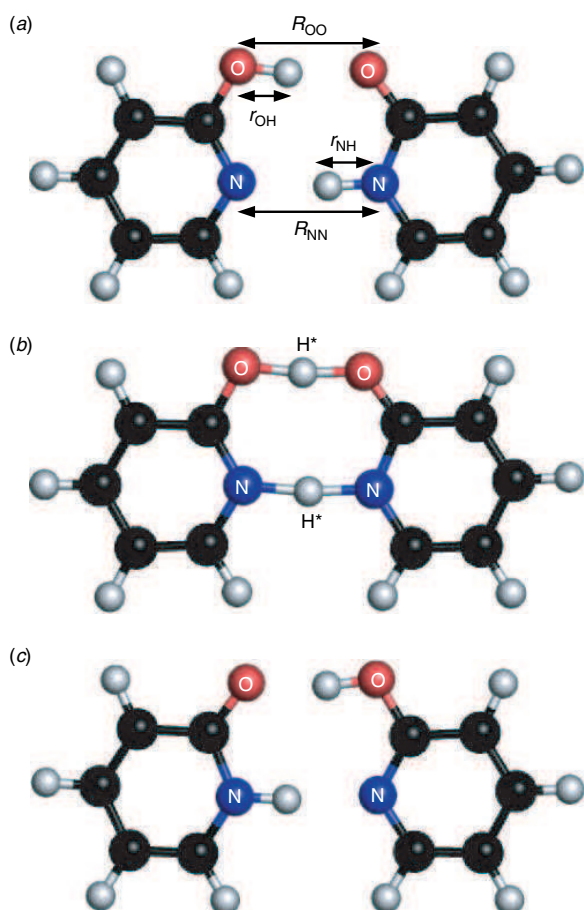


**Fig. 1.** (a) Reactant, (b) transition, and (c) product states of 2PY · 2HPY. The transferring protons are denoted  $H^*$ . The upper panel depicts the coordinates (introduced in the text) to describe the minimum structures and proton transfer process.  $R$  is the heavy-heavy interatomic distance and  $r$  the hydrogen-bond coordinate.

15 kcal mol<sup>-1</sup> above the minimum of each cut  $R = \text{const.}$ , and the potential parameters can be obtained from the authors upon request.

These zeroth-order potentials are constructed for the model systems  $(H_2O \cdots HOH_2)^+$  and  $(H_3N \cdots HNH_3)^+$ , respectively, and not for the hydrogen bonded network within 2PY · 2HPY. The main difference between the model potentials and the true DPT potential in 2PY · 2HPY is the height of the proton transfer barrier.<sup>[12]</sup> This quantity can be adjusted by scaling the isotropic part of the potential,  $V_0(R, r)$  which leads to the scaled potential

$$\tilde{V}(R, r, \theta) = \lambda V_0(R, r) + k\theta^2 \quad (4)$$

Such a procedure is a simplified version of the more general ‘morphing potential’ method.<sup>[6]</sup> It is worthwhile mentioning that potentials for  $O_2H_5^+$  exist in the literature.<sup>[19]</sup> This potential was constructed to describe an excess proton in water. The two PESs agree in that they both have a minimum energy structure where the proton is equally shared between the two water molecules. For  $R = 2.8 \text{ \AA}$  the barrier height for proton transfer is 7.8 kcal mol<sup>-1</sup> (see ref. [19]) compared to 8.2 kcal mol<sup>-1</sup> for our potential. However, for the present purpose it is mostly of importance that the zeroth order (MP2/6-311++G\*\*) potential describes the overall topology correctly. Once used within the ‘morphing’ the  $(O-H-O)^+$  potential loses its immediate relevance to protonated water dimer.

#### Implementation

We describe the proton transfer (PT) in terms of the dynamics of a hydrogen bond. This hydrogen bond is established by connecting donor (D), transferring hydrogen ( $H^*$ ), and acceptor (A) atoms through an additional potential energy term. When PT is completed, a new bonded state is reached which leads to new bonded energy terms due to establishing new angles and torsions on the acceptor side. These energy and force terms have to be switched on and off depending on the position of  $H^*$ .

The interaction between atoms forming a hydrogen bridge is calculated with the new potential  $V(R, r, \theta)$  while the other contributions to the total potential energy are treated with the CHARMM22 force field.<sup>[20]</sup> The force field including the proton transfer contribution is then

$$V(\vec{x}) = V_{MM}(\vec{x}) + V_{PT}(\vec{x}) \quad (5)$$

where  $V_{PT}(\vec{x}) = V_{OHO}(R_1, r_1, \theta_1) + V_{NHN}(R_2, r_2, \theta_2)$  and  $V_{MM}$  is the modified CHARMM22 force field and  $\vec{x}$  is a general configuration of the system. Care has to be taken in that certain terms in the classical force field have to be either turned off (such as the bonded donor- $H^*$  term) or smoothly switched on or off (such as angular terms  $X-D-H^*$  which only exist if the transferring proton is bonded to the side where the angle  $X-D-H^*$  exists). Also, the non-bonded interactions between  $H^*$  and A, and between A and D, are removed since we consider these to now form a bond. During the PT event we have to modify the contributions of several energy terms. This modification is achieved through a switching function  $s(R, r) = 1/2\{\tanh[\sigma(rR - \kappa(R))] + 1\}$  which gradually turns the terms on or off, respectively.

To complete the description of the energetics we discuss the effects on the angles, torsion, and improper dihedral terms. In the two limiting structures (shown in Fig. 1a and 1c) one full set of these terms exists, namely  $V_A(\vec{x})$  and  $V_C(\vec{x})$  for the upper and lower configuration in Fig. 1, respectively. In approaching the transition state (Fig. 1b) the two limiting structures are mixed according to  $V_A(\vec{x})s(R, r) + V_C(\vec{x})[1 - s(R, r)]$ . At the transition state, all modified energy terms contribute exactly half to the total potential. Table 1 summarizes the necessary changes in the calculation of the energies and forces to avoid double counting and correctly account for electrostatic and van der Waals interactions.

#### Molecular Dynamics Simulations

Molecular Dynamics (MD) simulations were used to investigate the PT dynamics and the possibility for DPT as a function of the barrier heights. All MD simulations were carried out with the modified force field (Eqn (5)) discussed in the previous section and implemented into

CHARMM.<sup>[21]</sup> The time step was 0.1 fs to properly account for the most rapid motions within the system. The system was heated to 300 K and equilibrated before dynamics runs in a microcanonical ensemble (constant energy). No external forces were applied to the system and dissociation was not observed although this would be possible with the modified force field. Non-bonded interactions were fully incorporated. Total simulation times in each case were 1 ns.

#### Unscaled and Scaled Potentials for Double Proton Transfer

To graphically represent the double proton transfer potential energy surface we introduce two coordinates. The coordinate  $\rho_1 = 1/2(R_{\text{NN}} + R_{\text{OO}})$  is defined as the average

**Table 1. A summary of all modified energy terms in CHARMM<sup>[21]</sup>**

D and A are donor and acceptor atoms, respectively. X and Y are bonded neighbouring atoms (carbon atoms in the present case)

Energy term	Affected atoms	Action	Potential function
H bond	D-H <sup>*</sup> ...A	add	$V_{\text{PT}}$
bond angle	D-H <sup>*</sup>	remove	$V_{\text{MM}}$
	X-D-H <sup>*</sup>	modify	$V_{\text{MM}} \times s(R, r)$
	X-A...H <sup>*</sup>	add	$V_{\text{MM}} \times s(R, r)$
dihedral	X-Y-D-H <sup>*</sup>	modify	$V_{\text{MM}} \times s(R, r)$
	X-Y-A...H <sup>*</sup>	add	$V_{\text{MM}} \times s(R, r)$
	X-D-Y-H <sup>*</sup>	modify	$V_{\text{MM}} \times s(R, r)$
improper	X-A-Y...H <sup>*</sup>	add	$V_{\text{MM}} \times s(R, r)$
	X-A-Y...H <sup>*</sup>	add	$V_{\text{MM}} \times s(R, r)$
non-bonded	H <sup>*</sup> ...A	remove	$V_{\text{MM}}$
	D...A	remove	$V_{\text{MM}}$
	X <sub>A</sub> bound...H <sup>*</sup>	modify	$V_{\text{MM}} \times s(R, r)$
	X <sub>D</sub> bound...H <sup>*</sup>	add	$V_{\text{MM}} \times s(R, r)$

of the intermolecular distances  $R$  of the N...N and O...O heavy interatomic distances.<sup>[12]</sup> The coordinate  $\rho_1 = 1/2(r_{\text{NH}} - r_{\text{NH,TS}} + r_{\text{OH}} - r_{\text{OH,TS}})$  describes the proton motions. It is defined with respect to the N-H and O-H bond length at the transition state structure,  $r_{\text{NH,TS}}$  and  $r_{\text{OH,TS}}$ . This leads to a symmetrical form where the transition state is located at  $\rho_2 = 0$ . In a similar fashion the projection of the trajectories on these potential landscapes are visualized by introducing the coordinates  $\sigma_1 = \rho_1$  and  $\sigma_2 = 1/2(r_{\text{NH}} + r_{\text{OH}})$ .

For each structure ( $\rho_1, \rho_2$ ) the total energy (Eqn (5)) is calculated on a grid of equally separated points by optimizing the remaining coordinates. The relaxed potential energy is calculated using the steepest descent method. Convergence was reached when the force gradient became smaller than  $10^{-4}$  kcal mol<sup>-1</sup> Å<sup>-1</sup>. A graphical representation of the relaxed potential energy surfaces for DPT using the unscaled ( $\lambda_{\text{OHO}} = 1.0, \lambda_{\text{NHN}} = 1.0$ ) potentials and the scaled potential energy function ( $\lambda_{\text{OHO}} = 5.0, \lambda_{\text{NHN}} = 5.0$ ) is shown in Fig. 2. By varying the scaling the barrier for DPT can be directly influenced.

For ( $\lambda_{\text{OHO}} = 1.0, \lambda_{\text{NHN}} = 1.0$ ) the barrier for DPT is 3.6 kcal mol<sup>-1</sup>. Although the zeroth order  $V_{\text{OHO}}$  potential has no barrier, steric factors and electrostatic interactions give rise to a barrier along this coordinate once  $V_{\text{OHO}}$  is used within the complete force field (Eqn (5)). This is evident from the correct minimum energy structure for 2PY·2HPY (see Fig. 1a). The heavy atom distances are  $R_{\text{OO}} = 2.46$  Å and  $R_{\text{NN}} = 2.70$  Å while the hydrogen bond

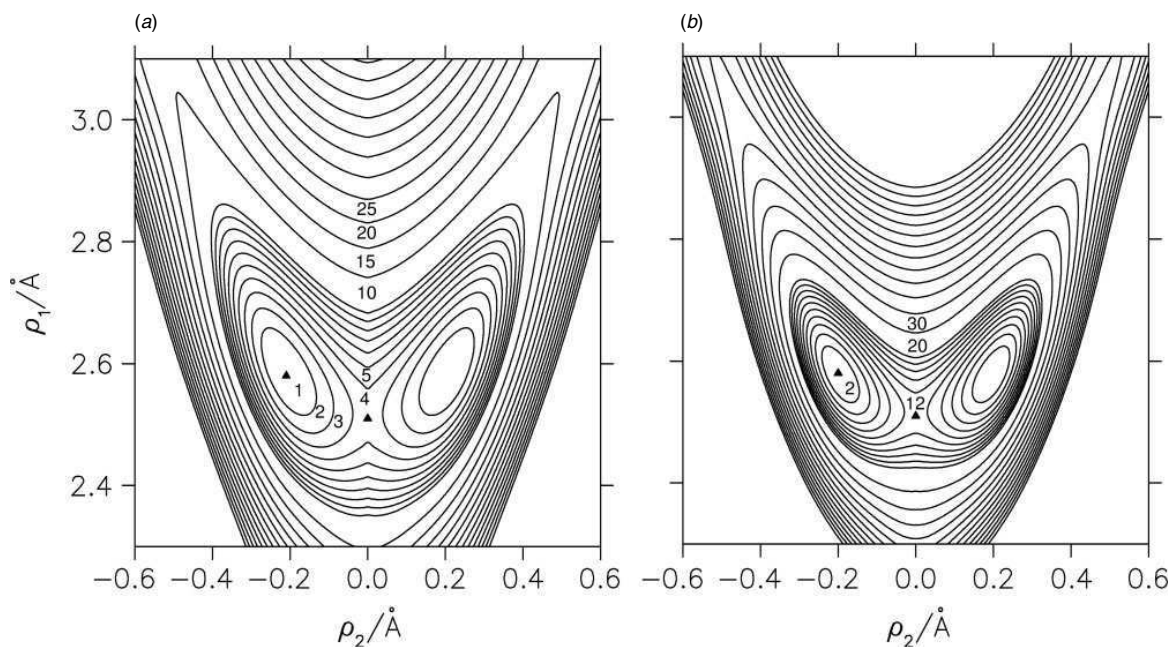


**Fig. 2.** (a) Relaxed potential energy surface for double proton transfer in 2PY·2HPY for ( $\lambda_{\text{OHO}} = 1.0, \lambda_{\text{NHN}} = 1.0$ ). The coordinates  $\rho_1$  (intermolecular distance) and  $\rho_2$  (proton motion) are defined in the text. Contours are drawn every 1 kcal mol<sup>-1</sup> for energies below 10 kcal mol<sup>-1</sup> and every 5 kcal mol<sup>-1</sup> above. The absolute minimum is at point ( $\rho_1 = 2.58, \rho_2 = -0.21$ ) and the transition state is located at ( $\rho_1 = 2.51, \rho_2 = 0.00$ ). Both points are marked by triangles. The resulting barrier height is 3.6 kcal mol<sup>-1</sup>. (b) As for (a) but for scaling factors ( $\lambda_{\text{OHO}} = 5.0, \lambda_{\text{NHN}} = 5.0$ ). Contours are drawn every 2 kcal mol<sup>-1</sup> below 20 kcal mol<sup>-1</sup> and every 10 kcal mol<sup>-1</sup> above. The resulting barrier height is 10.9 kcal mol<sup>-1</sup>.

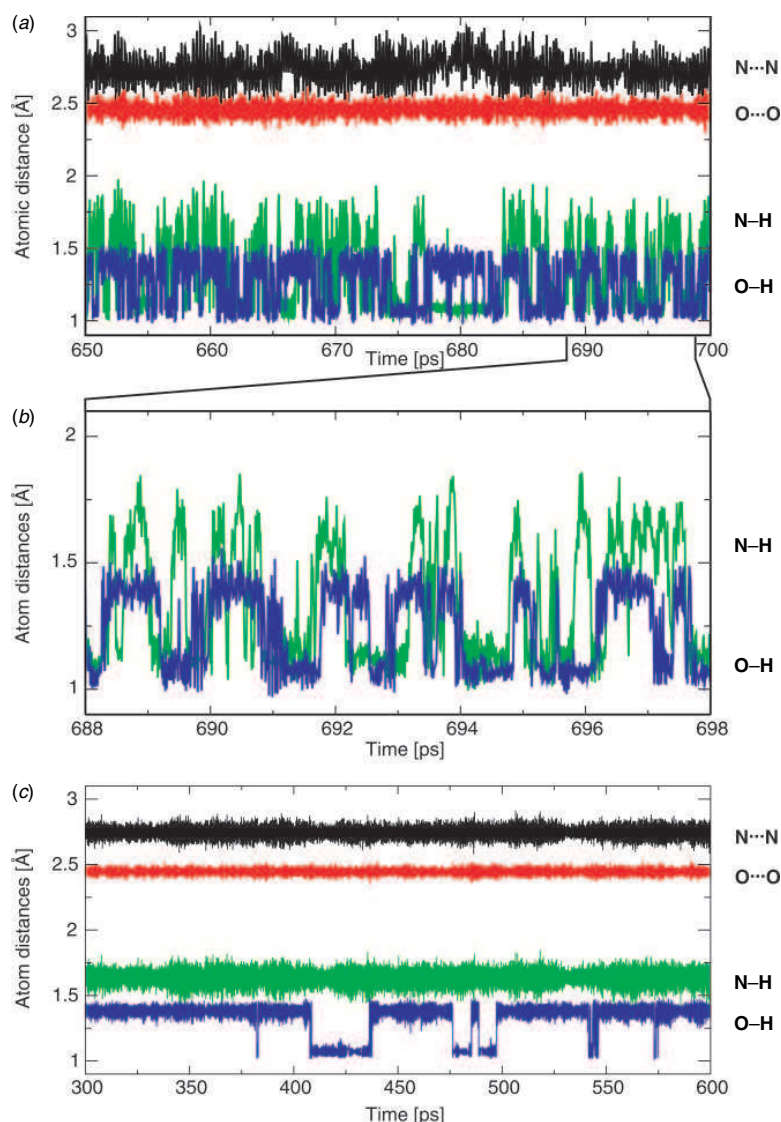


**Fig. 3.** (a) Atomic distance fluctuations on the surface with ( $\lambda_{\text{OHO}} = 1.0$ ,  $\lambda_{\text{NHN}} = 1.0$ ). A 50 ps sample from a 1 ns trajectory is shown. From top to bottom, the N...N, O...O, N-H, and O-H distances are displayed. Both hydrogen bonds are defined with respect to the initial bonding pattern. (b) Details from 10 ps of the same trajectory. In most cases the N-H and O-H are long and short at the same time. (c) As for (a) but for 300 ps dynamics on the scaled potential energy surface with ( $\lambda_{\text{OHO}} = 5.0$ ,  $\lambda_{\text{NHN}} = 5.0$ ). Since the barrier for PT along OHO is still low ( $4.8 \text{ kcal mol}^{-1}$ ) occasional transfers are observed.

lengths are  $r_{\text{OH}} = 1.05 \text{ \AA}$  and  $r_{\text{NH}} = 1.11 \text{ \AA}$ , respectively. The hydrogen bonds are not exactly linear but have angles of  $\theta_{\text{HOO}} = 6.9^\circ$  and  $\theta_{\text{HNN}} = 4.0^\circ$ , respectively. These data compare with  $R_{\text{OO}} = 2.64 \text{ \AA}$ ,  $R_{\text{NN}} = 2.87 \text{ \AA}$ ,  $r_{\text{OH}} = 1.00 \text{ \AA}$ , and  $r_{\text{NH}} = 1.04 \text{ \AA}$  and angles  $\theta_{\text{HOO}} = 5.7^\circ$  and  $\theta_{\text{HNN}} = 3.6^\circ$  from MP2/6-311++G\*\* calculations.<sup>[12]</sup>

The DPT barrier for the ( $\lambda_{\text{OHO}} = 5.0$ ,  $\lambda_{\text{NHN}} = 5.0$ ) scaled potential is  $10.9 \text{ kcal mol}^{-1}$ , close to the value from SCC-DFTB.<sup>[12]</sup> The minimum energy structure on this PES is characterized by  $R_{\text{OO}} = 2.45 \text{ \AA}$ ,  $R_{\text{NN}} = 2.74 \text{ \AA}$ ,  $r_{\text{OH}} = 1.06 \text{ \AA}$ , and  $r_{\text{NH}} = 1.11 \text{ \AA}$ , respectively. The hydrogen bond angles are slightly larger than before, namely  $\theta_{\text{HOO}} = 7.7^\circ$  and  $\theta_{\text{HNN}} = 4.4^\circ$ , respectively.

#### Nuclear Dynamics

MD simulations were run on the unscaled (zeroth-order) potential and a scaled potential (see Eqn (4)) with scaling ( $\lambda_{\text{OHO}} = 5.0$ ,  $\lambda_{\text{NHN}} = 5.0$ ) to demonstrate the effect of the energy scaling on PT dynamics. In all MD simulations the total energy is conserved to within  $10^{-3} \text{ kcal mol}^{-1}$ , which is typical for MD simulations. This establishes that the implementation of the energy terms and forces is correct.

The dynamics on the unscaled PES ( $\lambda_{\text{OHO}} = 1.0$ ,  $\lambda_{\text{NHN}} = 1.0$ ) with a barrier of  $3.6 \text{ kcal mol}^{-1}$  for DPT shows proton transfer events at irregular intervals (see Figs 3a and 4a for a projection of the dynamics onto the PES). After sufficient equilibration of the dynamics the PT events are mainly

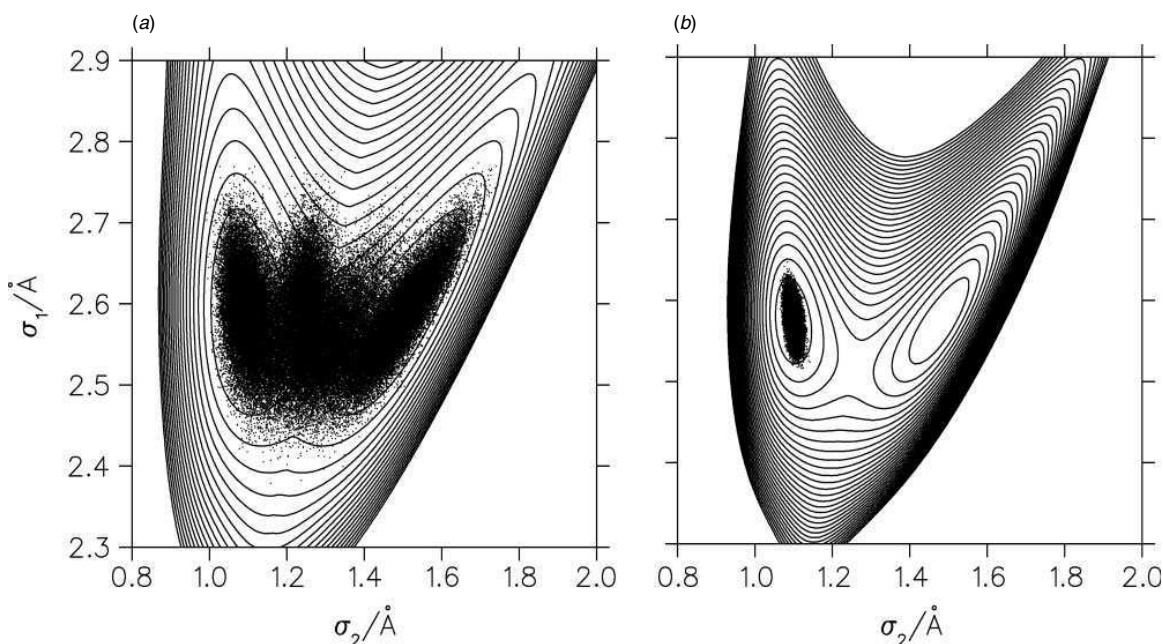


**Fig. 4.** (a) Projection of the trajectory run on the surface with ( $\lambda_{\text{OHO}} = 1.0$ ,  $\lambda_{\text{NHN}} = 1.0$ ). The coordinates  $\sigma_1$  (intermolecular distance) and  $\sigma_2$  (proton motion) are defined in the text. Contours are drawn every  $2 \text{ kcal mol}^{-1}$ . The proton transfers frequently between the two minima and samples the TS extensively. (b) As for (a) but on the scaled potential energy surface with scaling factors ( $\lambda_{\text{OHO}} = 10$ ,  $\lambda_{\text{NHN}} = 8$ ) and contours drawn every  $5 \text{ kcal mol}^{-1}$ . No proton transfers are observed.

correlated (the protons transfer synchronously<sup>[12]</sup>). This is shown in Fig. 3b where the N–H and O–H bonds are usually long and short at the same time. The barriers for proton transfer are sufficiently low to allow rapid exchange of the protons on a time scale of picoseconds, as found for example in  $\text{N}_2\text{H}_7^+$ .<sup>[22]</sup>

From previous ab initio MD simulations it is known that *spontaneous* PT at 300 K should be a rare event.<sup>[12]</sup> The reason for this is that the barrier for DPT is larger than the one for the unscaled potential discussed above. The barrier for DPT at different levels of theory was found to be between  $8.0 \text{ kcal mol}^{-1}$  (MP2/6–311++G\*\*) and  $11.5 \text{ kcal mol}^{-1}$  calculated with semiempirical density functional theory (DFT) methods.<sup>[12]</sup> Since the barrier for DPT for the unscaled potential is lower, it was of interest to carry out simulations for larger barrier heights. For this, the zeroth order potentials  $V_{\text{OHO}}(R, r, \theta)$  and  $V_{\text{NHN}}(R, r, \theta)$  in Eqn (4) were scaled with ( $\lambda_{\text{OHO}} = 5.0$ ,  $\lambda_{\text{NHN}} = 5.0$ ). As shown in Fig. 3c during the dynamics at 300 K, PT on this potential is a rare event. Only few transfers along the OHO motif and none along the NHN bond occur. The reason for the occasional transfer along the OHO coordinate is the still somewhat low barrier for PT along the OHO bond of  $4.8 \text{ kcal mol}^{-1}$  while the barrier along the NHN bond is  $5.7 \text{ kcal mol}^{-1}$ . However, a DPT barrier of around  $11 \text{ kcal mol}^{-1}$  can be achieved for different combinations of ( $\lambda_{\text{OHO}}$ ,  $\lambda_{\text{NHN}}$ ). These families of DPT potentials will have different barrier heights along the OHO and NHN pattern.

Increasing the scaling factor to ( $\lambda_{\text{OHO}} = 10.0$ ,  $\lambda_{\text{NHN}} = 8.0$ ) prevents all proton transfer events. The barrier for DPT in

this case is  $17.6 \text{ kcal mol}^{-1}$  and the minimum energy structure is essentially unchanged from the case for ( $\lambda_{\text{OHO}} = 5.0$ ,  $\lambda_{\text{NHN}} = 5.0$ ). Fig. 4b shows a projection of a trajectory calculated on this potential energy surface onto the ( $\sigma_1$ ,  $\sigma_2$ ) plane. The system is localized in one of the two possible tautomeric forms. This illustrates that depending upon the—experimental and/or theoretical—data available barriers for DPT can be scaled according to the requirements.

To conclude, in the present work the construction and use of dissociable force fields in classical MD simulations is discussed. The approach is based on high-quality zeroth-order PESs for proton transfer. These potentials can be adapted to the particular atomic and molecular environment by morphing the zeroth-order surfaces. ‘Morphing’ is most attractive in situations where experimental data on reaction barriers, vibrational frequencies, or equilibrium geometries are available. Since the aim was to establish a coherent methodology, the full range of possibilities was not explored in the present work. Rather, through comparison with a previously and thoroughly studied system, different applications of the method were discussed. Based on previous work<sup>[6–9]</sup> it is expected, however, that—sufficient and accurate experimental data provided—morphing will lead to highly improved PESs for a variety of systems involving PT.

It should be noted that for 2PY · 2HPY we were able to carry out the previous mixed QM/MM simulations<sup>[12]</sup> only for a few tens of picoseconds because of the considerable computational cost of semiempirical DFT compared to evaluating a force field. Thus, these previous simulations were not able to study effects such as ‘recurrence phenomena’

(recrossing after DPT) which are expected to occur on much longer time scales because of the relatively high barrier of 8–11 kcal mol<sup>-1</sup> for DPT. The main motivation to explore the present approach is to allow long-time simulations with extended sampling of the reactive region, which is out of reach for most biological systems using mixed QM/MM methods to date. In these previous simulations 10 ps of ab initio MD simulations for 2PY · 2HPY using a semiempirical DFT method<sup>[12]</sup> required 11 h of CPU time while 1 ns of nuclear dynamics with the present approach takes 5 min on the same computer.

#### Acknowledgments

The authors are supported by the Schweizerischer Nationalfonds. M.M. acknowledges financial support from the Schweizerischer Nationalfonds through a Förderungsprofessur.

#### References

- [1] M. Karplus, J. A. McCammon, *Nature Struct. Biol.* **2002**, *9*, 646. doi:10.1038/NSB0902-646
- [2] P. A. Bash, M. J. Field, M. Karplus, *J. Am. Chem. Soc.* **1987**, *109*, 8092.
- [3] Q. Cui, M. Elstner, E. Kaxiras, Th. Frauenheim, M. Karplus, *J. Phys. Chem. B* **2001**, *105*, 569. doi:10.1021/JP0029109
- [4] M. Karplus, Q. Cui, M. Elstner, *J. Phys. Chem. B* **2002**, *106*, 2721. doi:10.1021/JP013012V
- [5] A. Warshel, R. M. Weiss, *J. Am. Chem. Soc.* **1980**, *102*, 6218.
- [6] M. Meuwly, J. M. Hutson, *J. Chem. Phys.* **1999**, *110*, 8338. doi:10.1063/1.478744
- [7] A. A. Buchachenko, N. F. Stepanov, R. V. Krems, S. Nordholm, *Phys. Chem. Chem. Phys.* **2002**, *4*, 4992. doi:10.1039/B204480N
- [8] Z. Wang, R. R. Lucchese, J. W. Bevan, *J. Phys. Chem. A* **2004**, *108*, 2884. doi:10.1021/JP036603P
- [9] J. M. Bowman, S. S. Xantheas, *Pure Appl. Chem.* **2004**, *76*, 29.
- [10] A. Müller, F. Talbot, S. Leutwyler, *J. Chem. Phys.* **2001**, *115*, 5192. doi:10.1063/1.1394942
- [11] D. R. Borst, J. R. Roscioli, D. W. Pratt, G. M. Florio, T. S. Zwier, A. Müller, S. Leutwyler, *Chem. Phys.* **2002**, *283*, 341. doi:10.1016/S0301-0104(02)00598-0
- [12] M. Meuwly, A. Müller, S. Leutwyler, *Phys. Chem. Chem. Phys.* **2003**, *5*, 2663. doi:10.1039/B212732F
- [13] F. Madeja, M. Havenith, *J. Chem. Phys.* **2002**, *117*, 7162. doi:10.1063/1.1507581
- [14] Z. Smerdashina, W. Siebrand, A. Fernandez-Ramos, E. Martinez-Nunez, *Chem. Phys. Lett.* **2004**, *386*, 396. doi:10.1016/J.CPLETT.2004.01.061
- [15] M. Hutter, T. Clark, *J. Am. Chem. Soc.* **1996**, *118*, 7574. doi:10.1021/JA953370+
- [16] E. Nir, K. Kleiner, M. S. de Vries, *Nature* **2000**, *408*, 949. doi:10.1038/35050053
- [17] M. J. Frisch, G. W. Trucks, H. B. Schlegel, G. E. Scuseria, M. A. Robb, J. R. Cheeseman, V. G. Zakrzewski, J. A. Montgomery, Jr, R. E. Stratmann, et al., *Gaussian 98* (Gaussian, Inc.: Pittsburgh, PA).
- [18] M. M. Law, J. M. Hutson, *Comput. Phys. Commun.* **1997**, *102*, 252. doi:10.1016/S0010-4655(97)00013-1
- [19] L. Ojamäe, I. Shavitt, S. J. Singer, *J. Chem. Phys.* **1998**, *109*, 5547. doi:10.1063/1.477173
- [20] A. D. MacKerell, Jr, D. Bashford, M. Bellott, R. L. Dunbrack, Jr, J. D. Evanseck, M. J. Field, S. Fischer, J. Gao, et al., *J. Phys. Chem. B* **1998**, *102*, 3586. doi:10.1021/JP973084F
- [21] B. R. Brooks, R. E. Bruccoleri, B. D. Olafson, D. J. States, S. Swaminathan, M. Karplus, *J. Comp. Chem.* **1983**, *4*, 187.
- [22] M. Meuwly, M. Karplus, *J. Chem. Phys.* **2002**, *116*, 2572. doi:10.1063/1.1431285





## 5. Summary and Outlook

Within this thesis we presented the development of reactive force fields that are capable to describe the dynamics of proton and hydrogen atom transfer processes. The presented implementation in CHARMM overcomes the limitation that bond breaking and formation cannot be investigated by conventional classical MD simulations. Derived from high-level *ab initio* calculations this approach combines the accuracy of such calculations with the speed of MD simulations. The high-quality force fields of the prototype systems are comparable to high-level *ab initio* calculations in terms of structure and energy barriers. The PESs of proton transfer reactions are extremely sensitive with respect to the chemical environment. Nevertheless one is always able to classify the PT under investigation into symmetric and asymmetric PES. We developed a series of parameter sets that are not only able to describe symmetric and asymmetric correctly but also can accommodate to different locations of energetic minima and barriers. The chosen three-dimensional potential energy functions have shown to be quite flexible and transferable in characterizing PT reactions in quite diverse chemical systems. The morphing transformation of MMPT force field parameter, starting from one of our prototype systems to develop a new force field for a new molecular system which exhibits a similar topology in the PES along the proton reaction coordinates, has been shown to be successfully applicable in various examples. Energy scaling has been employed to investigate the effect on the proton transfer oscillation in  $\text{NH}_4^+ \cdots \text{NH}_3$ . New parameters through morphing have been developed for protonated diglyme, as well as for double proton transfer in 2PY2HP and for aspartic acid and water as model system for PT reactions in the active site of bacterial ferredoxin I. We applied the MMPT force field to investigate the vibrational infrared spectra of proton-bound species and explored the relationship of infrared spectra for protonated water dimer and protonated diglyme. The results for protonated water dimer compared well with other high-level calculations. Besides the further systematic development of the morphing approach one can also employ the force field in combination with Feynman path integral methods. The MMPT force field could be a

viable alternative to lower level quantum mechanical methods because the accuracy of the force field is only limited by the initial determination of the underlying PES for the PT of interest.

# Bibliography

1. K. R. Asmis, N. L. Pivonka, G. Santambrogio, M. Brümmer, C. Kaposta, D. M. Neumark, and L. Wöste. Gas-phase infrared spectrum of the protonated water dimer. *Science*, 299:1329–1330, 2003.
2. B. J. Alder and T. E. Wainwright. Phase transition for a hard sphere system. *J. Chem. Phys.*, 27(5):1208–1209, 1957.
3. B. J. Alder and T. E. Wainwright. Studies in molecular dynamics. I. General method. *J. Chem. Phys.*, 31(2):459–466, 1959.
4. J. B. Gibson, A. N. Goland, M. Milgram, and G. H. Vineyard. Dynamics of radiation damage. *Phys. Rev.*, 120(4):1229–1253, Nov 1960.
5. A. Rahman. Correlations in the motion of atoms in liquid argon. *Phys. Rev.*, 136(2A):A405–A411, 1964.
6. L. Verlet. Computer "experiments" on classical fluids. I. Thermodynamical properties of Lennard-Jones molecules. *Phys. Rev.*, 159(1):98, Jul 1967.
7. J. A. McCammon, B. R. Gelin, and M. Karplus. Dynamics of folded proteins. *Nature*, 267:585–590, 1977.
8. P. L. Freddolino, A. S. Arkhipova, S. B. Larson, A. McPherson, and K. Schulten. Molecular dynamics simulations of the complete satellite tobacco mosaic virus. *Structure*, 14(3):437–449, 2006.
9. B. R. Brooks, R. E. Bruccoleri, B. D. Olafson, D. J. States, S. Swaminathan, and M. Karplus. CHARMM: A program for macromolecular energy, minimization, and dynamics calculations. *J. Computational Chemistry*, 4(2):187 – 217, 1983.

10. S. J. Weiner, P. A. Kollman, D. A. Case, U. C. Singh, C. Ghio, G. Alagona, Jr. S. Profeta, and P. Weiner. A new force field for molecular mechanical simulation of nucleic acids and proteins. *J. Am. Chem. Soc.*, 106(3):765–784, 1984.
11. D. Van Der Spoel, E. Lindahl, B. Hess, G. Groenhof, A. E. Mark, and H. J. C. Berendsen. GROMACS: Fast, flexible, and free. *J. Comp. Chem.*, 26(16):1701–1718, 2005.
12. W. L. Jorgensen and J. Tirado-Rives. The OPLS force field for proteins. energy minimizations for crystals of cyclic peptides and crambin. *J. Am. Chem. Soc.*, 110(16):657–1666, 1988.
13. A. D. MacKerell, D. Bashford, M. Bellott, R. L. Dunbrack, J. D. Evanseck, M. J. Field, S. Fischer, J. Gao, H. Guo, S. Ha, D. Joseph-McCarthy, L. Kuchnir, K. Kuczeri, F. T. K. Lau, C. Mattos, S. Michnick, T. Ngo, D. T. Nguyen, B. Prodrom, W. E. III Reiher, B. Roux, M. Schlenkrich, J. C. Smith, R. Stote, J. Straub, M. Watanabe, J. Wiorkiewicz-Kuczera, D. Yin, and M. Karplus. All-atom empirical potential for molecular modeling and dynamics studies of proteins. *Journal of Physical Chemistry B*, 102:3586 – 3616, 1998.
14. A. Warshel and M. Levitt. Theoretical studies of enzymic reactions: Dielectric, electrostatic and steric stabilization of the carbonium ion in the reaction of lysozyme. *J. Mol. Biol.*, 103(2):227–249, 1976.
15. P. A. Bash, M. J. Field, and M. Karplus. Free energy perturbation method for chemical reactions in the condensed phase: a dynamic approach based on a combined quantum and molecular mechanics potential. *J. Am. Chem. Soc.*, 109(26):8092–8094, 1987.
16. J. Gao. Absolute free energy of solvation from monte carlo simulations using combined quantum and molecular mechanical potentials. *J. Phys. Chem.*, 96:537–540, 1992.
17. P. A. Bash, L. L. Ho, A. D. MacKerell, D. Levine, and P. Hallstrom. Progress toward chemical accuracy in the computer simulation of condensed phase reactions. *PNAS*, 93(8):3698–3703, 1996.
18. A. Warshel and R. M. Weiss. An empirical valence bond approach for comparing reactions in solutions and in enzymes. *J. Am. Chem. Soc.*, 102(20):6218–6226, 1980.

19. K. Hinsen and B. Roux. A potential function for computer simulation studies of proton transfer in acetylacetone. *J. Comp. Chem.*, 1998.
20. S. Braun-Sand, M. Strajbl, and A. Warshel. Studies of Proton Translocations in Biological Systems: Simulating Proton Transport in Carbonic Anhydrase by EVB-Based Models. *Biophys. J.*, 87(4):2221–2239, 2004.
21. P. Hohenberg and W. Kohn. Inhomogeneous electron gas. *Phys. Rev.*, 136(3B):864–871, 1964.
22. W. Kohn and L. J. Sham. Self-consistent equations including exchange and correlation effects. *Phys. Rev.*, 140(4A):A1133–A1138, 1965.
23. A. D. Becke. Density-functional thermochemistry. iii. the role of exact exchange. *J. Chem. Phys.*, 98(7):5648–5652, 1993.
24. C. Lee, W. Yang, and R. G. Parr. Development of the colle-salvetti correlation-energy formula into a functional of the electron density. *Phys. Rev. B*, 37(2):785–789, 1988.
25. M. Elstner, D. Porezag, G. Jungnickel, J. Elsner, M. Haugk, Th. Frauenheim, S. Suhai, and G. Seifert. Self-consistent-charge density-functional tight-binding method for simulations of complex materials properties. *Phys. Rev. B*, 58(11):7260–7268, 1998.
26. Q. Cui, M. Elstner, E. Kaxiras, T. Frauenheim, and M. Karplus. A QM/MM implementation of the self-consistent charge density functional tight binding (SCC-DFTB) method. *J. of Phys. Chem. B*, 105(2):569–585, 2001.
27. Q. Cui, M. Elstner, and M. Karplus. A theoretical analysis of the proton and hydride transfer in liver alcohol dehydrogenase (LADH). *J. of Phys. Chem. B*, 106(10):2721–2740, 2002.
28. M. Elstner. The SCC-DFTB method and its application to biological systems. *Theoret. Chem. Acc.*, 116(1-3):316–325, 2006.
29. X. Duan, S. Scheiner, and R. Wang. Modeling proton transfer potentials in angularly deformed hydrogen bonds. *Int. J. Quant. Chem.*, 48(S20):77–87, 1993.

30. S. Scheiner and X. Duan. Search for analytical functions to simulate proton transfers in hydrogen bonds. In *Modeling the hydrogen bond*, ACS Symposium Series, pages 125–138, 1994.
31. A.C.T. van Duin, S. Dasgupta, F. Lorant, and W.A. Goddard. ReaxFF: A reactive force field for hydrocarbons. *J. Phys. Chem. A*, 105:9396–9409, 2001.
32. M. Meuwly and J. M. Hutson. Morphing ab initio potentials: A systematic study of Ne-HF. *J. Chem. Phys.*, 110(17):8338–8347, 1999.
33. J. M. Bowman and S. S. Xantheas. Morphing of ab initio-based interaction potentials to spectroscopic accuracy: Application to Cl-(H<sub>2</sub>O). *Pure Appl. Chem.*, 76:29, 2004.
34. S. Scheiner. Theoretical studies of proton transfers. *Acc. Chem. Res.*, 18(6):174–180, 1985.
35. C Møller and M. S. Plesset. Note on an Approximation Treatment for Many-Electron Systems. *Phys. Rev.*, 46:618–622, 1934.
36. R. Krishnan, J. S. Binkley, R. Seeger, and J. A. Pople. Self-consistent molecular orbital methods. XX. A basis set for correlated wave functions. *J. Chem. Phys.*, 72(1):650–654, 1980.
37. T. Clark, J. Chandrasekhar, G. W. Spitznagel, and P. v. R. Schleyer. Efficient diffuse function-augmented basis sets for anion calculations. III. The 3-21+G basis set for first-row elements, Li-F. *J. Comp. Chem.*, 4(3):294–301, 1983.
38. I. Shavitt. The method of configuration interaction. In *Methods of Electronic Structure Theory*, pages 189–275, 1977.
39. J. A. Pople, R. Krishnan, H. B. Schlegel, and J. S. Binkley. Electron correlation theories and their application to the study of simple reaction potential surfaces. *Int. J. Quant. Chem.*, 14:545, 1978.
40. M. J. Frisch, G. W. Trucks, H. B. Schlegel, G. E. Scuseria, M. A. Robb, J. R. Cheeseman, J. A. Montgomery, Jr., T. Vreven, K. N. Kudin, J. C. Burant, J. M. Millam, S. S. Iyengar, J. Tomasi, V. Barone, B. Mennucci, M. Cossi, G. Scalmani, N. Rega, G. A. Petersson, H. Nakatsuji, M. Hada, M. Ehara, K. Toyota, R. Fukuda, J. Hasegawa, M. Ishida, T. Nakajima, Y. Honda, O. Kitao, H. Nakai,

- M. Klene, X. Li, J. E. Knox, H. P. Hratchian, J. B. Cross, V. Bakken, C. Adamo, J. Jaramillo, R. Gomperts, R. E. Stratmann, O. Yazyev, A. J. Austin, R. Cammi, C. Pomelli, J. W. Ochterski, P. Y. Ayala, K. Morokuma, G. A. Voth, P. Salvador, J. J. Dannenberg, V. G. Zakrzewski, S. Dapprich, A. D. Daniels, M. C. Strain, O. Farkas, D. K. Malick, A. D. Rabuck, K. Raghavachari, J. B. Foresman, J. V. Ortiz, Q. Cui, A. G. Baboul, S. Clifford, J. Cioslowski, B. B. Stefanov, G. Liu, A. Liashenko, P. Piskorz, I. Komaromi, R. L. Martin, D. J. Fox, T. Keith, M. A. Al-Laham, C. Y. Peng, A. Nanayakkara, M. Challacombe, P. M. W. Gill, B. Johnson, W. Chen, M. W. Wong, C. Gonzalez, and J. A. Pople. *Gaussian 03, Revision C.01*. Gaussian and Inc., Pittsburgh PA, 2004.
41. L. Jaroszewski, B. Lesyng, and J. A. McCammon. Ab initio potential energy functions for proton transfer in  $[\text{H}_3\text{N}-\text{H}-\text{NH}_3]^+$  and  $[\text{H}_3\text{N}-\text{H}-\text{OH}_2]^+$ . *J. Mol. Struct.*, 283:57–62, 1993.
42. X. Duan and S. Scheiner. Analytic functions fit to proton transfer potentials. *J. Mol. Struct.*, 270:173–185, 1992.
43. J. M. Price, M. W. Crofton, and Y. T. Lee. Observation of internal rotation in the  $\text{NH}_4^+(\text{NH}_3)_4$  ionic cluster. *J. Phys. Chem.*, 91(4):2749–2751, 1989.
44. J. M. Price, M. W. Crofton, and Y. T. Lee. Vibrational spectroscopy of the ammoniated ammonium ions  $\text{NH}_4^+(\text{NH}_3)_n$  ( $n = 1-10$ ). *J. Phys. Chem.*, 95(6):2182–2195, 1991.
45. S. Hamon, T. Speck, J. B. A. Mitchell, B. R. Rowe, and J. Troe. Experimental and theoretical study of the ion–molecule association reaction  $\text{NH}_4^+ + \text{NH}_3(+\text{M}) \rightarrow \text{N}_2\text{H}_7^+(+\text{M})$ . *J. Chem. Phys.*, 117(6):2557–2567, 2002.
46. P. Merlet, S. D. Peyerimhoff, and R. J. Buenker. Ab initio study of the hydrogen bond in  $[\text{H}_3\text{N}-\text{N}-\text{NH}_3]^+$ . *J. Am. Chem. Soc.*, 94(24):8301–8308, 1972.
47. J. A. Platts and K. E. Laidig. A theoretical study of the proton-bound ammonia dimer. *J. Phys. Chem.*, 99(17):6487–6492., 1995.
48. J. A. Platts and K. E. Laidig. Proton transfer in ionic hydrogen bonds. *J. Phys. Chem.*, 100(32):13455–13461, 1996.

49. T. Asada, H. Haraguchi, and K. Kitaura. Simulation studies of proton transfer in  $\text{N}_2\text{H}_7^+$  cluster by classical *ab initio* Monte Carlo and quantum wave packet dynamics. *J. Phys. Chem. A*, 105(31):7423–7428, 2001.
50. G.-S. Li, M. T. C. Martins Costa, C. Millot, and M. F. Ruiz-López. Effect of solvent fluctuations on proton transfer dynamics: a hybrid am1/mm molecular dynamics simulation on the  $[\text{H}_3\text{N}-\text{N}-\text{NH}_3]^+$ . *Chem. Phys.*, 240(1-2):93–99, 1999.
51. Y. Wang and J. R. Gunn. Computational study of structures and proton transfer in hydrogen-bonded ammonia complexes using semiempirical valence-bond approach. *Int. J. Quant. Chem.*, 73(4):357 – 367, 1999.
52. M. Meuwly and M. Karplus. Simulation of proton transfer along ammonia wires: An "ab initio" and semiempirical density functional comparison of potentials and classical molecular dynamics. *J. Chem. Phys.*, 116(6):2572–2585, 2002.
53. V. Zoete and M. Meuwly. On the influence of semirigid environments on proton transfer along molecular chains. *J. Chem. Phys.*, 120(15):7085–7094, 2004.
54. A. Fouqueau and M. Meuwly. Structures and dynamics of protonated ammonia clusters. *J Chem Phys.*, 123(24):244308, 2005.
55. E. Helfang. Brownian dynamics study of transitions in a polymer chain of bistable oscillators. *J. Chem. Phys.*, 69(3):1010–1018, 1978.
56. A. Müller, F. Talbot, and S. Leutwyler. Intermolecular vibrations of jet-cooled (2-pyridone)<sub>2</sub>: A model for the uracil dimer. *J. Chem. Phys.*, 112(8):3717–3725, 2000.
57. A. Müller, F. Talbot, and S. Leutwyler. Intermolecular vibrations of the jet-cooled 2-pyridone · 2-hydroxypyridine mixed dimer, a model for tautomeric nucleic acid base pairs. *J. Chem. Phys.*, 115(11):5192–5202, 2001.
58. D.R. Borst, J.R. Roscioli, and D.W. Pratt. High-resolution electronic spectra of 2-hydroxy and 2-aminopyridine. Perturbing effects of the nitrogen atom in the aromatic ring. *J. Phys. Chem. A*, 106(16):4022–4027, 2002.
59. D. R. Borst, J. R. Roscioli, D. W. Pratt, G. M. Florio, T. S. Zwier, A. Müller, and S. Leutwyler. Hydrogen bonding and tunneling in the 2-pyridone·2-hydroxypyridine dimer. Effect of electronic excitation. *Chem. Phys.*, 283(1-2):341–354, 2002.



60. M. J. Scanlan and I. H. Hillier. On the mechanism of proton transfer in the 2-hydroxypyridine  $\rightleftharpoons$  2-pyridone tautomeric equilibrium. *Chem. Phys. Lett.*, 107:330–332, 1984.
61. M. Meuwly, A. Müller, and S. Leutwyler. Energetics, dynamics and infrared spectra of the DNA base-pair analogue 2-pyridone · 2-hydroxypyridine. *Phys. Chem. Chem. Phys.*, 5(12):2663–2672, 2003.
62. A. Fernández-Ramos Z. Smedarchina, W. Siebrand and E. Martínez-Núñez. New interpretation of ground- and excited-state tunneling splitting in 2-pyridone · 2-hydroxypyridine. *Chem. Phys. Lett.*, 386(4-6):396–402, 2004.
63. Q.-S. Li, W.-H. Fang, and J.-G. Yu. Theoretical studies of proton-transfer reactions of 2-hydroxypyridine-(H<sub>2</sub>O)<sub>n</sub> ( $n = 0 - 2$ ) in the ground and excited states. *J. Phys. Chem. A*, 109(17):3983–3990, 2005.
64. M. Meuwly and M. Karplus. Theoretical investigations of Ferredoxin I: The possible role of internal water molecules on the coupled electron proton transfer reaction. *Faraday Discuss*, 124:297–313, 2003.
65. M. Meuwly and M. Karplus. Theoretical investigations on *Azotobacter vinelandii* ferredoxin I: Effects of electron transfer on protein dynamics. *Biophys. J.*, 86(4):1987–2007, 2004.
66. B. Shen, L. L. Martin, J. N. Butt, F. A. Armstrong, C. D. Stout, G. M. Jensen, P. J. Stephens, G. N. La Mar, C. M. Gorst, and B. K. Burgess. *Azotobacter vinelandii* ferredoxin I. Aspartate 15 facilitates proton transfer to the reduced [3Fe-4S] cluster. *J. Biol. Chem.*, 268(34):25928–25939, 1993.
67. K. Chen, J. Hirst, R. Camba, C. A. Bonagura, C. D. Stout, B. K. Burgess, and F. A. Armstrong. Atomically defined mechanism for proton transfer to a buried redox centre in a protein. *Nature*, 405(6788):814–817, 2000.
68. Dmitry A. Cherepanov and Armen Y. Mulkidjanian. Proton transfer in *azotobacter vinelandii* ferredoxin I: entatic Lys84 operates as elastic counterbalance for the proton-carrying Asp15. *Biochim. Biophys. Acta*, 1505(2-3):179–18, 2001.
69. R. Camba, Y.-S. Jung, L.M. Hunsicker-Wang, B.K. Burgess, C.D. Stout, J. Hirst, and F.A. Armstrong. Mechanisms of redox-coupled proton transfer in proteins:

- Role of the proximal proline in reactions of the [3Fe-4S] cluster in azotobacter vinelandii ferredoxin I. *Biochemistry*, 42(36):10589–10599, 2003.
70. R. Rajamani, K. J. Naidoo, and J. Gao. Implementation of an adaptive umbrella sampling method for the calculation of multidimensional potential of mean force of chemical reactions in solution. *J. Comp. Chem.*, 24:1775–1781, 2003.
71. E. Wigner. On the quantum correction for thermodynamic equilibrium. *Phys. Rev.*, 40(5):749–759, 1932.
72. C. J. T. de Grotthuss. Sur la décomposition de l'eau et des corps qu'elle tient en dissolution à l'aide de l'électricité galvanique. *Ann. Chim.*, 58:54–73, 1806.
73. M. Eigen. Proton transfer, acid-base catalysis and enzymatic hydrolysis. *Angew. Chem. Int. Eng.*, 3:1–19, 1964.
74. D. W. Pratt. High resolution spectroscopy in the gas phase: Even large molecules have well-defined shapes. *Ann. Rev. Phys. Chem.*, 49(1):481–530, 1998.
75. D. E. Folmer, E. S. Wisniewski, S. M. Hurley, and Jr. A. W. Castleman. Femtosecond cluster studies of the solvated 7-azaindole excited state double-proton transfer. *PNAS*, 96:12980–12986, 1999.
76. A. Bach and S. Leutwyler. Proton transfer in 7-hydroxyquinoline (NH<sub>3</sub>)<sub>n</sub> solvent clusters. *J. Chem. Phys.*, 112:560–565, 2000.
77. T. D. Fridgen, G. B. McMahon, L. MacAleese, J. Lemaire, and P. Maitre. Infrared spectrum of the protonated water dimer in the gas phase. *J. Phys. Chem.*, 108:9008, 2004.
78. D. T. Moore, J. Oomens, L. van der Meer, G. von Helden, G. Meijer, J. Valle, A. G. Marshall, and J. R. Eyler. Probing the vibrations of shared, OH+O-bound protons in the gas phase. *ChemPhysChem*, 5(5):740–743, 2004.
79. N. I. Hammer, E. G. Diken, J. R. Roscioli, M. A. Johnson, E. M. Myshakin, K. D. Jordan, A. B. McCoy, X. Huang, J. M. Bowman, and S. Carter. The vibrational predissociation spectra of the  $\text{H}_5\text{O}_2^+$  · RG<sub>n</sub> (RG = Ar, Ne) clusters: Correlation of the solvent perturbations in the free OH and shared proton transitions of the Zundel ion. *J. Chem. Phys.*, 122(24):244301, 2005.

80. H.-H. Bueker, T. Helgaker, K. Ruud, and E. Uggerud. Energetics and dynamics of intermolecular proton-transfer processes. 2. Ab initio direct dynamics calculations of the reaction  $\text{H}_3\text{O}^+ + \text{NH}_3 \rightarrow \text{NH}_4^+ + \text{H}_2\text{O}$ . *J. Phys. Chem.*, 100(38):15388–15392, 1996.
81. D. Wei and D. R. Salahub. Hydrated proton clusters: Ab initio molecular dynamics simulation and simulated annealing. *1997*, 106(14):6086–6094, 1997.
82. D. E. Sagnella and M. E. Tuckerman. An empirical valence bond model for proton transfer in water. *J. Chem. Phys.*, 108(5):2073–2083, 1998.
83. R. Vuilleumier and D. Borgis. Transport and spectroscopy of the hydrated proton: A molecular dynamics study. *J. Chem. Phys.*, 111(9):4251–4266, 1999.
84. M. V. Vener, O. Kühn, and J. Sauer. The infrared spectrum of the  $\text{O} \cdots \text{H} \cdots \text{O}$  fragment of  $\text{H}_5\text{O}_2^+$ : Ab initio classical molecular dynamics and quantum 4D model calculations. *J. Chem. Phys.*, 114(1):240–249, 2001.
85. N. Agmon. The grotthuss mechanism. *Chem. Phys. Lett.*, 244(5-6):456–462, 1995.
86. R. Pomes and B. Roux. Theoretical study of  $\text{H}^+$  translocation along a model proton wire. *J. Phys. Chem.*, 100(7):2519–2527, 1996.
87. H.-P. Chen. The motion of protons in water-ammonia clusters. *J. Chem. Phys.*, 105(14):6844–6855, 1996.
88. T. J. F. Day, U. W. Schmitt, and G. A. Voth. The mechanism of hydrated proton transport in water. *JACS*, 122(48):12027–12028, 2000.
89. P. L. Geissler, C. Dellago, D. Chandler, J. Hutter, and M. Parrinello. Ab initio analysis of proton transfer dynamics in  $(\text{H}_2\text{O})_3\text{H}^+$ . *Chem. Phys. Lett.*, 321(3-4):225–230, 2000.
90. M. Meuwly and M. Karplus. Simulation of proton transfer along ammonia wires: An ab initio and semiempirical density functional comparison of potentials and classical molecular dynamics. *J. Chem. Phys.*, 116(6):2572–2585, 2002.
91. J. Dai, Z. Bacic, X. Huang, S. Carter, and J. M. Bowman. A theoretical study of vibrational mode coupling in  $\text{H}_5\text{O}_2^+$ . *J. Chem. Phys.*, 119(13):6571–6580, 2003.

92. A. Fouqueau and M. Meuwly. Structures and dynamics of protonated ammonia clusters. *J. Chem. Phys.*, 123:244308, 2005.
93. M. Kaledin, A. L. Kaledin, and J. M. Bowman. Vibrational analysis of the  $\text{H}_5\text{O}_2^+$  infrared spectrum using molecular and driven molecular dynamics. *J. Phys. Chem. A.*, 110(9):2933–2939, 2006.
94. H. S. Mei, M. E. Tuckerman, D. E. Sagnella, and M. L. Klein. Quantum nuclear ab initio molecular dynamics study of water wires. *J. Phys. Chem. B.*, 102(50):10446–1045, 1998.
95. Y. Liu and M.E. Tuckerman. Protonic defects in hydrogen bonded liquids: Structure and dynamics in ammonia and comparison with water. *J. Phys. Chem. B.*, 105(28):6598–6610, 2001.
96. O. Chen, S. Groh, A. Liechty, and D. P. Ridge. Binding of nitric oxide to iron(II) porphyrins: Radiative association, blackbody infrared radiative dissociation, and gas-phase association equilibrium. *J. Am. Chem. Soc.*, 121(50):11910–11911, 1999.
97. J. L. and G. A. Voth. The quantum dynamics of an excess proton in water. *J. Chem. Phys.*, 104(5):2056–2069, 1996.
98. H. M. Cho and S. J. Singer. Correlation function quantum Monte Carlo study of the excited vibrational states of  $\text{H}_5\text{O}_2^+$ . *J. Phys. Chem. A*, 108(41):8691–8702, 2004.
99. J. Sauer and J. Döbler. Gas-phase infrared spectrum of the protonated water dimer: Molecular dynamics simulation and accuracy of the potential energy surface. *ChemPhysChem*, 6(9):1706 – 1710, 2005.
100. H.-P. Cheng and J. L. Krause. The dynamics of proton transfer in  $\text{H}_5\text{O}_2^+$ . *J. Chem. Phys.*, 107(20):8461–8468, 1997.
101. J. M. Hutson. Intermolecular forces from the spectroscopy of van der Waals molecules. *Ann. Rev. Phys. Chem.*, 41:123–154, 1990.
102. G. Alagona, C. Guio, and P. A. Kollman. Simple model for the effect of Glu165 -> Asp165 mutation on the rate of catalysis in triose phosphate isomerase. *J. Mol. Biol.*, 191(1):23–27, 1986.

103. M. J. Field, P. A. Bash, and M. Karplus. A combined quantum mechanical and molecular mechanical potential for molecular dynamics simulations. *J. Comput. Chem.*, 11(6):700–733, 1990.
104. P. Grochowski, B. Lesyng, P. Bala, and J. A. McCammon. Density functional based parametrization of a valence bond method and its applications in quantum-classical molecular dynamics simulations of enzymatic reactions. *Int. J. Quant. Chem.*, 60(6):1143–1164, 1996.
105. Z. Wang, A. L. McIntosh, B. A. McElmurry, J. R. Walton, R. R. Lucchese, and J. W. Bevan. Improved morphed potentials for Ar-HBr including scaling to the experimentally determined dissociation energy. *J. Phys. Chem. A*, 109(36):8168–8179, 2005.
106. K. J. Higgins and W. Klemperer. Structure and energy difference of two isomers of He-CH<sub>3</sub>F. *J. Chem. Phys.*, 122:244309, 2005.
107. M. M. Law and J. M. Hutson. I-nolls: A program for interactive nonlinear least-squares fitting of the parameters of physical models. *Comput. Phys. Comm.*, 102(1-3):252–268, 1997.
108. S. Lammers and M. Meuwly. Double proton transfer using dissociable force fields. *Aust. J. Chem.*, 57(12):1223–1228, 2004.
109. F. J. Harris. On the use of windows for harmonic analysis with the discrete Fourier transform. *Proc. IEEE*, 66(1):51–83, 1978.
110. M. Schmitz and P. Tavan. Vibrational spectra from atomic fluctuations in dynamics simulations. I. Theory, limitations, and a sample application. *J. Chem. Phys.*, 121(24):2233–2246, 2004.
111. M. Schmitz and P. Tavan. Vibrational spectra from atomic fluctuations in dynamics simulations. II. Solvent-induced frequency fluctuations at femtosecond time resolution. *J. Chem. Phys.*, 121(24):12247–12258, 2004.
112. A. E. Reed, R. B. Weinstock, and F. Weinhold. Natural population analysis. *J. Chem. Phys.*, 83(2):735–746, 1985.
113. S. Huang, B. J. Braams, and J. M. Bowman. Ab initio potential energy and dipole moment surfaces for H<sub>5</sub>O<sub>2</sub><sup>+</sup>. *J. Chem. Phys.*, 122:044308, 2005.

114. L. Ojamäe, I. Shavitt, and S. J. Singer. Potential energy surfaces and vibrational spectra of  $\text{H}_5\text{O}_2^+$  and larger hydrated proton complexes. *Int. J. Quant. Chem.*, 56(29):657 – 668, 1995.
115. E. F. Valeev and H. F. Schaefer III. The protonated water dimer: Brueckner methods remove the spurious  $C_1$  symmetry minimum. *J. Chem. Phys.*, 108(17):7197–7201, 1998.
116. M. Meuwly. The potential energy surface and rovibrational states of  $\text{He-HCO}^+$ . *J. Chem. Phys.*, 110(9):4347–4353, 1999.
117. O. Dopfer, R. V. Olkhov, and J. P. Maier. Microsolvation of  $\text{HN}_2^+$  in argon: Infrared spectra and ab initio calculations of  $\text{Ar}_n\text{-HN}_2^+$  ( $n = 1\text{-}13$ ). *J. Phys. Chem. A*, 103(16):2982–2991, 1999.
118. F. Tinti G. Buffa, L. Dore and M. Meuwly. New experimental and theoretical results for argon broadening and shift of  $\text{HCO}^+$  rotational lines. *ChemPhysChem*, 7(10):1764–1769, 2006.
119. B. Gazdy and J. M. Bowman. An adjusted global potential surface for HCN based on rigorous vibrational calculations. *J. Chem. Phys.*, 95(9):6309–6316, 1991.
120. Y.-S. Wang, H.-C. Chang, J.-C. Jiang, S. H. Lin, Y. T. Lee, and H.-C. Chang. Structures and isomeric transitions of  $\text{NH}_4^+(\text{H}_2\text{O})_{3-6}$ : From single to double rings. *J. Am. Chem. Soc.*, 120(34):8777–8788, 1998.
121. J.-W. Shin, N. I. Hammer, E. G. Diken, T. D. Jaeger M. A. Johnson and R. S. Walters, M. A. Duncan, R. A. Christie, and K. D. Jordan. Infrared signature of structures associated with the  $\text{H}^+(\text{H}_2\text{O})_n$  ( $n = 6$  to  $27$ ) clusters. *Science*, 304:1137–1140, 2004.
122. J. M. M. Howson and J. M. Hutson. Morphing the  $\text{He-OCS}$  intermolecular potential. *J. Chem. Phys.*, 115(11):5059–5065, 2001.

# A. Instructions for Use of CHARMM and MMPT

## A.1. Compilation

The subroutine `usersb.src` of the CHARMM program includes all MMPT routines. This subroutine has been written to allow users to directly interface with the core routines without having to modify the source code of the main program. The compilation of the MD program including the MMPT user routine follows the standard CHARMM installation protocol and can be invoked by including the install switch MMPT when calling the compilation script. The script has been adapted to compile with the file `usersb_mmpt.src` and the variable declaration file `mmpt.fcm` when the install switch MMPT is set. A typical example for the install command under a linux environment would be

```
./install.com gnu medium MMPT
```

For a full description of all possible options and switches see the documentation of the script supplied with the program. The executable program is called `charmm_mmpt` and stored in the directory `/c28a2/exec/gnu/`.

File name	Description
<code>usersb_mmpt.src</code>	User defined routine for MMPT reaction dynamics
<code>mmpt.fcm</code>	Variable declarations for <code>usersb_mmpt.src</code>

Table A.1: Summary of necessary files for compilation of CHARMM with MMPT.

## A.2. Usage

Usually the CHARMM commands are put in file and then submitted to the program in batch mode, where the commands are executed sequentially. We expect some familiarity in writing standard CHARMM input files and refer the reader for a complete description of available commands to the documentation supplied with the program as well as to the CHARMM publications. Typical examples of common CHARMM input files, like structure optimization, energy calculation, dynamics and trajectory analysis are available with the program and all commands concerning the energy calculation will include the MMPT energy and force contribution when the `USER` command is used. Important initial steps for a setting up a MMPT calculation consist of reading necessary information from MMPT specific files. They do not need to be given in any particular order but must be assigned to FORTRAN unit identifiers before the `USER` command is issued. The following files need to be assigned an unit identifier and have read access enabled. One or several MMPT parameter files depending on the number and type of hydrogen bridges. A file holding the number of hydrogen bridges and the number of atoms forming the bridge as they appear in the protein structure file. Certain newly formed bonded or non-bonded interaction on the acceptor side might demand user defined parameter because their are not present in the standard CHARMM parameter files. If the MMPT routine does not finds suitable parameter in the present molecule or protein the parameter need to be given in an additional file by the user. The necessary additional files are summarized in table A.2.

A possible usage of the `OPEN` command would look like the following lines.

```
OPEN UNIT 11 FORMATTED READ NAME MMPTNHO.PRM
OPEN UNIT 12 FORMATTED READ NAME HBRIDGE.DEF
OPEN UNIT 13 FORMATTED READ NAME HBRIDGE.PRM
```

The specified unit identifiers are then passed together with the appropriate keyword to the `USER MMPT` command. An example command line expression would be

```
USER MMPT NHOUNIT 11 HBRDUNIT 12 HPRMUNIT 13 SCLNHO 1.0,
```

which calls the MMPT initialization routine that reads the previously specified files, sets up bookkeeping tables of affected energy terms and tells the CHARMM main



File	Content	Keyword
MMPT parameter	contains all parameter for proton transfer reaction, parameters are stored one per line	NHOUNIT, NHNUNIT, OHOUNIT
Hydrogen bridge atom definitions	lists all atom numbers forming a hydrogen bridge, atom numbers correspond to numbering in protein structure file.	HBRDUNIT
Extra parameter	contains bond, angle, and dihedral as well as nonbonded parameter for new interactions on acceptor side, format follows CHARMM parameter files.	HPRMUNIT

Table A.2: Summary of MMPT specific files holding additional information.

routine to call the MMPT energy and force calculation routines when a energy calculation is requested in the CHARMM input script.

The non-bonded energy terms were more laborious to implement, mainly because of the numerous available algorithms to describe the electrostatic and van-der-Waals interactions. We focused our implementation efforts therefore on the recommended default options specified in the parameter file for proteins. These are the defaults that should be used in connection with the MMPT module to correctly calculate the electrostatic and van-der-Waals contributions of the hydrogen bonded atoms:

```
NONB NBXM 3 ELEC VDW ATOM CDIE SHIF VATOM VSWI BYGR NOEX NOEW
```

The options allow the calculation of the pair-wise electrostatic and van-der-Waals interactions between atoms, using a constant dielectric and shifting of the potential for long ranges. Please refer to the documentation for a detailed discussion of all the options given above. Care must be taken if other than these recommended options are used and it is recommended to verify the results with the provided test cases.

The flowchart illustrates the interaction of the MMPT routine with the main MD program.

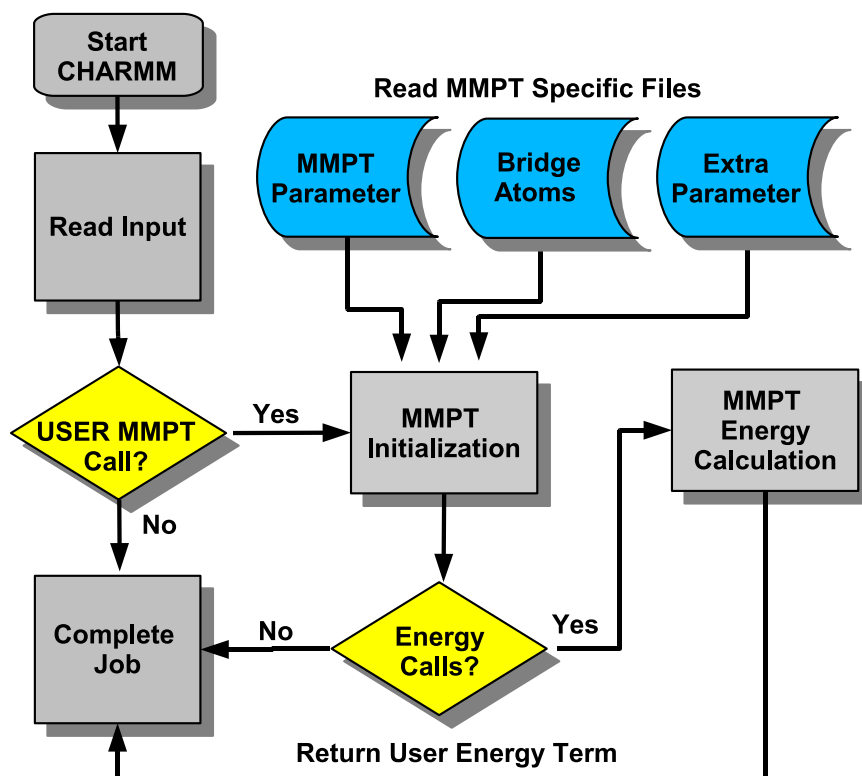


Figure A.1: Flowchart of the MMPT algorithm showing how its routines interact with the main CHARMM MD program.

## B. Fitting and Morphing of PES

### B.1. Fitting with I-NoLLS

The problem we face is to fit a set of PES data to a theoretical model, our analytical energy function. Estimation of the model is generally performed by a least-square fit. We use primarily the I-NoLLS program (107) for an interactive least-squares fitting. The program expects an initial trial parameter set, the target PES data and an energy function written in FORTRAN as input data to calculate the new fitted parameter. A first trial parameter set is easiest created by fitting the analytical functions with an additional graphical plotting program that has some fitting capabilities, e.g. xmgrace, and allows the user to examine the quality of the fit graphically and the suitability of the chosen fit functions. This initial parameter set is then already a good starting point for the fit using I-NoLLS and one gained already some insight about the different contributions of different parameter and the sensitivity of the algorithm. The initial least square fits were reduced on a set of points with energies lower than 20 kcal/mol. It is a strong feature of the program to interactively choose physical regions and tailor the selection of parameters accordingly. Once a reasonably good fit has been achieved on a subset of data points and parameter we can proceed the fit by increasing the data and parameter space step by step.

### B.2. Morphing of PES

The three model proton bound dimer show that the same functional form allows a successful fitting procedure to reproduce symmetric and nearly symmetric potential energy surfaces, as well as asymmetric PES. Although it is in principle possible to repeat the fitting process for any desired proton bound molecular system, it is beneficial to recognize the similarities of the proton transfer PES and that they can be put to use to circumvent the computational cost of new PES scans and reduce the laborious task of fitting entirely new parameter sets. By introducing constant scaling factors we are

able to change properties of the original PES, like barrier heights or minimum energy geometries. This transformation can be written mathematically as

$$V_{morph}(R, \rho, \theta) = \lambda(R, \rho, \theta) V_{orig}(R, \rho, \theta), \quad (\text{B.1})$$

where the definition of  $\lambda$  can be a plain constant as in the case of protonated diglyme or 2PY2HP or a complex function of one or more of the coordinates as it was necessary for the case of Ferredoxin I. A natural choice to control the barrier height would then be to introduce a potential scaling, whereas to affect the minimum energy geometries could be achieved by scaling the coordinates  $R, \rho, \theta$ .

In this paper we applied two transformations to demonstrate the principle idea, the effects on the PES and ultimately on the dynamics of the molecular systems. We introduce a constant potential scaling  $\lambda_V$  to influence the barrier heights. Scaling the potential is straightforward and it is directly implemented in the user-defined routine and the user can control the barrier height in the CHARMM input scripts through keywords. The coordinate scaling is applied to the data sets and refitted to derive new parameter sets which reflect the desired scaling. The coordinate scaling has not been implemented directly because of the various possible scaling transformations. Each possible choice needs a specific transformation and the resulting force derivatives need to be implemented specifically in the energy and force routines of the MMPT module for each choice. The coordinate scaling in  $R$  is demonstrated in Figs B.1–B.3 as a series of increasing scaling factors,  $\lambda = [1.01, 1.03, 1.06, 1.1]$ . The development of the parameter  $p_i$  of the functions  $D_{eq}(R)$ ,  $\beta(R)$  and  $R_{eq}(R)$  themselves are shown at the right column in the small diagrams. The larger diagrams on the left hand side depict the effects of the scaling on the shape and curvature of the functions that describe the proton transfer PES. The morphing transformation itself is done using several Python scripts that applies the desired transformation to the original PES scan results of the prototype dimers and outputs a morphed data set in format directly readable by the I-NoLLS program, where the new parameters of the morphed PES are then determined.

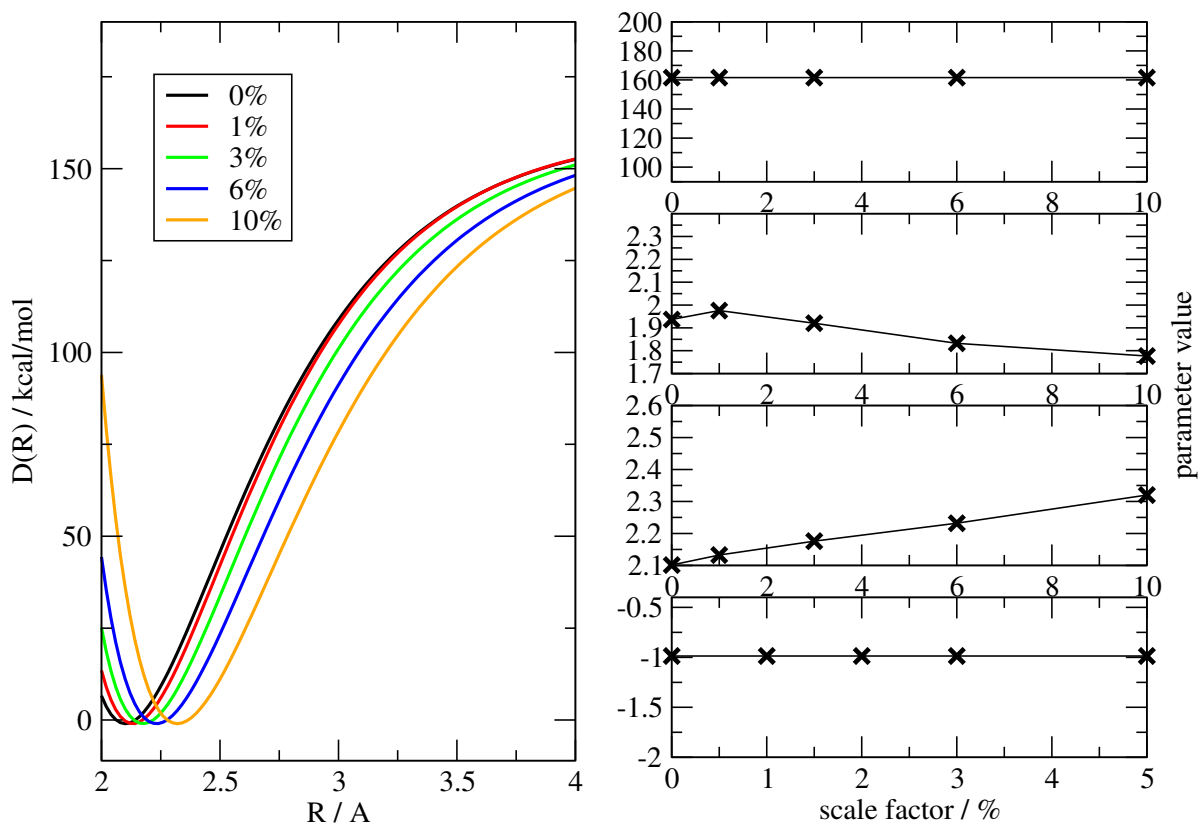


Figure B.1:

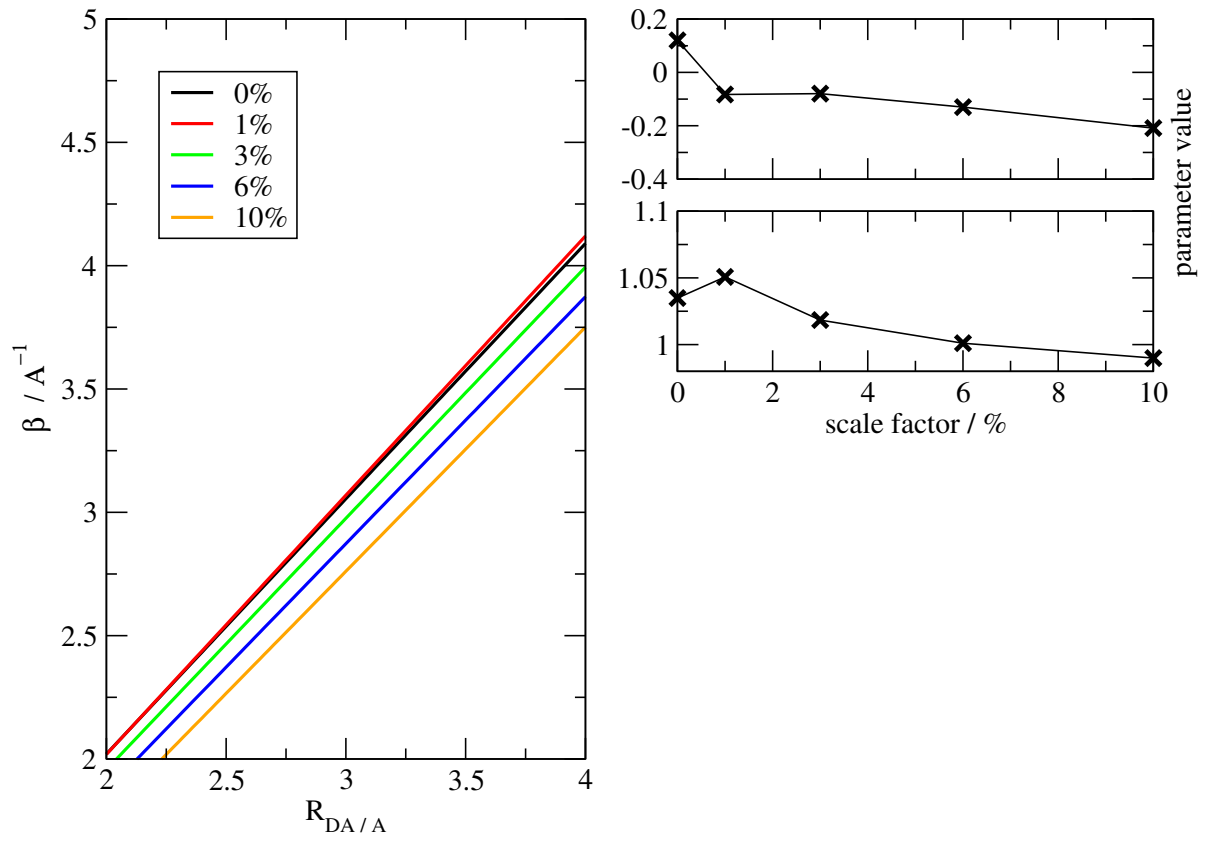


Figure B.2:

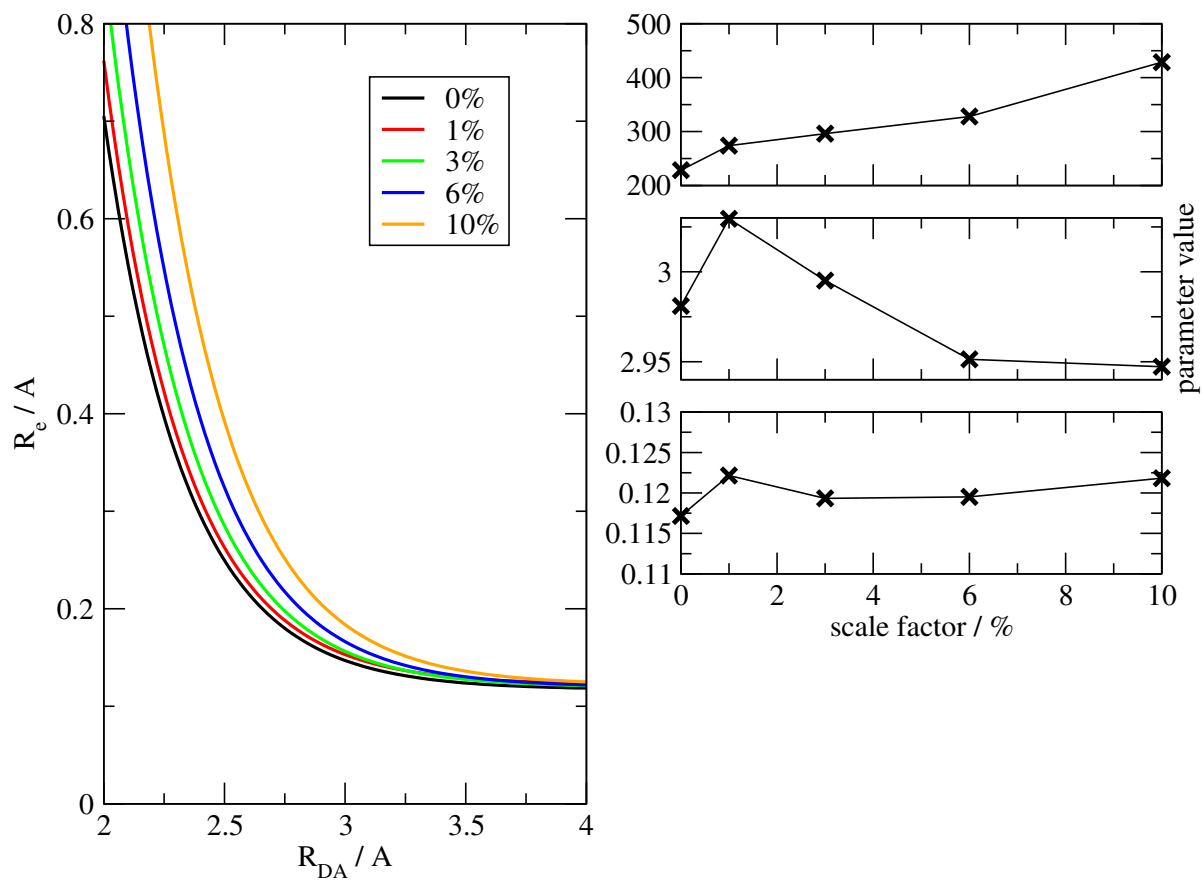


Figure B.3:





## C. Parameter Tables

$\lambda$		0.95	0.97	0.99	1.01	1.03	1.05	1.06	1.10	1.15	
$D_e(R)$	$p_1$	161.593	161.593	161.593	161.593	161.593	161.593	161.593	161.593	161.593	kcal/mol
	$p_2$	2.160	2.002	1.994	1.975	1.920	1.925	1.832	1.913	1.910	$\text{\AA}^{-1}$
	$p_3$	2.017	2.040	2.089	2.132	2.175	2.144	2.231	2.192	2.241	
	$p_4$	-0.987	-0.986	-0.986	-0.986	-0.986	-0.986	-0.986	-0.986	-0.986	-0.986
$\beta(R)$	$p_5$	0.534	0.511	0.092	-0.082	-0.079	-0.101	-0.130	-0.101	-0.101	$\text{\AA}^{-1}$
	$p_6$	0.889	0.857	0.991	1.050	1.018	1.038	1.001	1.017	1.001	$\text{\AA}^{-2}$
$R_{eq}(R)$	$p_7$	229.064	228.861	228.861	273.851	296.143	197.404	327.954	198.052	198.052	$\text{\AA}$
	$p_8$	3.095	3.022	2.994	3.029	2.995	2.877	2.951	2.808	2.751	$\text{\AA}^{-1}$
	$p_9$	0.113	0.107	0.112	0.122	0.119	0.117	0.119	0.114	0.112	$\text{\AA}$
$k$	$p_{10}$	0.010	0.010	0.010	0.010	0.010	0.010	0.010	0.010	0.010	kcal/mol
$c$	$p_{11}$	23.510	23.367	27.446	27.446	27.446	27.482	24.445	27.482	27.482	kcal/mol

Table C.1: The morphing parameter sets after several scaling factors  $\lambda$  were applied to the original double minimum  $\text{N}_2\text{H}_7^+$  potential energy surface. Combination of these sets were used to model the double proton transfer reaction in 2PY2HP.

$D_1(R)$		$\beta_1(R)$		$\rho_1(R)$					
$p_1$	16.079 kcal/mol	$p_5$	4.094 Å <sup>-1</sup>	$p_8$	-0.098 Å				
$p_2$	1.815 Å <sup>-1</sup>	$p_6$	2.323 Å <sup>-1</sup>	$p_9$	1.671 Å <sup>-1</sup>				
$p_3$	3.101	$p_7$	2.605 Å <sup>-1</sup>	$p_{10}$	2.533 Å				
$p_4$	121.346 kcal/mol			$p_{11}$	0.183 Å				
$D_2(R)$		$\beta_2(R)$		$\rho_2(R)$		$c$		$k$	
$p_{12}$	38.614 kcal/mol	$p_{16}$	5.500 Å <sup>-1</sup>	$p_{19}$	0.080 Å	$p_{23}$	63.478 kcal/mol	$p_{27}$	0.012 kcal/mol/deg
$p_{13}$	1.355 Å <sup>-1</sup>	$p_{17}$	1.979 Å <sup>-1</sup>	$p_{20}$	1.709 Å <sup>-1</sup>	$p_{24}$	0.836 Å <sup>-1</sup>		
$p_{14}$	2.964	$p_{18}$	2.634 Å <sup>-1</sup>	$p_{21}$	2.650 Å	$p_{25}$	2.703 Å		
$p_{15}$	75.398 kcal/mol			$p_{22}$	0.8590 Å	$p_{26}$	60.257 kcal/mol		

Table C.2: The parameter set for the fit of of the proton transfer potentials in NH<sub>4</sub><sup>+</sup> ··· H<sub>2</sub>O.

$D_1(R)$		$\beta_1(R)$		$\rho_1(R)$					
$p_1$	13.148 kcal/mol	$p_5$	3.849 Å <sup>-1</sup>	$p_8$	-0.075 Å				
$p_2$	1.667 Å <sup>-1</sup>	$p_6$	2.149 Å <sup>-1</sup>	$p_9$	1.893 Å <sup>-1</sup>				
$p_3$	3.030	$p_7$	2.594 Å <sup>-1</sup>	$p_{10}$	2.457 Å				
$p_4$	143.155 kcal/mol			$p_{11}$	0.154 Å				
$D_2(R)$		$\beta_2(R)$		$\rho_2(R)$		$c$		$k$	
$p_{12}$	15.959 kcal/mol	$p_{16}$	4.988 Å <sup>-1</sup>	$p_{19}$	0.063 Å	$p_{23}$	12.653 kcal/mol	$p_{27}$	0.011 kcal/mol/deg
$p_{13}$	1.342 Å <sup>-1</sup>	$p_{17}$	2.251 Å <sup>-1</sup>	$p_{20}$	1.769 Å <sup>-1</sup>	$p_{24}$	0.794 Å <sup>-1</sup>		
$p_{14}$	3.031	$p_{18}$	2.521 Å <sup>-1</sup>	$p_{21}$	2.650 Å	$p_{25}$	2.669 Å		
$p_{15}$	38.244 kcal/mol			$p_{22}$	0.848 Å	$p_{26}$	32.4355 kcal/mol		

Table C.3: The morphed parameter set used in the Ferredoxin I studies. Derived by morphing the original asymmetric PES of NH<sub>4</sub><sup>+</sup> ··· H<sub>2</sub>O to protonated aspartic acid and water, a model system of the active site.

## Curriculum vitae

Dipl. Physiker Sven Lammers

\* 23. Februar 1974 in Husum, Deutschland

Lothringerstrasse 113

4056 Basel

Schweiz

- 7/1994 Abitur – Fachgymnasium (Wirtschaftlicher Zweig) der Beruflichen Schule des Kreises Nordfriesland
- 8/1994 – 9/1995 Zivildienst
- 10/1995 – 2/1999 Studium der Physik an der Universität Heidelberg, Deutschland
- 2/1999 – 12/1999 Studium der Physik an der Universität Kapstadt, Südafrika
- 12/1999 B. Sc. (Honours) in Physik
- 1/2000 – 6/2002 Studium der Physik an der Universität Heidelberg, Deutschland
- 6/2002 Diplom in Physik
- 10/2002 – 12/2006 Dissertation am Departement Chemie der Universität Basel, Schweiz

### Publikationen

- Investigating the Relationship between Infrared Spectra of Shared Protons in Different Chemical Environments: A Comparison of protonated diglyme and protonated water dimer, S Lammers and M Meuwly, Journal of Physical Chemistry, *in revision*
- Double Proton Transfer using Dissociable Force Fields, S Lammers and M Meuwly, Australian Journal of Chemistry, 2004
- Convergence properties of X-ray scattering calculated from protein crystal molecular dynamics simulations, L Meinhold, S Lammers, T Becker, and JC Smith, Physica B: Physics of Condensed Matter, 2004
- Io as a source of the Jovian dust streams, AL Graps, E Grün, H Svedhem, H Krüger, M Horányi, A Heck and S Lammers, Nature, 2000
- Observations of electromagnetically coupled dust in the Jovian magnetosphere, H Krüger, E Grün, AL Graps, S Lammers, Astrophysics and Space Science, 1999
- Analysis of the sensor characteristics of the Galileo dust detector with collimated Jovian dust stream particles, H Krüger, E Grün, A Heck, S Lammers, Planetary & Space Science, 1999

Während meiner Studienzeit an der Universität Basel besuchte ich Vorlesungen, Seminare und Praktika der folgenden Dozenten:

Prof. Dr. Stefan Goedecker, Prof Dr. Hanspeter Huber, Prof. Dr. Markus Meuwly,  
Prof. Erik van Nimwegen, Prof. Dr. Torsten Schwede, Prof. Dr. Angelo Vedani